2014

CAPILLARITY AND TWO-PHASE FLUID TRANSPORT IN MEDIA WITH FIBERS OF DISSIMILAR PROPERTIES

Thomas M. Bucher Jr.
Virginia Commonwealth University, buchertm@mymail.vcu.edu

CAPILLARITY AND TWO-PHASE FLUID TRANSPORT IN MEDIA WITH FIBERS OF DISSIMILAR PROPERTIES

A dissertation submitted in partial fulfillment of the requirements for the degree of Doctor of Philosophy at Virginia Commonwealth University.

by

THOMAS MICHAEL BUCHER JR.

MS, Mechanical and Nuclear Engineering, Virginia Commonwealth University, 2012
BS, Mechanical Engineering, Virginia Commonwealth University, 2010

Director: DR. HOOMAN VAHEDI TAFRESHI
ASSOCIATE PROFESSOR, MECHANICAL AND NUCLEAR ENGINEERING

Virginia Commonwealth University
Richmond, Virginia
August 2012

Acknowledgements

I would of course like to thank my advisor, Dr. Hooman Vahedi Tafreshi for all the years of collaboration that would seem to have accumulated over the course of my work. It has been an experience that will soon be forgotten or repeated, and his guidance has helped make this dissertation what it is.

I would also like to thank the other members of my Ph.D. committee, Dr. Daren Chen, Dr. Worth Longest, Dr. Rebecca Segal, and Dr. Alenka Luzar for their service and for their insightful questions and comments which have helped strengthen my work. I would also like to thank Dr. Mohamed Gad-el-Hak and Dr. James McLeskey for their wisdom and counsel over the years

Regarding friends and family, if I said all there was to say, this section would be as long as the thesis. For their love, patience, guidance, and inspiration, I will always be grateful to Anna and Bud, Mrs. Ward, Gram and Gramp, Laura, Rob, Beth, Mom, various Buchers, Curleys, Junods, and other far-flung relatives whose names elude me right just now, Satan (not that one, a different one), Helen Richard Dyer (my best friend I don't hang out with ever), my labmates past and present, and maybe Raghu Arambakam.

For Bob and Stelle Junod.

Honestly, who else???

Table of Contents

Abstract

CAPILLARITY AND TWO-PHASE FLUID TRANSPORT IN MEDIA WITH FIBERS OF DISSIMILAR PROPERTIES

By Thomas Michael Bucher Jr., M.S.

A dissertation submitted in partial fulfillment of the requirements for the degree of Doctor of Philosophy at Virginia Commonwealth University.

Virginia Commonwealth University, 2014

Director: Dr. Hooman Vahedi Tafreshi
Associate Professor, Mechanical and Nuclear Engineering

Capillarity is a physical phenomenon that acts as a driving force in the displacement of one fluid by another within a porous medium. This mechanism operates on the micro and nanoscale, and is responsible for countless observable events. This can include applications such as absorption in various hygiene products, self-cleaning surfaces such as water beading up and rolling off a specially-coated windshield, anti-icing, and water management in fuel cells, among many others.

The most significant research into capillarity has occurred within the last century or so. Traditional formulations for fluid absorption include the Lucas–Washburn model for porous media, which is a 1-D model that reduces a porous medium to a series of capillary tubes of some educated equivalent radius. The Richards equation allows for modeling fluid saturation as a function of time and space, but requires additional information on capillary pressure as a

function of saturation ($p_c(S)$) in order to solve for absorption. In both approaches, the surface can only possess one fluid affinity. This thesis focuses on developing capillary models necessary for predicting fluid absorption and repulsion in fibrous media. Some of the work entails utilizing approximations based on pore space available to the fluid, which allows for capillary pressure simulation in media with arbitrary fiber orientation. This thesis also presents models for tracking the fluid interface in fibrous media and coatings with simpler geometries such as horizontally and vertically aligned fibers and orthogonal fiber layers. This method hinges on solving for the true fluid interface shape between the fibers based on the balance of forces across it, ensuring the accurate location and total content of fluid in the medium, and therefore accurate $p_c(S)$. Using this approach also allows, for the first time, fibers of different fluid affinities to exist in the same structure, to examine their combined influence on fluid behavior. The models in this thesis focus mainly on absorbent fabrics and superhydrophobic coatings, but can be easily expanded for use in other applications such as water filtration from fuel, fluid transport and storage in microchannels, polymer impregnation in fiber-reinforced composite materials, among countless others.

Chapter 1: Overall Objectives of This Thesis

This thesis primarily focuses on the phenomenon of capillarity and capillary pressure, and always as it pertains to various fibrous configurations. The earliest capillary models chronologically involve the Full Morphology method, which focuses on relations between capillary pressure and fluid content in a given structure, but do so using a mathematical approximation that negates calculating meniscus shape or allowing multiple wettabilities in a single structure. Simulations performed using this method, however, provide a benchmark, a context in which subsequent models and derivation can be considered and compared. The true novelty of the work is in the development of models that produce the true shape of the water–air interface within a fibrous structure, and facilitate characterizing additional information about the system.

Chapter 2 will provide a background for capillarity as a phenomenon, and give an overview of the two primary approaches for modeling absorption in fibrous media. We will also examine applications in which capillarity resulting in the repelling of fluids is beneficial, with particular emphasis on fibrous superhydrophobic coatings. Other applications for repulsion will also be discussed, such as oil–water filtration coatings, gas diffusion layers in fuel cells, and Laplace barriers in microchannels.

Chapter 3 will focus on capillarity models developed for absorption. We will begin with models for capillary height rise in a tube, which will establish some initial information for analytical force balance expressions that will apply to more complicated models. We will then benchmark several numerical approaches for determining interface curvature with our analytical expressions. From there, we will consider height rise in vertically arranged fiber bundles, introducing an analytical expression for overall height rise, as well as a numerical model for determining meniscus shape for randomly placed vertical fiber bundles containing multiple wettabilities (i.e., contact angles). We will then review our strategies for capillary flows perpendicular to fibers in a medium, first discussing the Full Morphology (FM) method, and then moving on to an approach based on the balance of forces of a fluid interface working its way through horizontal parallel fibers. Like the vertical fibers, this model yields the true interface shape, and can accommodate multiple contact angles in a single medium.

Chapter 4 will entail our application of one of our capillarity models to solve the Richards Equation on the macroscale for thin fibrous wipes. We will explain modeling permeability (another contributor to the nonlinearity of the Richards equation), then show a series of models for absorption and drainage, emphasizing effects of fiber orientation and the hydrophilicity of the dry surface.

Chapter 5 will examine our models for characterizing fibrous superhydrophobic coatings. We will begin by summarizing several force balance equations for the simple case of parallel fibers. We will then examine the disparity between force balance and FM results for this simple case for varying fiber spacings and contact angles. From there, we will present the results of a

series of FM simulations to establish critical pressure as it relates to microstructure properties. We will do this for randomly layered coatings and orthogonally layered coatings. From there, we will examine a model that determines critical pressure by calculating the minimum-energy shape of the fluid interface in an orthogonally layered coating, as well as establishing wetted area (which contributes to effectiveness of drag force reduction). As with the meniscus shape-based absorption models, this approach can also facilitate multiple contact angles in a single structure, so this effect will be examined as well. We will take a brief look at the extension of our orthogonal coating structures to the context of aerosol filtration, establishing observed properties unique to coatings of this design. These properties make such a nanofibrous structure useful as an additional filter coating applied downstream of a filter medium with larger fibers.

Finally, we will close with our overall conclusions in Chapter 6, as well as with recommendations for future extensions of this work.

Chapter 2

Capillarity in Fibrous Media: Background Information

Capillarity is the physical mechanism by which two immiscible fluids establish conditions (i.e., shape and position of the deformable interface between them) that minimize surface energy (de Gennes *et al*., 2004). The surface tension over the interface in, for example, a droplet in midair causes the droplet to conform to a spherical shape within the constraints of forces such as air resistance and gravity. In the application of porous media, this mechanism always involves a solid surface. The chemistry of the surface is typically such that it has an affinity for one of the two fluids over the other. Sticking for now with the example of the two fluids being water and air, the difference in the solid–fluid surface tension when the fluid is air versus when it is water causes a droplet on a flat surface to conform to a contact angle θ with the surface, as is shown in Figure 2.1 (Dullien, 1992). Figure 2.1a illustrates the balance of surface tension forces on the contact line where the three phases meet (point A in the two-dimensional figure). The balance of the three forces yields the contact angle θ the droplet makes with the surface, given by the Young equation (Dullien, 1992):

$$\sigma_{lg}\cos\theta = \sigma_{sg} - \sigma_{sl} \tag{2.1}$$

where the subscripts *s*, *l*, and *g* stand for solid, liquid, and gas, respectively. This contact angle property is exploited through various mechanisms which will be discussed in this introduction. As can be seen in Figures 2.1b and 2.1c, the overall characteristic of whether a surface can be

regarded as hydrophilic (prefers and retains water) or hydrophobic (repels water) simply comes down to whether θ is greater than or less than 90°.

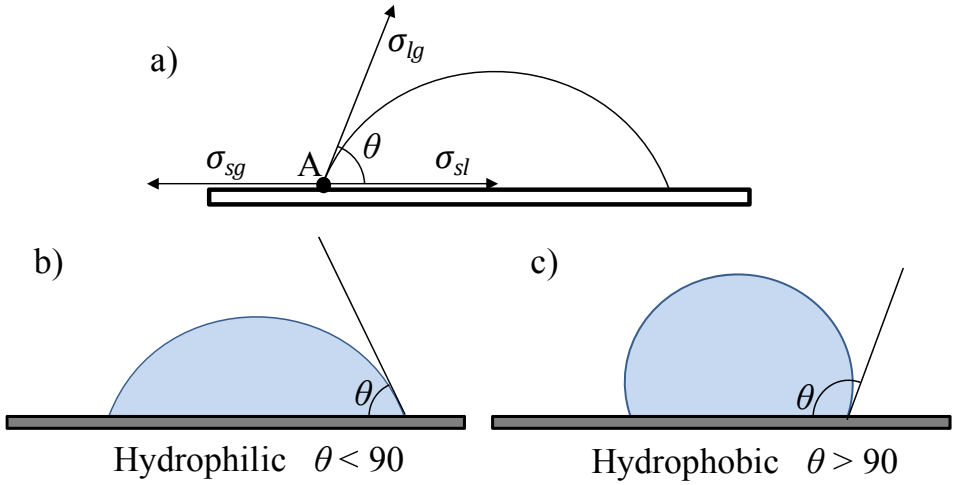

Figure 2.1: (a) Illustration of the balance of forces between the three surface tension forces along the ring where three phases meet (shown as point A in two dimensions) for a droplet on a flat surface. (b) Droplet on a hydrophilic surface ($\theta < 90°$) . (c) Droplet on a hydrophobic surface ($\theta > 90°$).

Depending on the hydrophilicity or hydrophobicity, porous media and coatings comprised of a given material can be used in a number of applications, so long as the size scale of the working components of the medium (e.g., wicks, posts, grooves, fibers, etc.) is on an order of magnitude sufficient for surface tension forces to be a relevant factor. In the event that a dry hydrophilic material comes into contact with a reservoir of water, it will spontaneously absorb the water via capillary forces, displacing the non-wetting air. In a capillary tube, such as those shown in Figure 2.2, the capillary forces acting around the interior ring of the tube draw a partial vacuum in the liquid at the top of the front (Masoodi and Pillai, 2013), drawing the liquid into the tube until the weight of the liquid in the column matches the drawing force of the tube. The pressure difference across the spherical meniscus inside the tube (capillary pressure p_c) is given by the well-known Young–Laplace equation:

$$p_c = \frac{2\sigma \cos\theta}{r_{cap}} \tag{2.2}$$

where r_{cap} is equal to the radius of the tube.

Figure 2.2: Absorption of liquid into a series of tubes via capillary forces.[1]

This fundamental mechanism is the driving force behind much of the material covered in this thesis, and a number of predictive models for understanding the role of capillarity different applications will be explored.

2.1 Applications and Models: Absorption

Lucas–Washburn Models

The oldest models were applied to absorption into porous media. It is the most broadly applicable use for the understanding of capillarity, applying heavily in soil science and petroleum engineering, and in fibrous media extending to wipes, diapers, sanitary patches, among many

[1] Image from http://fphoto.photoshelter.com/image/I000096KKIQwJAGc

other things. Vertical fluid rise z in a capillary tube of fixed diameter d_{cap} was the first quantifiable experiment involving capillarity, resulting in what later became known as Jurin's law (Jurin, 1719):

$$z = \frac{4a^2 \cos\theta}{d_{cap}} \tag{2.3}$$

where $a = \sqrt{\sigma / \rho g}$ is equal to capillary length scale. ρ and g represent surface tension, density, and gravitational acceleration, respectively. The effect of capillarity is significant when d_{cap} is less than capillary length a (Ponomarenko *et al*., 2011). It is easily seen that this equation is simply Equation 2.2 with hydrostatic pressure equal to capillary pressure. The oldest dynamic formula using capillarity that is still used today is the Lucas–Washburn model for absorption, derived from 1-D Poiseuille flow in a vertical capillary tube (Lucas, 1920; Washburn, 1921; Hollies *et al.*, 1957; Miller and Jansen, 1982; Hodgson and Berg, 1987; Zhmud *et al.*, 2000; Mullins *et al*., 2007):

$$\frac{2\sigma \cos\theta}{r_{cap}} = \rho g z + \frac{8\mu z}{r_{cap}^2}\frac{dz}{dt} \tag{2.4}$$

Some researchers have in recent years also taken inertia into consideration for a dynamic model, in which case Equation (2.4) instead becomes (Fries and Dreyer, 2008a and b; Ben Amara and Ben Nasrallah, 2011; Masoodi *et al*., 2013):

$$\frac{2\sigma \cos\theta}{r_{cap}} = \rho g z + \frac{8\mu}{r_{cap}^2} z\dot{z} + \rho \frac{d(z\dot{z})}{dt} \tag{2.5}$$

In either case, Equations (2.4) and (2.5) simplify to Equation (2.3) when a steady-state condition is reached. The simple geometry of the vertical capillarity has formed the basis of many empirical and theoretical representations of capillarity. Many researchers have taken to

simplifying the complex internals of a porous medium by representing them as bundles of parallel capillary tubes with some effective radius determined empirically (Dullien, 1992). The same basis for derivation was later revisited by Marmur (1988), in which a model for predicting the radial horizontal spread of a fluid from an infinite reservoir of radius r_0 was developed, and later validated for spread in sheet papers (Danino and Marmur, 1994). A modified form of Marmur's equation was then presented in Hyvaluoma *et al*. (2006) as

$$\left(\frac{r}{r_0}\right)^2\left(\ln\frac{r}{r_0}-\frac{1}{2}\right)+\frac{1}{2}=\frac{\sigma d_{cap}\cos\theta_{cap}}{12\mu r_0^2}t \tag{2.5}$$

Additional similar relations for radial spread have also been developed and validated on similar bases (Danino and Marmur, 1994; Conrath *et al*., 2010). Equation 2.5, or any such equation derived based on a capillary-tube representation of a multi-component fibrous medium (medium having more than one fiber diameter and/or wall-contact angle), requires single numeric values for the diameter d_{cap} and contact angle θ_{cap} of the representative capillary tube.

These models, collectively referred to in this work as Lucas–Washburn (LW) approaches, all hinge upon the simplifying act of reducing the porous medium under consideration to one or more capillary tubes, dismissing the actual morphology of the medium and the fluid's actual behavior in such a medium. Moreover, the focus of these approaches on the location of a distinct liquid front prevents one from considering partially-saturated regions in a medium, and its derivation limits it to applicability in one dimension only. Nonetheless, the model has had utility in quantifying a problem as complicated as porous geometries, as demonstrated in the above works, among many others. One of the first models discussed in the next chapter will be a vertical height rise model in the same vein as the LW models, but will leave the geometry of the

fibers intact, modeling capillarity in aligned fiber tows. The results of this approach can then be tailored to the models discussed above, such as establishing d_{cap} and θ_{cap} in Equation 2.5.

The Richards Equation

An alternative approach to LW models is the Richards equation (Richards, 1931). Rather than fixating on a location of a single liquid front, the Richards equation expresses saturation S (i.e., the ratio of absorbed fluid volume to total pore volume) as a function of time and space, modeling the domain on the macroscale as a homogeneous zone with uniform properties—properties arrived upon through the use of additional microscale correlations. Deriving the Richards equation begins with the 3-D unsteady continuity equation:

$$\Phi \frac{\partial S}{\partial t} + \frac{\partial u}{\partial x} + \frac{\partial v}{\partial y} + \frac{\partial w}{\partial z} = 0 \tag{2.7}$$

where ε is equal to the solid volume fraction (SVF) of the medium. The velocity terms can be substituted using Darcy's Law (Jaganathan *et al*., 2009):

$$u_i = -\frac{k_{ij}(S)}{\mu} \frac{\partial p_c(S)}{\partial x_j} \tag{2.8}$$

where $k_{ij}(S)$ is equal to permeability of the medium (described in greater detail later in this thesis), a second-order tensor whose off-diagonal terms have been found to be negligible (Ashari and Tafreshi, 2009), and μ is equal to viscosity. Substituting into Equation 2.7 and applying the chain rule to $p_c(S)$, the Richards equation is thus given as

$$\begin{aligned} &\Phi \frac{\partial S}{\partial t} - \frac{1}{\mu}\left(\frac{\partial}{\partial x}\left(k_{xx}(S) \frac{\partial p_c}{\partial S} \frac{\partial S}{\partial x} \right) + \frac{\partial}{\partial y}\left(k_{yy}(S) \frac{\partial p_c}{\partial S} \frac{\partial S}{\partial y} \right) \right. \\ &\left. + \frac{\partial}{\partial z}\left(k_{zz}(S) \frac{\partial p_c}{\partial S} \frac{\partial S}{\partial z} \right) \right) = 0 \end{aligned} \tag{2.9}$$

The full equation is highly nonlinear, with capillary pressure and permeability both being functions of S themselves. The result is a solution that allows for partially saturated regions to exist inside the domain, and can facilitate spread and transport in multiple dimensions, as will be shown later. Figure 2.3a shows a contour plot for the final solution for height rise in a vertically hung strip of fabric (from Jaganathan *et al*., 2009). Figure 2.3a shows an example using the Richards equation to solve for vertical height rise of mineral oil in fabric sheets over time. The solution is plotted along with the results of three experiments performed in conjunction with it. Accounting for gravity and simplifying to absorption in one dimension, Equation 2.9 becomes

$$\Phi \frac{\partial S}{\partial t} - \frac{1}{\mu}\left(\frac{\partial}{\partial z}\left(k_{zz}(S) \frac{\partial p_c}{\partial S} \frac{\partial S}{\partial z} + \rho g k_{zz}(S) \sin\beta \right) \right) = 0 \qquad (2.10)$$

where β is equal to the inclination angle of the fabric (90° being vertical). Figure 2.3b shows how the distribution of the partially saturated region in a sample at equilibrium changes with inclination angle β, indicating the decrease in overall wetted length and in the size of the partially saturated region.

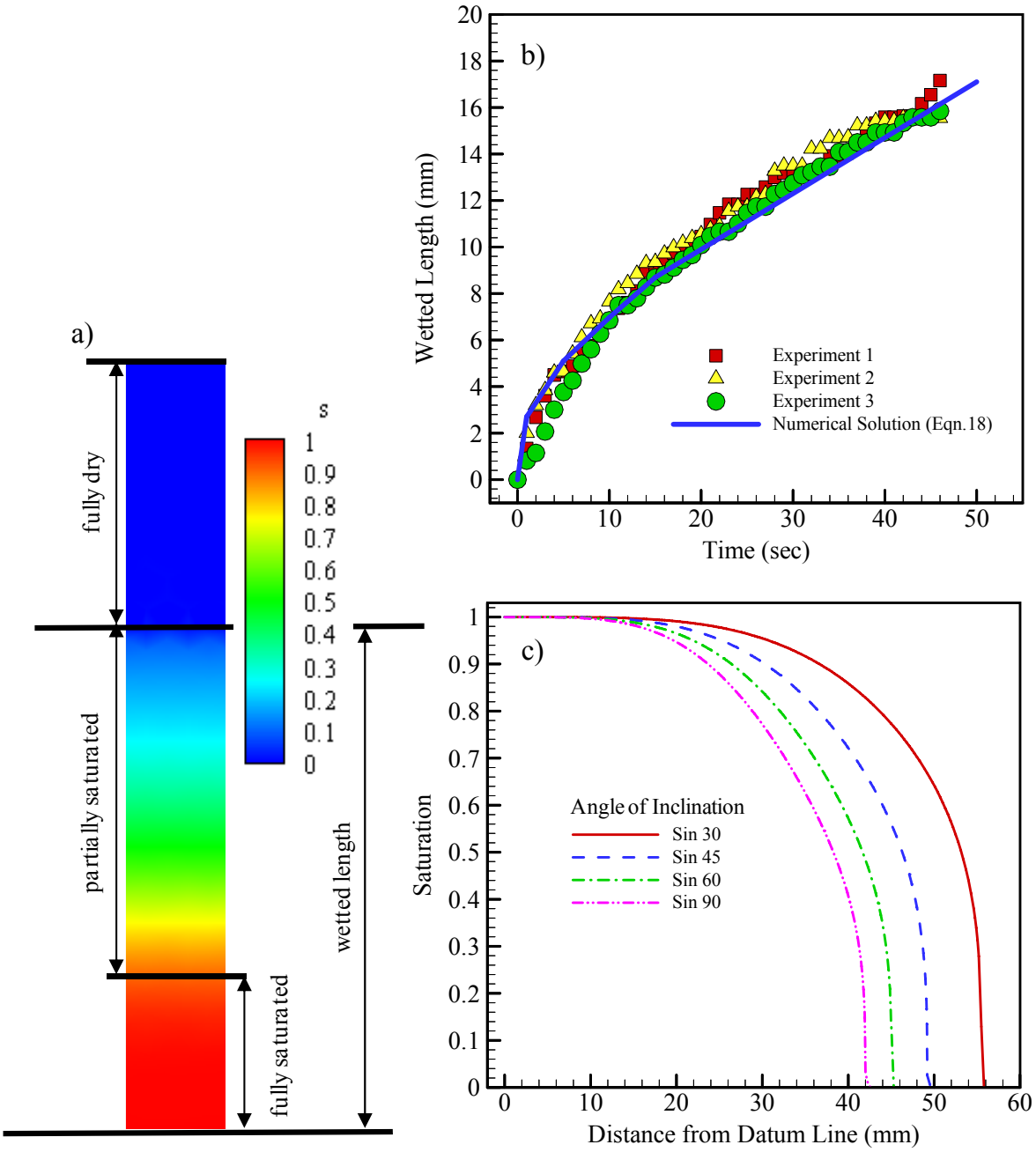

Figure 2.3: (a) Contour plot showing the solution of the one-dimensional Richards equation with gravity (2.10) for vertical height rise in fabric samples from the work of Jaganathan *et al*. (2009). (b) Height rise with respect to time for three experiments (symbols) and the numerical solution of Equation 2.9 (solid line), $\beta = 90°$. (c) Effect of angle β on overall height rise and size of partially saturated region.

2.2 Applications and Models: Repulsion

Superhydrophobic Coatings and Surfaces

The models introduced thus far have focused on absorption. A surface that possesses a contact angle greater than 90° (hydrophobic) results in behaviors that lend themselves to other intriguing applications. An area of particular interest this thesis will focus on is superhydrophobic surfaces. Superhydrophobicity is typically the combination of two effects: an inherent hydrophobicity of the surface as described above, and an additional surface roughness on the micro or nanoscale which facilitates the trapping of air beneath a drop of water in the spaces between microridges. These effects combine to endow an apparent contact angle (i.e., an observed contact angle regardless of surface topography) greater than 150°.

This phenomenon was first observed in nature (like so many phenomena that find their way into engineering application), utilized by a number of plants and animals for various purposes. The most famous example is that of the lotus leaf, whose leaves possess a characteristic superhydrophobicity owed to a combination of epidermal roughness and an epicuticular wax coating (Samaha *et al.*, 2012; Koch *et al.*, 2009; Barthlott and Neinhuis, 1997). The lotus uses superhydrophobicity for self-cleaning, as an incoming drop will easily roll off the leaf, taking with it any particulate debris in its path. This maximizes the available surface area on the leaf for photosynthesis. Other examples include the water strider using superhydrophobicity to walk on water, and the diving bell spider using the phenomenon to live its entire life underwater (Seymour and Hetz, 2011).

Among the first uses considered for superhydrophobic surfaces and coatings were self-cleaning for such applications as clothing and car windshields, using the same principles as the lotus. Another interesting application is anti-icing for aircraft. Ice cannot accumulate on the exterior of an airplane if water cannot adhere to the surface to begin with. This application has also been extended to wind turbines, as the accumulation of ice on the blades causes a considerable reduction in their efficiency (Alizadeh, *et al.*, 2012). However, more recently, the use of superhydrophobic coatings for submersible applications has become a subject of considerable interest (Samaha *et al.*, 2012), and is the main application studied in this thesis. Patel *et al*. (2013) and Patel and Chase (2014) also investigated the applicability of superhydrophobic electrospun fibrous membranes for use in water droplet separation from diesel fuel flows, as opposed to simply producing slip flow along a channel wall. Water droplets in the fuel would be caught by the capillary properties of the fibers, removing them from the flow.

To achieve the necessary surface roughness synthetically, a number of techniques have been developed in the last decade or so. Most engineered superhydrophobic surfaces to date are comprised of micro-fabricated posts or grooves. Figure 2.4a shows a series of SEM images of surfaces comprised of ordered posts from the work of Lee *et al.* (2008). By varying post diameter while keeping pitch (center-to-center distance between posts) constant, the authors were able to determine the gas fraction for each substrate (shown in the corner of each image), and subsequently measure the slip effect for each case using a rheometer. Maynes *et al.* (2007) performed a similar study in which micro-channels were aligned parallel to a passing laminar flow (shown in Figure 2.4b). The ordered nature of these micro-engineered surfaces lends itself to the devising of analytical functions for meniscus stability based on the balance of forces

between the air–water interfaces between the microstructures. These expressions can then be used to compare against numerical and experimental data, as the authors of these works have done. A disadvantage to this manufacturing method is that producing such surfaces and coatings on a large scale is time-consuming, expensive, and impractical when considering the necessity of conforming the surfaces to arbitrary shapes.

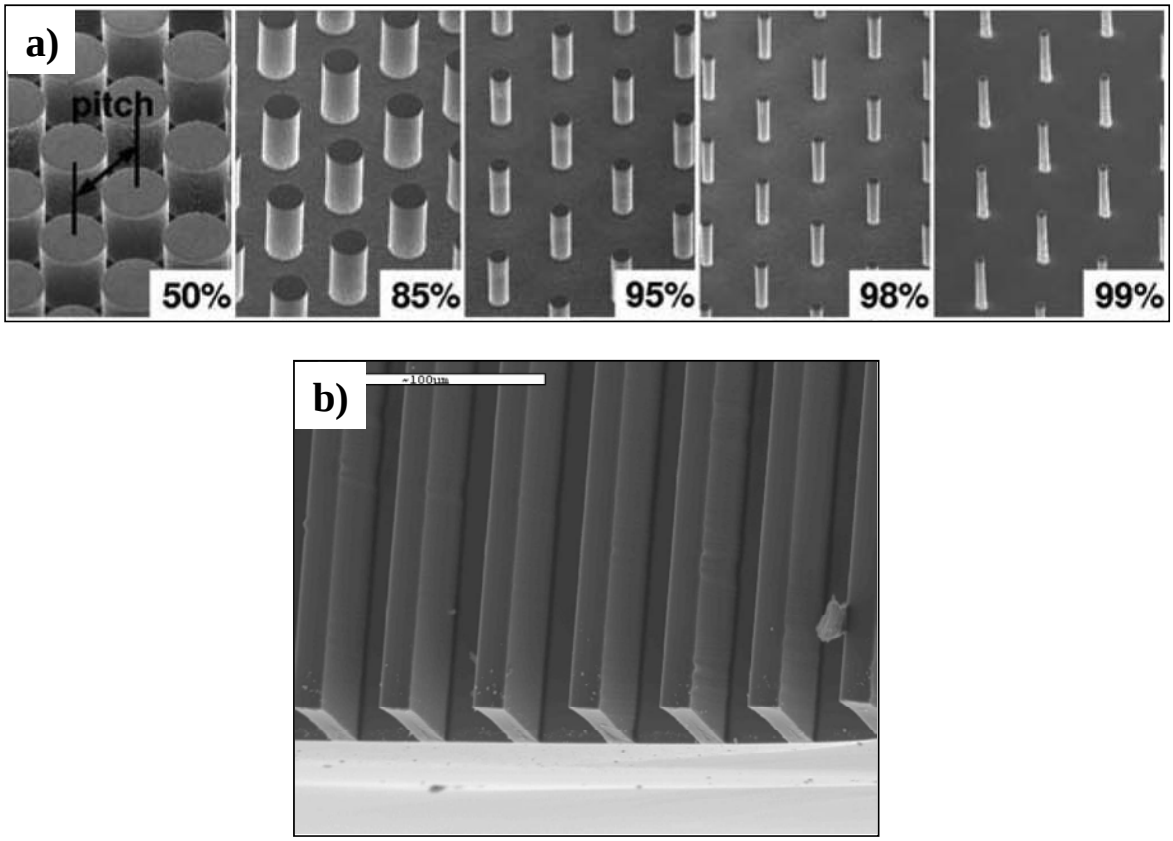

Figure 2.4: (a) Examples of superhydrophobic surfaces comprised of evenly distributed, microfabricated posts under an SEM from the work of Lee *et al.* (2008). The pitch for all surfaces shown is 50 μm. Percentages denote the gas fraction for each case. (b) SEM image of a surface comprised of microfabricated grooves from the work of Maynes *et al.*, (2007). The grooves are 15 μm deep and 30 μm wide, while the ridges have a width of 10 μm.

Recent studies have shown that superhydrophobic coatings can also be produced using polymeric nanofibers manufactured via electrospinning (Ma *et al*., 2005, 2008). Electrospinning is more cost effective than microfabrication, and can better conform to surfaces with arbitrary

shapes. With electrospinning, however, one has less control over the coating microstructure. Different methods of electrospinning can produce fibrous coatings with varying degrees of order and controllability in how fibers are laid down. Nanofibers produced via electrospinning often have random in-plane orientations, owing to the unstable whipping of the polymer filament as it is released from the Taylor cone (Yarin *et al*., 2001; Reneker and Yarin, 2008).

In a typical electrospinning process, a DC electric field is applied to a polymer solution contained within a capillary needle. Such a field exerts a force on the polymer solution, distorting the fluid surface at the tip of the injection needle into a characteristic Taylor cone, caused by the balance between surface tension and the applied electric force. When the electric force on the liquid exceeds a critical limit, a jet of charged liquid emerges from the tip of the Taylor cone, and if the solution contains a polymer solute, continuous polymer nanofibers can be produced with diameters well below 1 μm. However, in a electrospun fiber mat, the electrically charged fibrous output from the capillary needle swings and spirals wildly due to Coulombic self-repulsion, leading to loops in the deposited fiber diameters on the order of several millimeters. Figure 2.5a shows a typical electrospun nanofiber coating from the work of Uecker *et al*. (2010). Such a coating possess the roughness necessary on the nanoscale to facilitate superhydrophobicity on the substrate to which the coating is applied.

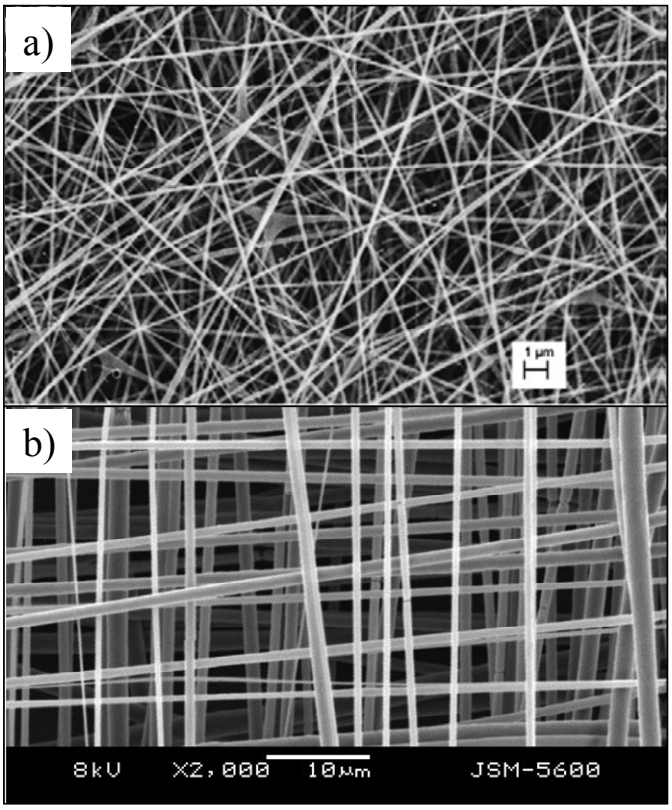

Figure 2.5: (a) SEM image of randomly laid nanofibrous coating fabricated using electrospinning (from the work of Uecker *et al*., 2010). (b) SEM image of orthogonally laid electrospun coating.[2]

Recent advances in the area of electrospinning have allowed for minimizing or counteracting the effect of Coulombic self-repulsion production of coatings with controlled spacing and orientation in its fibers, enough even to produce coatings with layers laid orthogonally to one another (Kessick and Tepper, 2003, 2004 and 2006; Levit and Tepper, 2004; Sarkar *et al*.,2007, among many others), as shown in Figure 2.5b. A superhydrophobic coating comprised of electrospun nanofibers can potentially generate drag-reduction and pressure-tolerance performance characteristics similar to those of microfabricated posts and ridges, but at a much lower cost. To encourage the desired inter-fiber voids within the medium, one can

[2] Image from http://www.nasa.gov/centers/langley/business/tg-img-fibermats.html.

produce coatings with bimodal fiber-diameter distributions if desired. Generally speaking, the coarse fibers in such coatings would help to provide the required porosity and thickness, whereas fine fibers would control the pore size.

A water–air system on a superhydrophobic surface is typically regarded as being in one of two states, illustrated in Figure 2.6. In the Cassie state, a volume air is trapped below the water droplet, which rests on the top of the coating (Cassie and Baxter, 1944). The reduced water–solid contact area results in the desired free-slip condition which would reduce skin-friction drag. The second state, the Wenzel state, is when the water has penetrated into the coating and displaced the trapped air (Wenzel, 1936). In this state, the free-slip condition has vanished, as the coating itself is now submerged in the flow. Coating failure is defined simply as the transition from the Cassie state to the Wenzel state. Models and experiments for superhydrophobic coatings are often concerned with two primary pieces of information (among some others): the critical pressure, the pressure beyond which a meniscus fails simply due to applied forces overcoming capillary forces; and longevity, the time required for trapped air to diffuse into the water and cause coating failure.

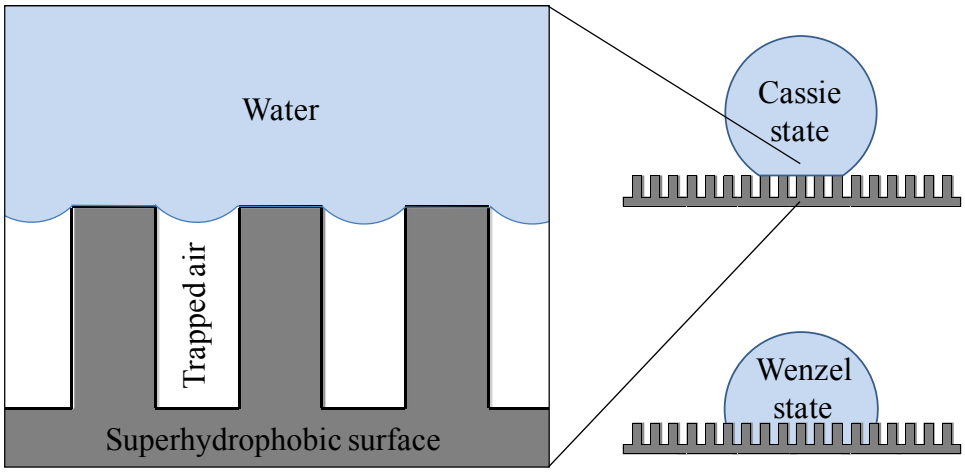

Figure 2.6: Side view illustrating the two primary quasi-static water–surface interface states on a superhydrophobic surface, in this case comprised of ordered, microfabricated posts.

The work presented in this thesis is focused on studying the effect of the microstructure on critical pressure, and therefore its resistance against hydrostatic pressures. We will first examine this using the Full Morphology approach—a method also applied to find $p_c(S)$ in our Richards equation model introduced earlier. This method, however, while useful for establishing relations for media with fibers of any arbitrary orientation, does so at the expense of a true shape for the air–water interface in our coatings. Were the true meniscus shape calculated, one could also calculate the exact solid area in contact with water (the area causing friction due to the no-slip boundary) and predict the drag reduction percentage brought about by the coating. Emami *et al*. (2011, 2012) developed several models capable of determining meniscus shape for surfaces comprised of posts and thin fibrous coatings (i.e., one or two layers thick). We therefore also present in this thesis an alternative method that can be applied to orthogonally oriented coatings, in which the true meniscus shape is calculated, thus providing both failure pressure and maximum water contact area. The model is based on solving for the interface shape that minimizes surface energy. Moreover, this model can be applied to coatings comprised of

multiple fiber types (i.e., contact angles). Both methods will be elaborated upon in subsequent chapters.

Additional Potential Applications

The work to follow in this thesis focuses particularly on fibrous media and coatings, but could easily be tailored to a number of other phenomena in which capillarity plays a central role. In microfluidics, microposts can be added to thin flat microchannels to induce and control fluid transport in microchannels (Saha *et al*., 2009). In the work of Kreit *et al*. (2010) and Schultz *et al*. (2014), the authors used arranged pillars in thin mircochannels to act as Laplace barriers in electrowetting. As is shown in Figure 2.7, a charge is applied to an electrode to provide the motive force to conform a fluid to some intended geometry within the channel, and then the hydrophobic pillars within channel keep the fluid in the given geometry via capillary forces after the voltage is removed. The posts can also be spaced differently in different regions to help govern fluid shape as is also shown in Kreit *et al*. (2010), but different hydrophobicities to evenly spaced posts could also accomplish it. The capillarity models established here can easily be applied to help predict interface shape and pressure tolerance for such cases.

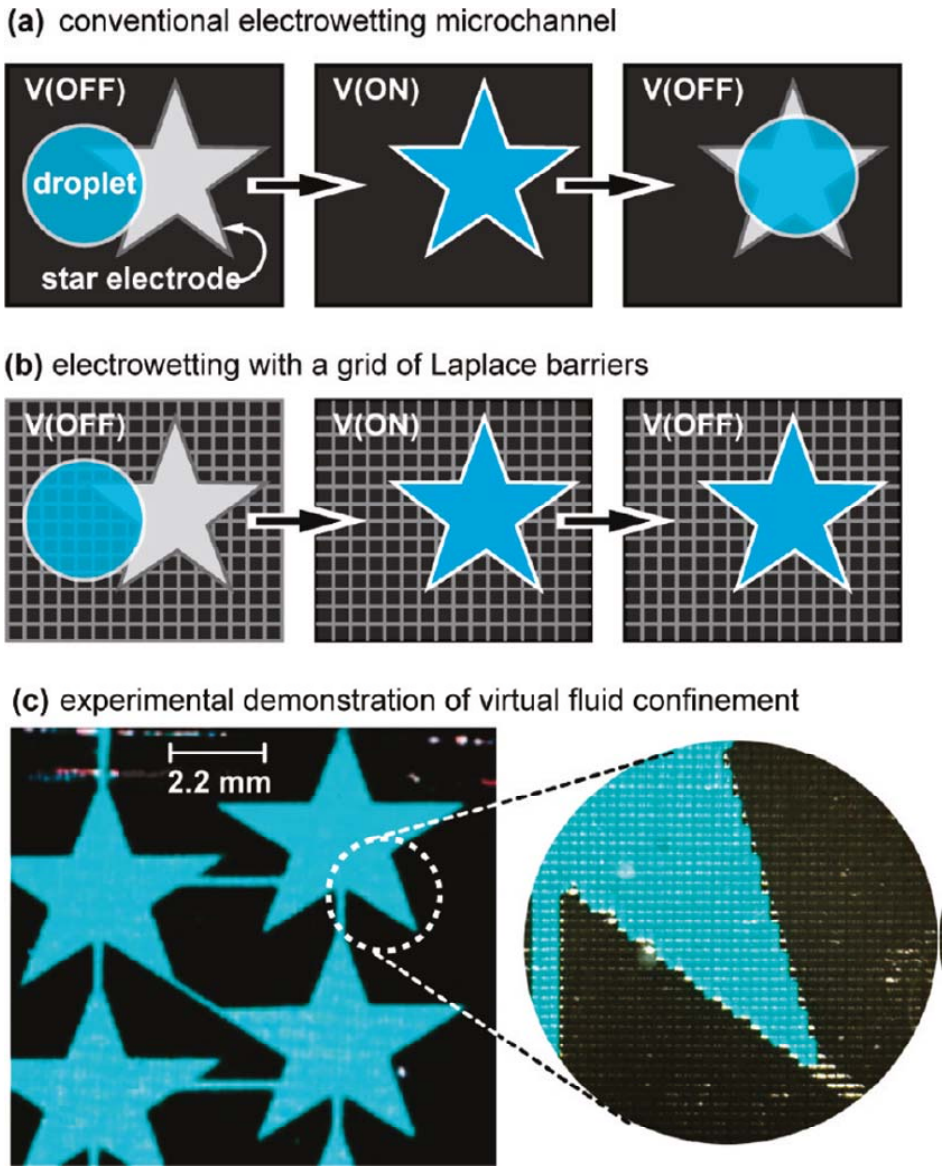

Figure 2.7: (a) Conceptualization of electrowetting in a microchannel without Laplace barriers. (b) Conceptualization of electrowetting in a microchannel with Laplace barriers. (c) Experimental demonstration of electrowetting with Laplace barriers. Image is from the work of Kreit *et al*. (2010).

Quantifying capillarity is also essential in anticipating the gas diffusion layer (GDL) for polymer electrolyte membrane (PEM) fuel cells (also known as proton exchange membrane fuel cells). Numerous recent studies have revealed the importance of the GDL's fibrous microstructure and wettability (i.e., capillarity) on moisture management in PEM fuel cells (e.g.,

Litster *et al*., 2005; Zhou and Wu, 2010; Hao and Cheng, 2010; Caulk and Baker, 2011). Figure 2.8 is the result of a lattice Botlzmann simulation of a 3-D reconstruction of the GDL of a fuel cell from the work of Hao and Cheng (2010). Four stages of water accumulation and penetration are shown (for different times). The accumulation of water on one side of the cell results in an intruding fluid front working its way through the fibrous web. While some hydration is good for proton conductivity, too much water can block the transport of reaction gases (Tuber *et al*., 2003). The lattice Boltzmann method, while an accurate modeling strategy, is computationally expensive, requiring a fully realized three-dimensional mesh of the fibers and surrounding space. One of the models presented in this thesis (Section 5.2) could be modified to this application, and would only require modeling of the air–water interface itself. Capillarity in fibrous materials has also been the subject of extensive research in fiber-reinforced composite materials. Such materials as thermoplastics are made up of fibers, sometimes ordered and sometimes randomly arranged, that are impregnated with a liquid resin that subsequently solidifies, adding rigidity and mechanical strength (e.g., Bayramli and Powell, 1990; Kaptay, 2008; Simcek *et al*., 2009 among many others). The impregnation process is a balance between capillary forces and viscous forces. Essentially, most any conceivable application which utilizes capillary forces that would benefit from specific knowledge of interface shape, position, and behavior could have the models presented in this thesis extended for use in that context.

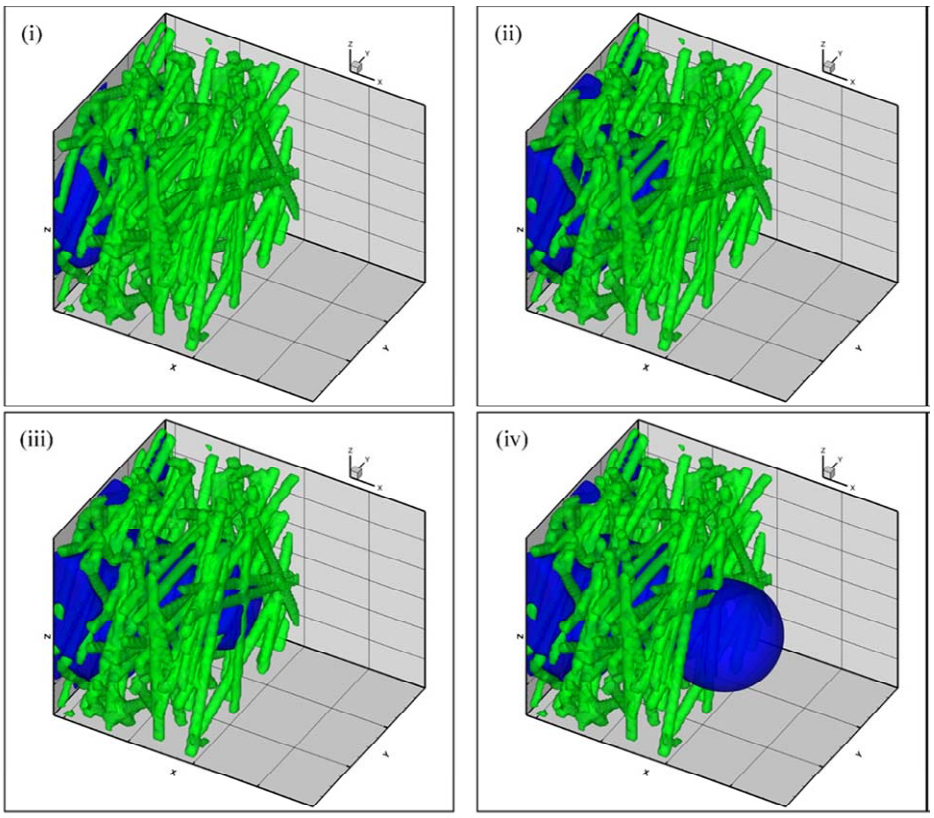

Figure 2.8: Lattice Boltzmann simulation of water accumulation and penetration in the gas diffusion layer of a PEM fuel cell shown at four different times (0.75s, 0.95s, 1.05s, and 1.2s, respectively) from the work of Hao and Cheng (2010).

Finally, fiber coatings with orthogonally laid layers also have utility in the field of aerosol filtration, and have some unique properties in that application. These coatings can serve as a nano-sieve designed and placed on the downstream side of a conventional nonwoven fibrous filter to enhance its performance (i.e., collection efficiency for a given pressure drop). This thesis will also briefly report on an analysis of the performance characteristics of these thin coatings to guide the fabrication process in terms of their microstructural properties, much in the same vein as for a superhydrophobic coating. In particular, there is a correlation we have found such that, for coatings comprised of a given fiber size, there exists a corresponding particle size for which the coating's performance becomes independent of variations in fiber-to-fiber spacing (i.e., coating's non-homogeneity).

Chapter 3

Capillary Models for Fluid Transport in Fibrous Media[3]

3.1 Fluid Height in a Vertical Capillary Tube

Analytic Expressions from Balance of Forces across the Interface

Equation 2.3 is simply a balance of forces in a vertical cylindrical capillary tube, as shown in Figure 3.1. The capillary force around the wall at the air–water meniscus of the tube is balanced by the weight of the column of water raised into the tube. This system assumes that air pressure is the same inside and outside the tube (i.e., the tube and reservoir are open to atmosphere). For any medium in which capillarity applies and the geometry of the system is fixed in the z direction, the balance of forces for vertical height rise can be expressed as

$$A\rho gz = C\sigma\cos\theta \tag{3.1}$$

where the left side represents the downward force due to gravity, and the right side the capillary forces drawing the meniscus upward. Since C and A in this case are merely the circumference and cross-sectional area inside the tube, Equation 3.1 simplifies to the equation for Jurin's height—Equation 2.3.

[3] Some of the contents of this chapter appears in the following publications:

- T.M. Bucher and H.V. Tafreshi, "On applications and limitations of one-dimensional capillary formulations for media with heterogeneous wettability," *Applied Physics Letters* 102, 241606 (2013).
- T.M. Bucher and H.V.Tafreshi, "Modeling air–water interface in disordered fibrous media with heterogeneous wettabilities," *Colloids and Surfaces A: Physiochemical and Engineering Aspects* 461, 323–335 (2014)

This simple case serves as the starting point against which several methods are discussed in this thesis for predicting meniscus height and shape. These methods are respectively described in the following three subsections.

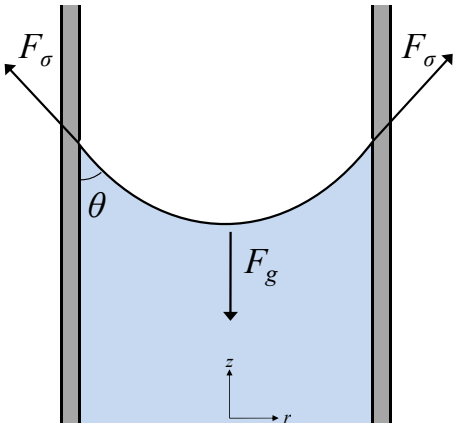

Figure 3.1: Free body diagram of the forces balancing the vertical height rise of liquid in a cylindrical capillary tube.

Simulation of Height Rise via the Volume of Fluid Method

First, we developed a model for meniscus height and shape based on solving the Navier–Stokes equations in the finite volume environment. We use the Volume of Fluid (VOF) method to define regions within a computational domain that are initially comprised of water (the rest being air), and we allow the defined surface and body forces to reconfigure the two fluids into their equilibrium state. During the solution, mass is conserved by allowing each computational cell to have a volume fraction to represent partial water and air content at the location of the interface. The method is similar to the Marker and Cell method, in which case discretized computational cells are either dry or (if containing even one "marker particle" for the other

phase) wet (McKee *et al*., 2008). However, the absolute wet-or-dry cell classification leads to mass conservation issues requiring refining and adapting the mesh near the fluid interface. Marker and Cell also has computational expense comparable to VOF. Due to VOF's computational expense in a fully three-dimensional space, for this task, we take advantage of the simplicity of this particular problem, and model a 2-D axisymmetric plane. The initial configuration of the system is shown in Figure 3.2 below. The central axis of rotation is on the right boundary of the domain. Thus, the thin region on the right represents the capillary tube, while the area outside is the reservoir. The blue and red regions are air and water, respectively. The tube has an inside radius of 2 mm, and a contact angle of 40°. The outside surface of the tube is neutral to air and water. Applying these parameters to Equation 2.3 yields a final height of 5.7 mm. This final height is applied to the VOF model as a height difference between the water level inside and outside the tube.

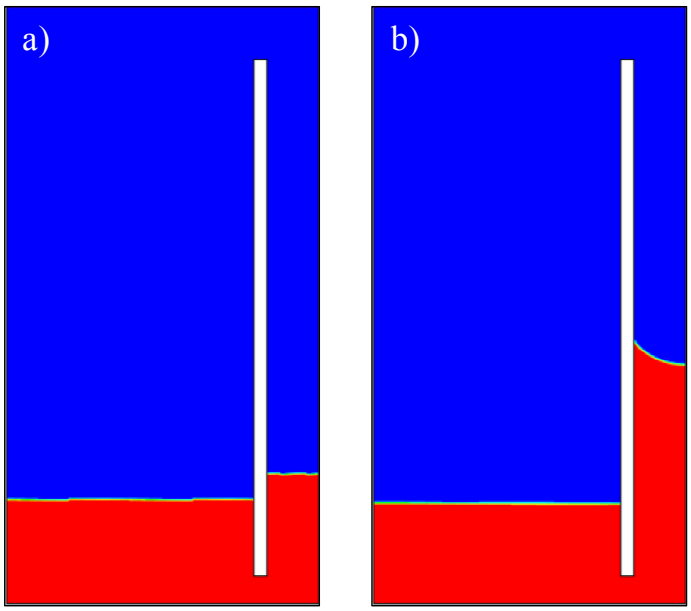

Figure 3.2: 2-D axisymmetric VOF simulation of vertical height rise inside a capillary tube with a radius of 2 mm and a water contact angle of 40°. Figures (a) and (b) represent the initial and final conditions of the system, respectively.

To measure height inside the domain in Figure 3.2, we developed a C++ subroutine or user-defined function (UDF) that reads the height inside and outside the tube and subtracts the difference between them. An additional consideration must be made, however. It can be easily seen in Figure 3.2 that the meniscus inside the tube is not a flat height, but rather has a spherical curvature. The height given by Equation 2.3 corresponds to the equivalent height of a flat cylinder inside the tube that has the same volume as the meniscus in our model. To obtain this equivalent height, our UDF first measures the minimum height of the meniscus z_{min}. It then adds the result of the following equation to that height:

$$z_{add} = \frac{r}{\cos^3\theta}\left(\frac{2}{3}\left(\cos^3\left(90-\theta\right)\right)-\left(\cos^2\left(90-\theta\right)\right)+\frac{1}{3}\right) \tag{3.2}$$

It can be shown that Equation 3.2 gives the volume of the meniscus above z_{min}, and divides it by the area of the tube, yielding the height of a fictitious cylinder with the same volume as the meniscus. Thus, $\bar{z} = z_{min} + z_{add}$ is the height returned by the UDF, and is the singular height Equation 2.3 predicts.

Starting with the initial configuration shown in Figure 3.2a, we performed a dynamic simulation in which the system is allowed to equilibrate on its own, and compared it with Equation 2.5, which was solved using a fourth-order Runge–Kutta method (Mosoodi *et al*., 2013). The result is shown in Figure 3.3, along with the steady-state Jurin's height as a reference. The two curves show very strong agreement. Our model dampens more quickly, but Equation 2.5 assumes an infinite reservoir, whereas our model has a finite reservoir, the feedback oscillations of which dampen the oscillations inside the tube. This dampening is also consistent with experimental comparisons in the literature (Masoodi *et al*., 2013).

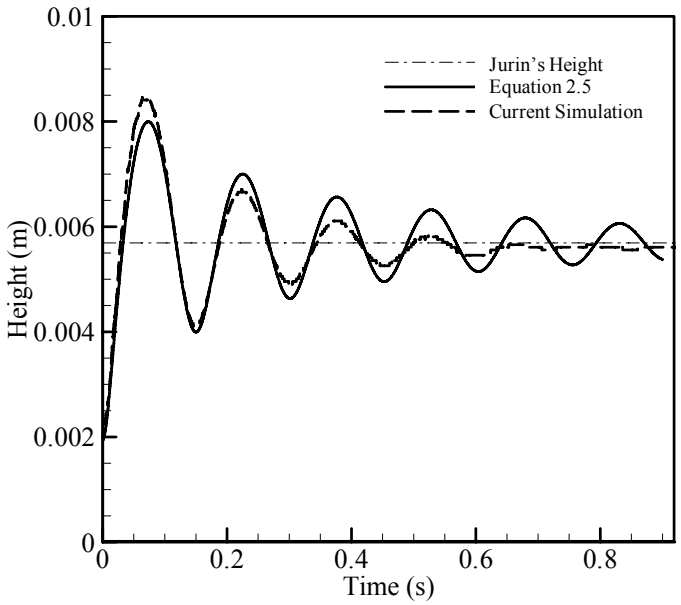

Figure 3.3: Comparison of meniscus rise and settling time between our VOF model and the prediction from Equation 2.5. The steady-state Jurin solution from Equation 2.3 is also shown. The capillary tube has a radius of 2 mm and a contact angle of 40°.

While solving for meniscus shape and height via the VOF simulation has shown strong agreement in simple cases, using it in any other more complicated case can be prohibitively computationally expensive. To address this problem to some degree, we have used the simple case studied in this section to develop a methodology for circumventing the need to generate the full capillary tube and reservoir, and instead modeling only a small window where the meniscus exists. At the inlet to the window, a pressure boundary is applied that corresponds to the appropriate hydrostatic pressure for the remainder of the tube not modeled. The UDF previously written to measure meniscus height is modified to now apply the necessary pressure at the boundary, which can be expressed as:

$$P_{in} = -\rho g\left(z_{min} + z_{add} + B\right) \tag{3.3}$$

Figure 3.4 below illustrates this simplified simulation domain and the height components for the pressure boundary. With this method, of course, one can only predict final meniscus height and shape, not the time it takes to reach it.

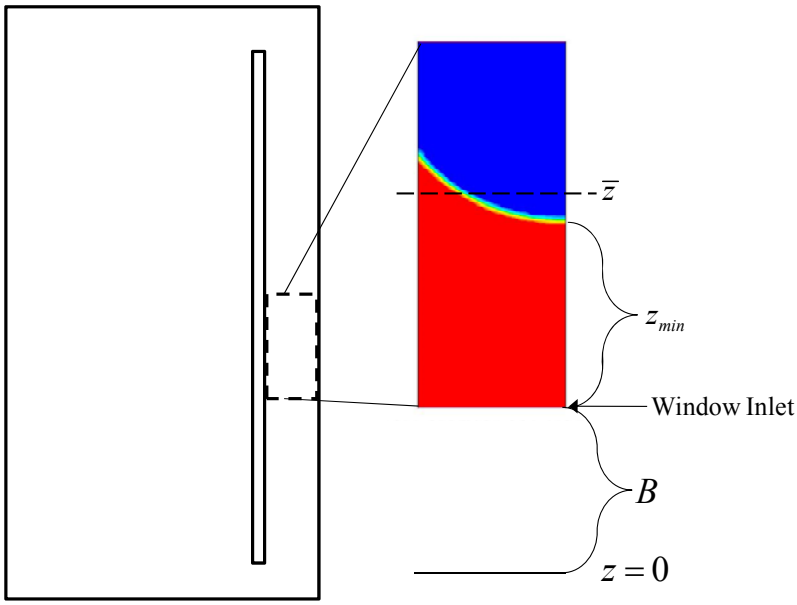

Figure 3.4: Conceptual illustration of modeling a small window of the full capillary tube domain and reservoir. Pressure boundary applied at the inlet is due to the height of the fluid inside the window and the height of the column below it.

The same process of simulating a window with the appropriate pressure boundary was also performed for the case of a hydrophobic tube ($\theta = 140°$ instead of 40°), in which final liquid height inside the tube is lower than that of the reservoir. The illustrations are not shown for the sake of brevity. Table 3.1 shows a comparison of the final heights for hydrophilic and hydrophobic tubes with Jurin's height, both for a full domain with a reservoir and for our simplified window model. While this model has shown utility for simple dynamic cases like the one shown, computational domains will quickly become too complex for this method to continue to be practical to use. We therefore turn to the methods described ahead.

Table 3.1: Comparison of final meniscus height predictions for hydrophilic and hydrophobic capillaries compared with their respective predictions from Equation 2.3. Both the full simulation domain with a reservoir and the simplified window model were tested. Tube has a radius of 2 mm.

	Equation 2.3	Full Domain with Reservoir	% Error	Window Only	% Error
$\theta = 40$	5.691	5.576	2.02	5.558	1.95
$\theta = 140$	-5.691	-5.477	3.76	-5.358	5.85

Simulation of Height Rise by Minimizing Interfacial Energy

If all that is needed is the final steady-state shape and position of the air–water interface in a tube, then there are several other methods one can use that are not as computationally expensive as the dynamic VOF method. So far, we have examined vertical height rise in a tube only through conservation of momentum. One can also view this problem from the perspective of minimizing the energy across the interface, energy due to gravity, surface tension, and the tube's affinity for the liquid, which all contribute to the interface taking a shape with a curvature that keeps these vying energies at a minimum state (de Gennes *et al*., 2004).

To model the meniscus in a tube in this fashion, we employ the Surface Evolver code, an open source code developed by Ken Brakke at Susquehanna University to predict the shape of a liquid interface in response to any given contributions to its surface energy (Brakke, 1996; Brakke and Morgan, 2002). This model is three-dimensional, and employs the finite element method to solve for the energy equation, refining the surface's shape and position after each iteration in order to reduce its energy. Figure 3.5 below shows the final shape and position of the meniscus for the same vertical capillary. Only the interface itself is explicitly modeled. A wireframe of

the tube is shown for illustration purposes. The influence of the tube wall on the tube wall is accounted for in the form of a boundary condition that expresses energy through the integral

$$dE = \sigma \cos\theta \iint dA \tag{3.4}$$

where $\iint dA$ represents the surface area of the tube interior below the water column (in this case).

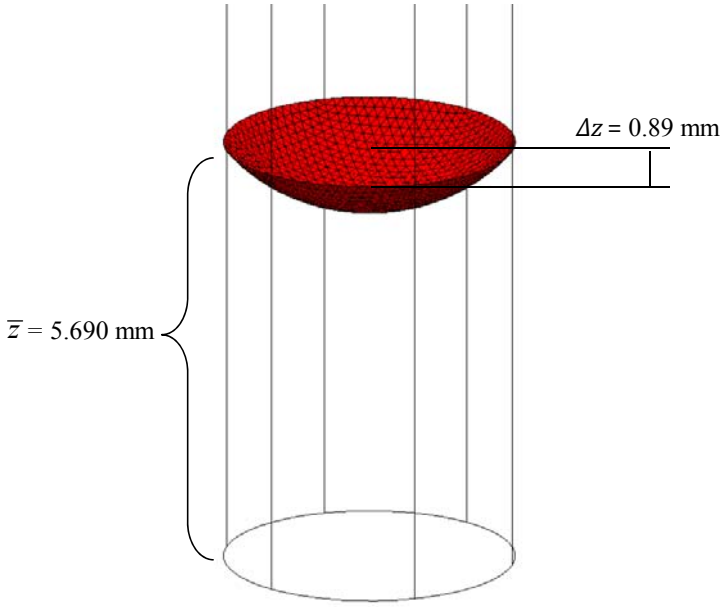

Figure 3.5: Final meniscus shape and height in a vertical capillary tube as predicted by surface energy minimization via the Surface Evolver code. Tube has a radius of 2 mm and a water contact angle of 40°.

As can be seen in Figure 3.5, the area-averaged height of the meniscus is 5.690 mm, about 0.02% error with Equation 2.3, showing near-perfect agreement with analytical force balance predictions. This agreement can be made stronger by refining the mesh to a higher density, but it comes at the expense of computation time. It should also be noted that this method required only several minutes to complete on a conventional desktop computer. Solving the system using VOF in a 2-D axisymmetric simulation domain required several days for the simplified window model, and over one week for the full domain with a reservoir.

Simulation of Height Rise by Solving for Interfacial Curvature

The third numerical method for height rise uses Equation 2.3, but expanded into a more general form to solve for local meniscus height as a function of x and y. This more general form is given as

$$F(x,y) = a^2\left(\vec{\nabla}\cdot\hat{n}\right) \tag{3.5}$$

where $F(x,y)$ is the local height of the meniscus, and $\hat{n}$ is its unit normal vector. Defining the level set function $G(x,y,z) = F(x,y) - z$ for which $G = 0$ along the meniscus, we obtain the unit normal vector as $\hat{n} = \nabla G / |\nabla G|$, and Equation 3.5 becomes:

$$F\left(F_x^2 + F_y^2 + 1\right)^{3/2} = a^2\left(\left(1+F_y^2\right)F_{xx} + \left(1+F_x^2\right)F_{yy} - 2F_xF_yF_{xy}\right) \tag{3.6}$$

where the subscripts of x and y represent respective partial derivates of $F(x,y)$. A similar equation was also derived for meniscus shape in Pozrikidis (2010). This equation is solved in finite element space using the gradient descent method (the FlexPDE software from PDESolutions Inc.), with a boundary condition along the tube given by $|\nabla F| = \cot\theta$. Expressing Equation 2.3 in the form of Equation 3.6 has the advantage of being applicable for any geometry with constant cross-sectional area, not just a tube. Figure 3.6 below shows the solution of the same case as in the previous two subsections given by the solution of Equation 3.6. The area-weighted average height is equal to 5.642 mm, again, showing very good agreement with the prediction on Equation 2.3. A weakness of this method, however, is that Equation 3.6 requires the geometry to have a constant cross-sectional area, i.e., one that does not change in the z-direction.

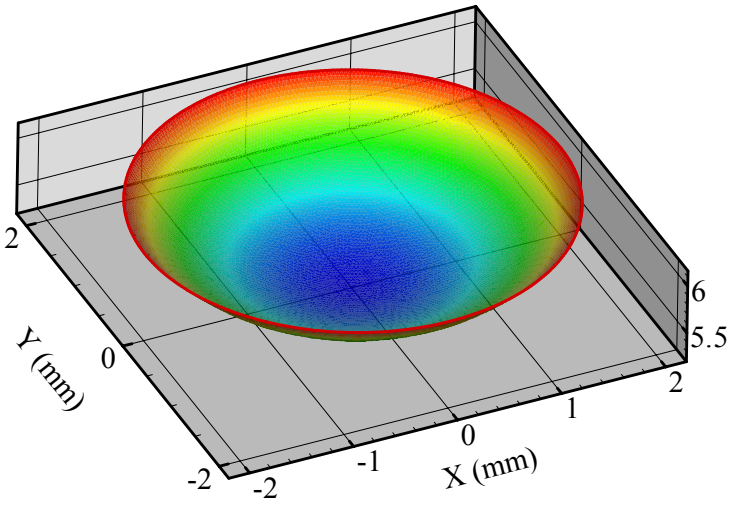

Figure 3.6: Meniscus height (mm) inside a vertical capillary tube as a function of *x* and *y* found by solving Equation 3.6. The tube has a radius of 2 mm and a water contact angle of 40°.

In this section, we have established three different solution methodologies that will be used at different points in the remainder of this thesis. Here, we have benchmarked the methods against the simple case of height rise in a vertical tube, a case with a simple analytic solution, and found all three to be in good agreement. These methods will be used again, in part or as a whole, and comparison with analytical expressions as well as with each other will be performed wherever possible.

3.2 Capillary Pressure for Fluid Transport Parallel to Fibers

Fiber Arrays with Uniformly Distributed Properties

At this point, we add a level of complexity to the analysis of capillarity that has only been considered by our group: explicitly modeling more than one fiber wettability (i.e., contact angle) in a single medium. We use the subject of capillary height rise to initially examine this, this time for the case of vertically-oriented parallel fiber bundles. We start with this geometry in order to

remove the complication of varying cross-sectional area for the moment, and isolate the effect of bi-component fiber composition. Recall from Chapter 2 that relations exist that can apply capillary pressure to dynamic models (see Equations 2.4 and 2.5 for example) when capillary information is represented as if from a single vertical capillary tube (Washburn, 1921; Fries and Dreyer, 2008 a and b, Marmur, 1987, Hyvaluoma *et al*., 2006). We will show through the balance of forces and accompanying numerical data that a system of vertical parallel fiber bundles comprised of dissimilar fibers can be converted into a fictitious capillary tube with properties corresponding to those of the given fiber bundle.

Figure 3.7 shows a free-body diagram of the forces around a single fiber that lies in an array of parallel fibers. Steady-state height rise z of such a system can be expressed as a function of other relevant system parameters:

$$z = f\left(\varepsilon, d_1, d_2, ..., \theta_1, \theta_2, ..., n_1, n_2, ...\right) \tag{3.7}$$

Considering the 2×2 unit cell shown on the top right of Figure 3.7, the force balance of Equation 3.1 can be adapted not only to such a domain where only one fiber type (and size) exists, but also when two or more fiber types exist. Expressing Equation 3.1 accordingly in terms of Equation 3.7 when two types of fibers are in the domain, one obtains:

$$\bar{z} = \frac{4\sigma\left(n_1 d_1 \cos\theta_1 + n_2 d_2 \cos\theta_2\right)}{\rho g\left(1/\varepsilon - 1\right)\left(n_1 d_1^2 + n_2 d_2^2\right)} \tag{3.8}$$

It is worth mentioning that Princen (1969) performed force-balance analysis on vertical parallel cylinders, and Equation 3.8 simplifies to the relation developed in that work when only one fiber type exists in the domain. Rearranging Equations 2.3 and 3.8, one obtains

$$\frac{\cos\theta_{cap}}{d_{cap}} = \frac{\left(n_1 d_1 \cos\theta_1 + n_2 d_2 \cos\theta_2\right)}{\left(1/\varepsilon - 1\right)\left(n_1 d_1^2 + n_2 d_2^2\right)} \tag{3.9}$$

Examining Equation 3.9 reveals that this equation is in fact comprised of two more familiar equations, a weighted averaging of cosines of the two contact angles for the cosine of equivalent contact angle θ_{cap}, and the classical hydraulic diameter for equivalent capillary diameter d_{cap}, i.e.,

$$\cos\theta_{cap} = \frac{n_1 d_1}{n_1 d_1 + n_2 d_2}\cos\theta_1 + \frac{n_2 d_2}{n_1 d_1 + n_2 d_2}\cos\theta_2 \tag{3.10}$$

$$d_{cap} = 4\frac{A}{C} = \left(\frac{1}{\varepsilon} - 1\right)\frac{n_1 d_1^2 + n_2 d_2^2}{n_1 d_1 + n_2 d_2} \tag{3.11}$$

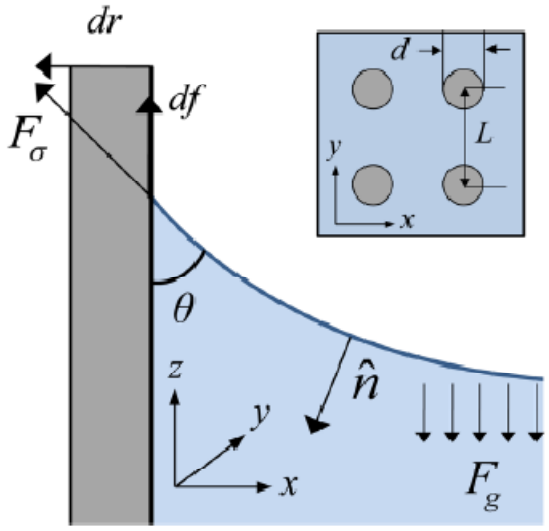

Figure 3.7: Free-body diagram of the forces acting along a fiber in a vertical array of parallel fibers. The top right shows an overhead view of a 2×2 unit cell of fibers.

One therefore can use Equations 3.10 and 3.11 together with Equation 2.3 to predict a fluid's height rise, or Equation 2.5 (among others) to predict a fluid's radial horizontal spread in multi-component media. We model this relation first using Equation 3.6, which, recall, is the generalized Young–Laplace equation that solves for local meniscus height. The boundary

condition around the fibers is $|\nabla F|_{fib} = \cot\theta$, and periodic boundary conditions are assigned to the lateral sides of the domain. We obtain an average height rise from the solution of Equation 3.6 by taking the integral of local height over the domain (equal to volume) and dividing it by cross-sectional area.

Aside from the ordered 2×2 unit cells, we have also compared the solution of Equation 3.6 with that of Equation 3.8 for fiber bundles with random fiber placement and two sets of fiber properties homogeneously distributed. For such random-fiber structures, the domains are larger for improved statistical relevance, and a minimum inter-fiber distance of $d_f / 3$ is enforced in order to avoid additional capillary effects that occur in corners with small angles (Ponomarenko *et al.*, 2011; Weislogel, 2012). Figure 3.8 shows an example of local height values obtained from solving Equation 3.6, in which a medium with $\varepsilon = 0.15$ and $d_f = 10$ μm is considered. The structure also has a bimodal contact-angle distribution with half the fibers having $\theta_1 = 45°$, and the other half $\theta_2 = 85°$. The z-axis in the contour plot shows local height in mm. We have compared predictions of an ensemble of 1-D and 2-D force-balance calculations for media with SVFs from 5–15%, fiber diameters from 5–25 μm, and contact angles from 25°–85°, allowing both for unimodal and bimodal fiber size and component distributions. We observed good agreement (within 10% margin of error) between the meniscus height of Equation 2.3 and the average meniscus height of Equation 3.6 for all microstructure property combinations considered. We performed our calculations not only on unit cells (Figure 3.7), but also on larger domains, in which a greater number of fibers are distributed randomly (Figure 3.8a).

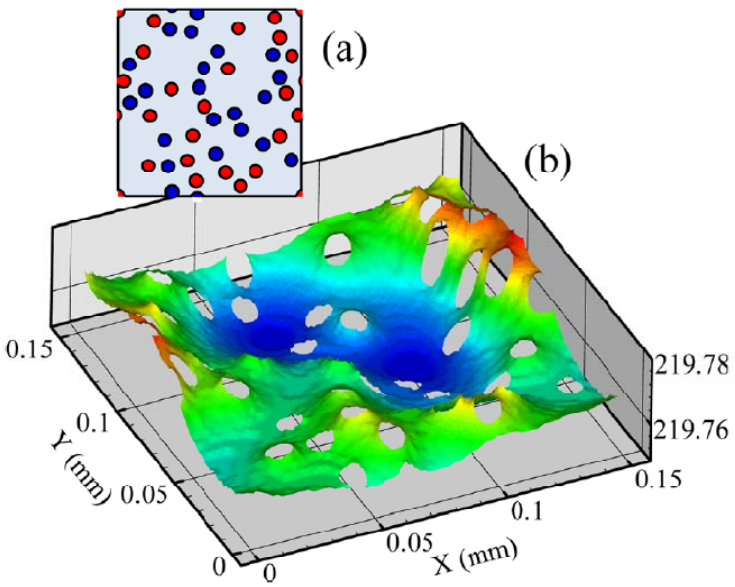

Figure 3.8: (a) Sample computational domain with random fiber spacing. $\varepsilon = 0.15$, $d_f = 10$ µm, $\theta_1 = 45°$ (red fibers) and $\theta_2 = 85°$ (blue fibers); (b) contour plot of local meniscus height (mm). Equation 3.1 predicts height rise of 208.5 mm for this medium, about 5% difference from Equation 3.6.

In Figure 3.9, we illustrate the overall effect of bimodality on capillarity, plotting height rise as a function of number fraction of coarse fibers n_c. For all structures, we considered an SVF 10% and a fine fiber diameter of 10 µm (the parameter R_{cf} refers to the size ratio between coarse and fine fibers). It can be seen that capillarity reduces sharply with the introduction of larger fibers, and more so the larger the coarse fibers. This is because with the available solid volume being consolidated into fewer larger fibers, the capillary force is left with less solid surface area over which to act. This is also the case for structures containing only one larger fiber size (Figure 3.9 when $n_c = 1$).

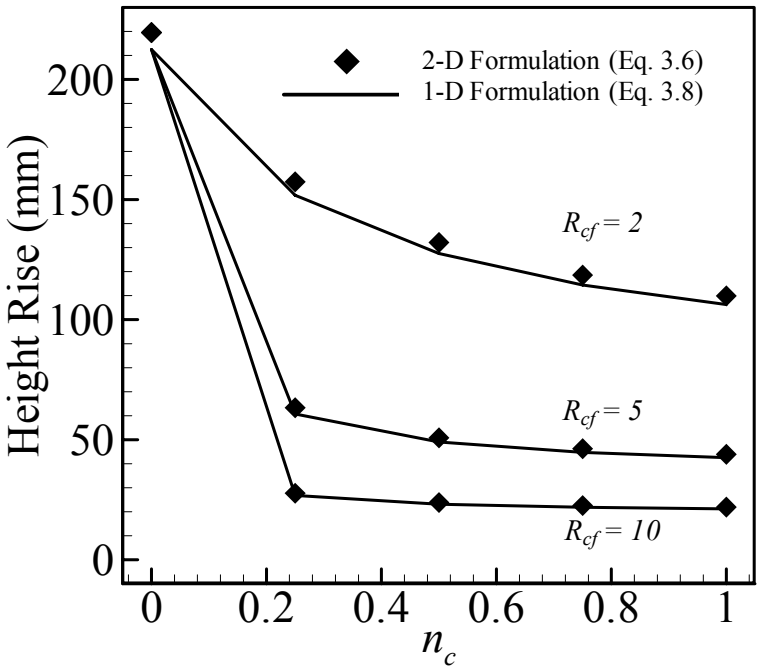

Figure 3.9: Capillary height rise as a function of coarse fiber fraction n_c. Solutions for both 1-D average height (Equation 3.8) and average 2-D height $\overline{F}$ (Equation 3.6) are shown. For all structures, SVF = 0.1, d_f = 10 μm, and θ = 50°. R_{cf} is the size ratio between coarse and fine fibers.

Fiber Arrays with Non-Uniformly-Distributed Properties

The agreement of Equation 3.6 using this method with analytical predictions becomes strained, however, when a structure is produced in which the distribution of its two property sets is not uniform. Such a case is shown in Figure 3.10 below. The figure shows a 7×7 array of parallel fibers in which the fibers lining the outside are hydrophilic by a given degree, and the twenty-five inside fibers are hydrophobic by the same degree. Symmetry boundaries line the domain borders. The result, while near zero height rise relative to results in the other cases shown, is not in as close agreement with Equation 3.8 as the homogeneous cases, and fluctuates when varying mesh density.

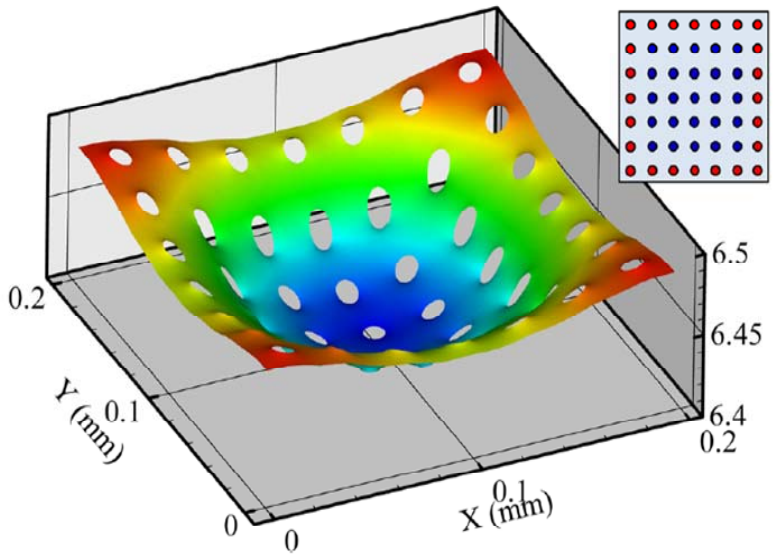

Figure 3.10: Contour plot of solution of Equation 3.6 for local height (in mm) for a square 7×7 array of fibers in which fibers with θ_1 = 60° line the boundaries of the structure, and those with θ_2= 120° are clustered in the middle. Conceptual layout to the right of the plot is colored with red and blue fibers for θ_1 = 60°, and θ_2 = 120°, respectively. The array has a SVF of 0.1, and a unimodal fiber diameter of 10 μm.

To examine the disparity of Equation 3.6 more closely, we revisit the method of solving for meniscus shape and position via minimization of energy across it. Figure 3.11 shows the equilibrium meniscus shape obtained via this method. As can be seen, the meniscus roughly formed the same shape for both methods, with a top-to-bottom height difference of about 0.1 mm. The area-averaged height can be obtained by reading the total volume of the column and dividing by the cross-sectional area of the array. Doing so yields an average height of -3.528 mm. Solving Equation 3.6 for this domain would give a height of -3.369 mm, less than 5% error between results.

Figure 3.11: Equilibrium meniscus shape and position for the structure from Figure 3.10 solved through minimization of interfacial energy. Area-averaged meniscus height is equal to -3.528 mm, less than 5% error with Equation 3.1. The array has a SVF of 0.1, and a unimodal fiber diameter of 10 µm. The outside fibers have a water contact angle of 60°, and the inside fibers a water contact angle of 120°.

The energy minimization method shows close agreement with analytical predictions even for structures with non-uniform properties.

3.3 Fluid Transport Perpendicular to Fibers: The Full Morphology Method

Our earliest work involving water intrusion simulations is performed using the Full Morphology (FM) method, first developed by Hazlett (1995) and later used by Hilpert and Miller (2001) and Becker *et al*., (2008). The FM method is a voxel-based approach. A voxel is the smallest unit of resolution within a given simulation domain, and is recognized as being fully occupied by one of three possible domain constituents: a solid fiber (blue in Figure 3.12), wetting phase (clear in Figure 3.12), or non-wetting phase (red in Figure 3.12). In the FM

method, a quasi-static distribution of liquid and gas (water and air in the present work) is calculated in a 3-D domain at incremental capillary pressure values. When calculations are carried out for an adequate range of capillary pressures, a relation between capillary pressure and liquid (or gas) saturation is obtained. The FM method uses a sphere-caging algorithm, and has also been used for calculation of pressure–saturation relationships in fibrous media with different microstructures (Jaganathan *et al*., 2009; Ashari and Tafreshi, 2009b), as will also be shown later in this thesis.

The algorithm begins by considering one face of a given cubic domain as the non-wetting reservoir (the top face in Figure 3.12). For each incremental pressure rise in the non-wetting reservoir, the FM algorithm determines a minimum pore radius (i.e., sphere radius r_{sph}) using the Young–Laplace equation (Equation 2.2), and examines every voxel in the domain for two conditions: one, a voxel is not occupied by a fiber, along with every voxel around it within a distance of r_{sph}; two, an unbroken path exists between that voxel and the reservoir face into which other spheres of at radius r_{sph} can fit in the same manner. If these two conditions are met, then a sphere is placed in the domain with that voxel as its center, with a radius equal to the distance between the voxel and the nearest solid fiber. A sphere must be connected via other spheres to the reservoir. The overlying spheres form the non-wetting fluid continuum in the domain. This process is repeated for every following pressure increment, with a smaller r_{sph} used each time pressure is raised. Obviously, as is the case in an actual fluid drainage experiment, the non-wetting phase can only penetrate into a porous medium as deeply as the most constrictive spaces therein—the size and distribution of which being a function of the coating's microstructure—allow (the famous ink-bottle effect) (Jaganathan *et al*., 2008b). The FM method

is implemented in the GeoDict code developed by the Fraunhofer Institute ITWM, Germany, and is used for the simulations presented here.

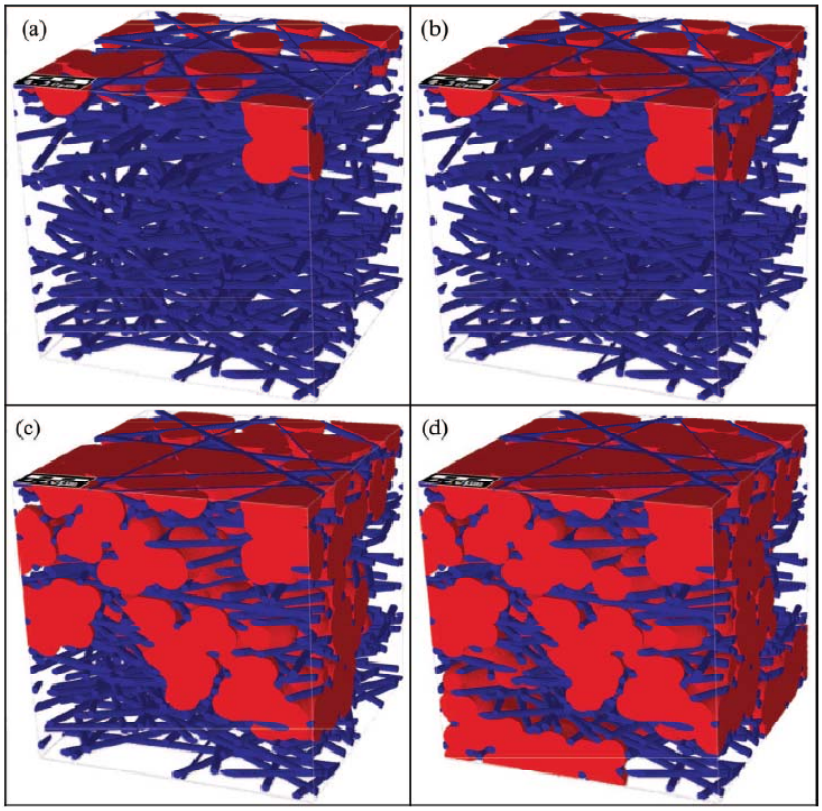

Figure 3.12: A visualization of the Full Morphology simulation method at four different corresponding capillary pressures. Corresponding pressures are: (a) 2949.15 Pa, (b) 3411.75 Pa, (c) 3866.65 Pa, and (d) 4046.5 Pa. The fibrous medium shown has a solid volume fraction of 0.1, fiber diameter of 10 μm, and a thickness of 480 μm.

Figure 3.12 illustrates different stages of water intrusion simulation corresponding to four different applied pressures. The spheres are overlaid with one another to form a virtual fluid continuum within the medium. Even if larger spaces exist inside the medium, the non-wetting front will not be able to reach them if a prohibitively tight space must first be cleared. When no more spheres of the prescribed radius can be fitted into the available domain, non-wetting-phase saturation is then calculated based on the volume of space thus occupied. The process is repeated using a smaller sphere radius, corresponding to the next ascending input capillary pressure value.

This method provides a means of relating capillary pressure to fluid content, but its use of spheres with radius dictated by Equation 2.2 means that the method is only an approximation of the pressure required to force a non-wetting phase to penetrate into a fibrous structure. However, it is the only useable streamlined approach for doing so, and is the only computationally reasonable method available for randomly oriented fibrous media. It cannot be used to investigate the exact shape of the air–water interface, and, due to its simplified use of Equation 2.2, can only represent fibers of a single fluid affinity (contact angle) in a single structure.

While the FM method is typically executed from the direction of drainage (beginning with a fully saturated medium and pressurizing with the non-wetting phase), the results can also be applied to absorption, as the vacuum drawn in the wetting phase at the fluid front equal to the capillary pressure applied for drainage. Figure 3.13 shows the effect of SVF and fiber diameter on $p_c(S)$. It can be seen in Figure 3.13a that capillary pressure is stronger (more negative) when SVF is higher (i.e., lower porosity, and therefore tighter spaces for higher capillarity), and in Figure 3.13b we see that capillarity is stronger when the fibers are smaller (i.e., greater surface are for given solid volume, concurs with force balance analyses in Chapter 2).

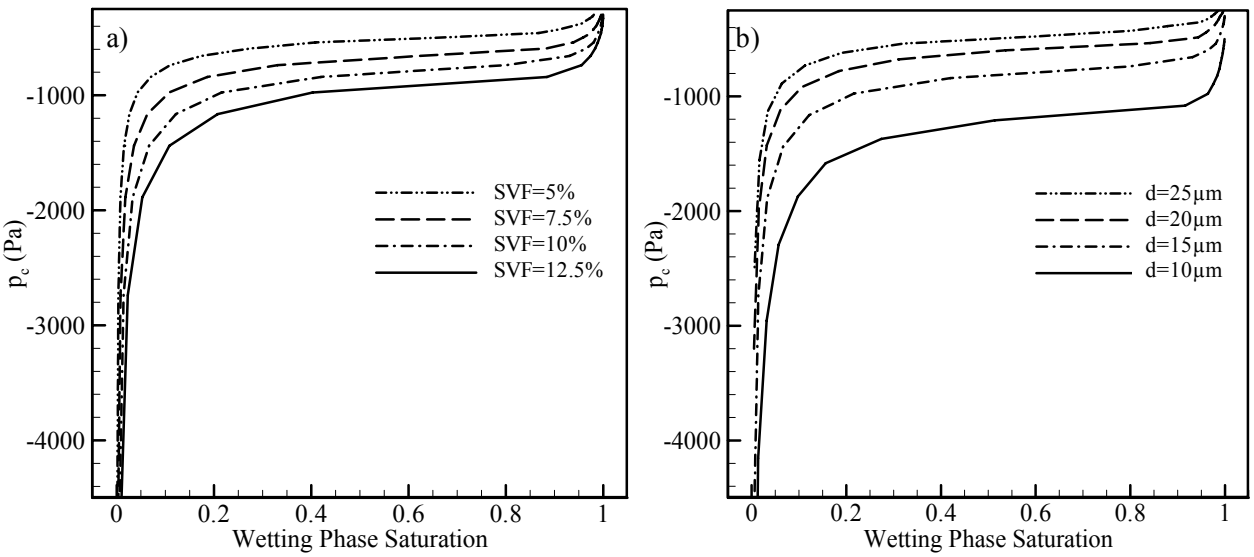

Figure 3.13: Capillary pressure versus saturation using the FM method for modeled virtual fibrous media with dimensions of 1500×1500×1000μm: (a) varying SVF while fiber diameter is held at 15μm, (b) varying fiber diameter while SVF is held at 10%. The surface tension and wetting-phase contact angle used are equal to 0.7275 N/m and 80 degrees, respectively, for both plots.

The FM approach is useful for predicting the effect of microstructure on capillary pressure in fibrous media of arbitrary configuration. However, being able to predict the exact shape of the air–water interface would still be desirable, but requires a different modeling technique such as that of Lobaton *et al*. (2007) and Pozrikidis (2010), who have established meniscus shape models for simple cases with ordered geometry based on the constant-mean-curvature concept, which is difficult to apply to 3-D disordered fibrous surfaces. In the next section we will elaborate on a model we have since developed for unidirectional fiber bundles.

3.4 Horizontal Parallel Fibers with Heterogeneous Wettability

In the concern of devising a capillary pressure model that takes into account the forces in play, meniscus shape, and effect of multiple wettabilities in a single fibrous structure, we have

developed a new simulation method founded on the basis of analytical equations derived from the balance of forces acting on an air–water interface between two fibers. The novelty of the method in this section is: 1) it is computationally fast, and 2) it can be used to calculate the pressure required for a fluid to penetrate into fibrous media comprised of fibers with dissimilar wettabilities or diameters. These capabilities allow one to conduct computationally affordable parameter studies for media with varying properties to construct easy-to-use correlations for capillary pressure, or custom-design the microstructure of a capillaric system to meet the needs of its specific application (e.g., GDL in fuel cells, microchannels containing hydrophobic or hydrophilic microposts, superhydrophobic fibrous coatings for self-cleaning, or hygiene products among many others). The major, perhaps only, limitation of the analytical simulation methods proposed here is that it considers a 2-D representation for the fibrous media (most accurate for fluid penetration into fiber bundles).

We will first explain the equations for calculating the position and curvature of a meniscus between two dissimilar fibers. Then we will explain how our algorithm produces an air–water interface in a disordered medium and calculates saturation. We will then expand on the capillary pressure–saturation relationship which began in the last section, establishing the necessary constraints on domain size to ensure statistical confidence, and comparing the results of our simulations with correlations in the literature. This will be followed by a parameter study performed for various microstructure properties but with uniform wettability before we finally explore the effects of heterogeneity in the media's wettability. We will finish this section with an easy-to-use expression for converting the capillary pressure–saturation obtained for a heterogeneous fluid–solid system to another.

Balance of Forces over Air–Water Interface between Two Fibers

We begin by considering a stable meniscus between two parallel fibers, the fibers each having their own unique contact angle (see Figure 3.14a). This meniscus is obtained by applying a capillary pressure p_c to the non-wetting phase (air in this case) above the fibers, and possesses a constant mean curvature r_m given by the Young–Laplace equation simplified for the case of parallel walls:

$$r_m = \frac{\sigma}{p_c} \tag{3.13}$$

Recall σ is equal to surface tension. The applied pressure is balanced by surface tension forces acting along the fibers:

$$p_c L(s_f - r_f \sin\alpha_1 - r_f \sin\alpha_2) = \sigma L\left(\cos(3\pi/2 - \alpha_1 - \theta_1^{nw}) + \cos(3\pi/2 - \alpha_2 - \theta_2^{nw})\right) \tag{3.14}$$

Where the left-hand side is the product of pressure and cross-sectional area between the fibers, and the right-hand side is the z-component of the surface tension force times the interface contact perimeter—i.e., two parallel fibers of length L (see Figure 3.14 for remaining terms). Rearranging, cancelling L, and substituting a more convenient trigonometric expression, we obtain

$$p_c = -\sigma \frac{\sin(\alpha_1 + \theta_1^{nw}) + \sin(\alpha_2 + \theta_2^{nw})}{s_f - r_f\left(\sin\alpha_1 + \sin\alpha_2\right)} \tag{3.15}$$

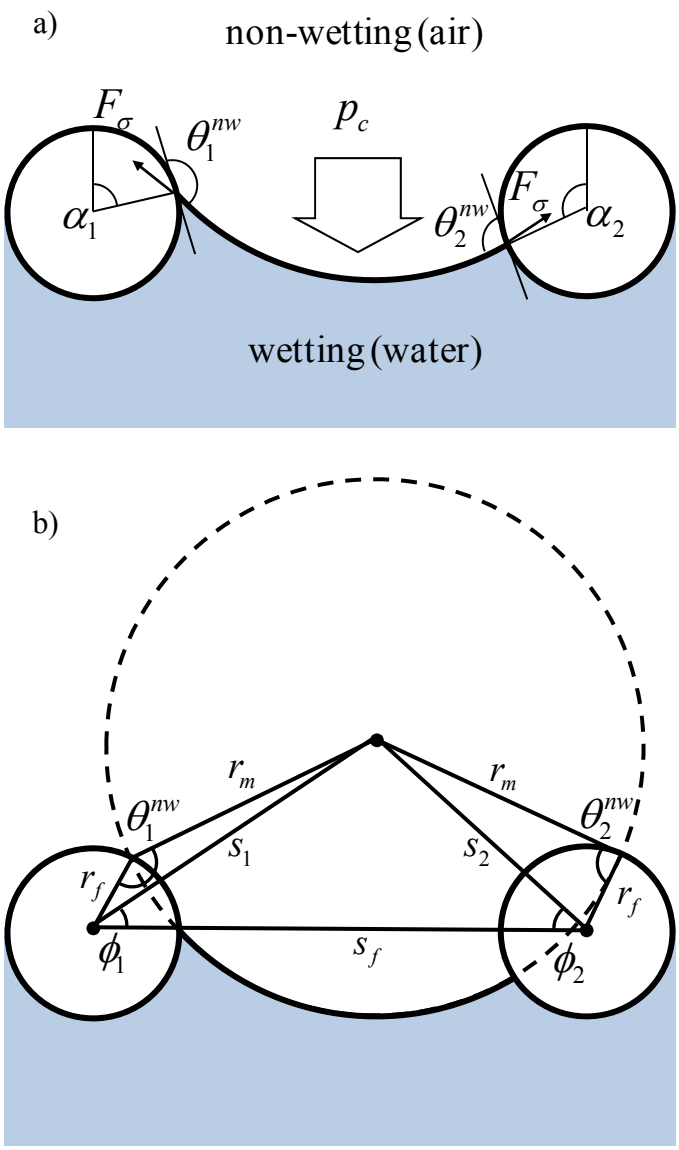

Figure 3.14: (a) A free body diagram illustrating the balance of forces across a stable meniscus between two parallel fibers with different contact angles; (b) illustration of the means by which one can geometrically determine the location of the meniscus in relation to the two surrounding fibers by considering the meniscus as an arc in a circle of radius r_m.

The physics of the system is similar to that of a meniscus across posts or fibers on a superhydrophobic surface (Emami *et al*., 2011a, 2011b, 2012), but with the wetting and non-wetting fluids reversed. The angles α_1 and α_2 are not known explicitly, and Equation 3.15 alone is not sufficient to obtain them. However, the constant mean-curvature principle (Equation 3.13)

establishes a geometric relationship between α_1 and α_2, i.e., a fictitious circle with radius r_m between the fibers (along which the stable meniscus would be an arc) intersects each of the two fibers so as to satisfy the contact angles θ_1^{nw} and θ_2^{nw} (see Figure 3.14b). The geometry of the air–water interface at equilibrium results in the formation of three triangles between the fibers and the fictitious circle: one with the centers of the fibers and the circle as its vertices, and one between each fiber and the center of the circle, the third vertex of each being the point where the two adjoining circles intersect. Of the sides and angles labeled in Figure 3.14b, s_f, r_f, and r_m are known. It is also known that the two angles in the diagram where r_f and r_m meet for each pair of fibers are equal to θ_1^{nw} and θ_2^{nw}, respectively. Using the law of cosines, one can determine the value of all the remaining unknowns:

$$s_1 = \sqrt{r_f^2 + r_m^2 - 2r_f r_m \cos\theta_1^{nw}} \tag{3.16a}$$

$$s_2 = \sqrt{r_f^2 + r_m^2 - 2r_f r_m \cos\theta_2^{nw}} \tag{3.16b}$$

$$\phi_1 = \cos^{-1}\left(\frac{s_1^2 + s_f^2 - s_2^2}{2s_1 s_f}\right) \tag{3.17a}$$

$$\phi_2 = \cos^{-1}\left(\frac{s_2^2 + s_f^2 - s_1^2}{2s_2 s_f}\right) \tag{3.17b}$$

With the coordinates of the center of the fictitious circle known (Equations 3.16a–3.17b), α_1 and α_2 can be determined, and then inserted back into Equation 3.15 to verify that they indeed satisfy the balance of forces (i.e., this meniscus can physically exist). In all cases performed for this work, α_1 and α_2 satisfy Equation 3.15.

While Equation 3.15 must be used in conjunction with Equations 3.16a–3.17b to find the meniscus shape at an arbitrary capillary pressure p_c, this equation alone can be used to calculate the maximum pressure p_c^* at which a stable air–water interface can exist, the so-called critical pressure, as will be discussed in Chapter 5. This is done by solving the system of equations given below for α_1 and α_2, and consequently, p_c^*.

$$\left.\frac{\partial p_c}{\partial \alpha_1}\right|_{p_c^*} = -\sigma \frac{\cos\left(\alpha_1 + \theta_1^{nw}\right)}{s_f - r_f\left(\sin\alpha_1 - \sin\alpha_2\right)} - \sigma r_f \cos\alpha_1 \frac{\sin(\alpha_1 + \theta_1^{nw}) + \sin(\alpha_2 + \theta_2^{nw})}{\left(s_f - r_f(\sin\alpha_1 - \sin\alpha_2)\right)^2} = 0 \quad (3.18a)$$

$$\left.\frac{\partial p_c}{\partial \alpha_2}\right|_{p_c^*} = -\sigma \frac{\cos\left(\alpha_2 + \theta_2^{nw}\right)}{s_f - r_f\left(\sin\alpha_1 - \sin\alpha_2\right)} - \sigma r_f \cos\alpha_2 \frac{\sin(\alpha_1 + \theta_1^{nw}) + \sin(\alpha_2 + \theta_2^{nw})}{\left(s_f - r_f(\sin\alpha_1 - \sin\alpha_2)\right)^2} = 0 \quad (3.18b)$$

Thus, before attempting to calculate the shape of a meniscus between two fibers with arbitrary properties, we can establish whether or not a stable meniscus can exist at the given pressure in the first place, as well as predict where and at what pressure the interface from an earlier pressure input will break more deeply into the medium.

Interface Tracking Algorithm for Disordered Media

With the equations for the meniscus shape between two fibers in hand, in this section we present our algorithm for establishing an interface across an entire domain consisting of multiple fibers arranged arbitrarily.

Random fibers are generated until the desired solid volume fraction (SVF) is reached. Figure 3.15 illustrates a sample structure with an SVF of $\varepsilon = 0.2$ and a fiber diameter $d_f = 10$ μm. The fibers can possess one of two (or more if desired) contact angles with a given percent population of each. The current study only considers bi-component fibrous media for the sake of

brevity, but the model can be applied to consider any degree of fiber diversity. Periodic boundary conditions (PBCs) are placed on the left and right side of the domain, i.e., any fiber that crosses one of these boundaries is continued across the other boundary. PBCs allow our computational domain to act as a representative area element in a much larger structure. The PBC also applies for the menisci that will be generated, as an interface that crosses the boundary will continue on the other side of the domain without interruption. In addition, a minimum space between the fibers is enforced (one tenth of fiber diameter), in order to prevent direct fiber-to-fiber contact and its associated complications. Obviously, fibers in a tow are not perfectly parallel, i.e., there are regions with fiber crossovers. However, in the absence of quantitative information about the frequency of occurrence and the area of each crossover (fiber-to-fiber angle at crossovers) the effects of such irregularities cannot be quantified either computationally or even experimentally. The effects of such irregularities thus have to be treated like statistical uncertainty or noise added to the performance obtained for more idealized structures.

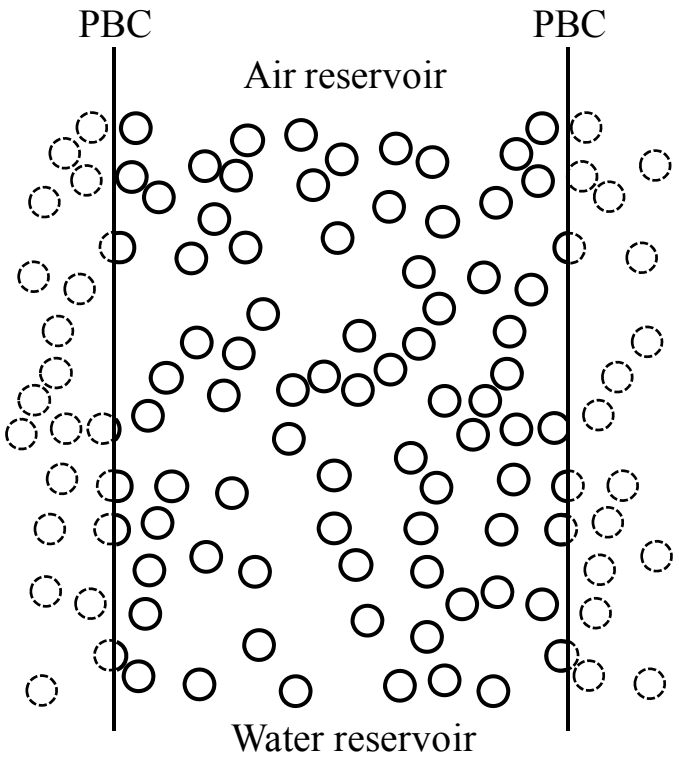

Figure 3.15: Typical simulation domain and boundary conditions for our random fiber spacing model.

Given a computational domain with established microstructural parameters, we can describe the motivation behind our interface-locating algorithm as follows: in a fibrous medium configured as defined, if a stable and unbroken interface can exist somewhere within the structure at a given applied pressure, then that interface would follow a path beginning and ending across the same point along the periodic boundary, and would exist across the closest periodic boundary to the penetrating fluid (as close to the top of the domain as possible). With this driving principle, it is then possible to represent such an interface by building a bridge across the domain comprised of a series of interlinked menisci, starting from one side of the domain and ending up at the other, each one satisfying Equation 3.15, and with each shape calculated using the method described along with Figure 3.14.

Figure 3.16 shows a flowchart for the general overview of the algorithm. To determine a starting point, every pair of fibers for which each fiber is on the opposite side of the boundary from the other is recorded. Equation 3.15 and Equations 3.18a and 3.18b are then used to confirm whether or not a stable meniscus can exist between each pair at the given input pressure. Of the pairs that remain, they are sorted in descending order based on the y-intercept of s_f between each pair. For the first pair of fibers on the list, a tentative meniscus shape is calculated. The algorithm then performs a check to make sure no other fiber intersects with the meniscus that was just drawn. If a fiber is in the way, then the meniscus is recalculated to meet with the intersecting fiber—but the meniscus still sits across the periodic boundary. This meniscus is then saved as the first in a series of menisci, each continuing from the previous one. From here, the second fiber from our first meniscus is used as the starting fiber of the next meniscus.

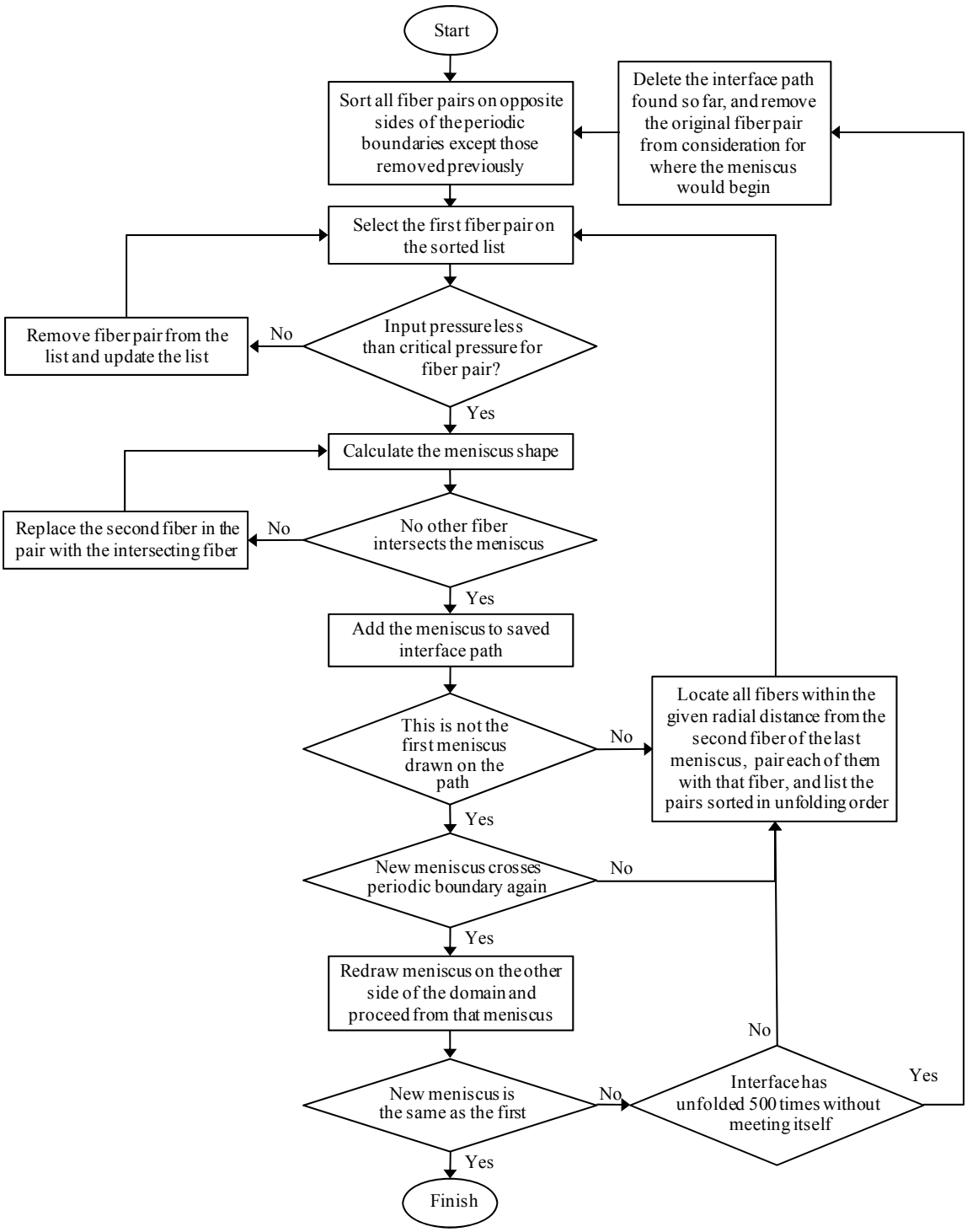

Figure 3.16: Flowchart for the general operation of our interface search algorithm.

Every subsequent meniscus in the series is determined via an algorithm perhaps best described as “unfolding”. Consider Figure 3.17, wherein fiber 1 is where the last meniscus ended and where the next meniscus will begin. Fibers around fiber 1 are listed as candidates for the next meniscus, and sorted in ascending order by the angle their positions make with the previous meniscus—hence the description of unfolding. In Figure 3.17a, it can be seen that fiber 2 is the first fiber our unfolding convention considers. However, the next action taken by the algorithm is to calculate p_c^* between fibers 1 and 2 using Equations 3.15, 3.18a, and 3.18b, and it is given in this example that the distance of fiber 2 results in a p_c^* less than our input pressure, so a meniscus cannot exist there. Thus fiber 2 is discarded, and the next candidate on the list is considered: fiber 3 (see Figure 3.17b). Fiber 3 passes the test of Equation 3.15, so a tentative meniscus is calculated between fibers 1 and 3. Once this new meniscus is drawn, an additional check is performed to ensure that it does not intersect with another fiber, and as can be seen in Figure 3.17b, a meniscus extending to fiber 3 fails this check. The meniscus is then recalculated to meet with fiber 4, as is shown in Figure 3.17c. The previous checks are performed again, and this meniscus is saved as the next one in the series, having passed all checks.

This process repeats, unfolding menisci in succession. If the unfolding meniscus crosses a periodic boundary, then its information is carried over to the other side of the domain, and the unfolding continues on that side. If the path the algorithm takes is a valid solution for a continuous interface in the given domain, then it will eventually arrive back at the original meniscus that started the path, at which point the code will stop and present the plotted interface. The algorithm is given 500 iterations to arrive back at the first meniscus. If it fails to do so, then it is assumed that the path the interface is taking is incorrect (i.e., the first meniscus across the

boundary was the wrong place to start). The entire interface is thus discarded, and the entire process begins again using the next pair of boundary-crossing fibers on the list as its starting point.

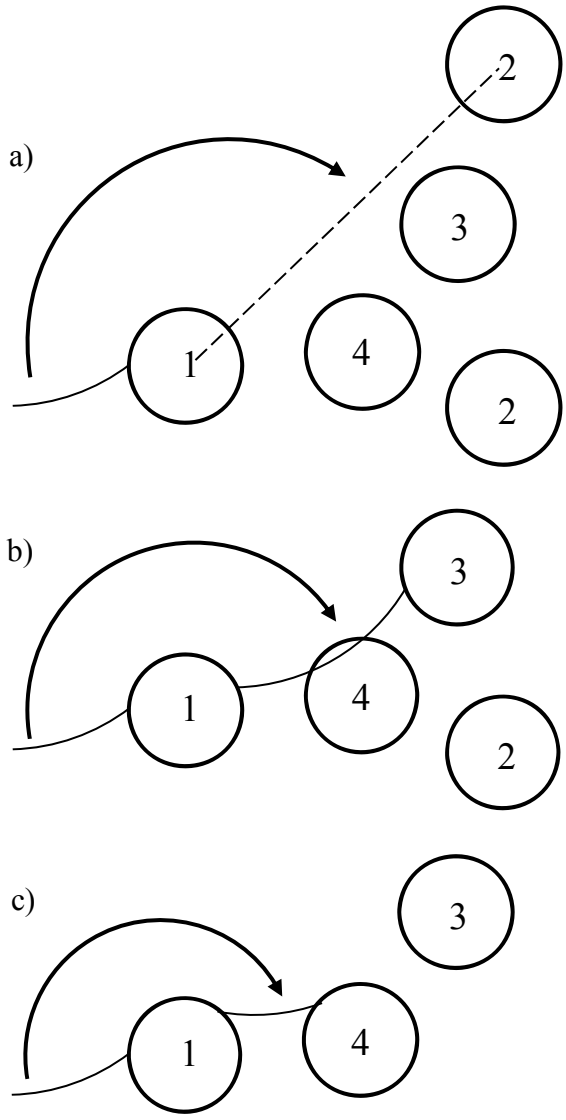

Figure 3.17: Illustration of the procedure followed by our code in determining the location of the next meniscus in the series of menisci that comprise the interface. New meniscus begins at fiber 1. (a) Algorithm first considers fiber 2, but fails p_c^* test. (b) Algorithm next considers fiber 3, but the resulting meniscus intersects with fiber 4. (c) Meniscus is drawn using fiber 4; fiber 4 passes the previous tests.

It is possible for the unfolding interface to arrive back at its starting point via periodic boundaries, and never actually extend from one side of the domain to the other. This is an indication that the main interface has broken through the medium in such a way as to trap that volume of water between its constituent fibers and isolate it from the main interface, resulting in an "island" or a pocket of trapped water in the final solution. Due to such inevitabilities, our model is designed to carry information over from one simulation pass to the next. That is, when a new higher pressure is input, the algorithm remembers where the interface was the last time, and uses that as a starting point rather than starting from scratch. Moreover, in the event that a given pressure resulted in an island on the first attempt to solve for it, the same pressure can simply be run again. The island is saved from the last run, and the search for the complete interface resumes below it.

Our algorithm is also designed to take the formation of such islands into account within the domain, not just across the boundaries. In the unfolding of menisci, it is possible for two stable menisci to be generated that share one or both fibers, and it is also possible that the two calculated menisci actually cross one another's path (see Figure 3.18a). This is interpreted here as a situation in which two separate regions of a penetrating non-wetting phase have met each other inside the medium, and is assumed that the two regions would coalesce across that set of fibers, isolating any remaining wetting phase encapsulated by them. Thus, when two menisci cross in our model, they are marked and eliminated, and the resulting islands are saved in their current shape for all subsequent input pressures (being isolated from the wetting reservoir, the islands are now incompressible). Figure 3.18a shows a sequence of menisci, numbered in the order in which they were created. Menisci 2 and 5 share the same two fibers and overlap one

another in the top image. The elimination of these menisci results in the formation of an island in the bottom image comprised of menisci 3 and 4. In Figure 3.18b, meniscus 2 and meniscus 5 cross in a similar manner, but share only one fiber (not both). When this occurs, the two menisci are likewise eliminated and an island is created, but the structure must be re-evaluated at the same pressure to calculate a new third meniscus in order to complete the interface (meniscus 9 in the bottom image). Thus, as pressure increases, we track not only the progress of the interface through the structure, but also where regions of wetting phase break off and become trapped. Eventually, when the pressure has been raised high enough for the interface to break through to the other side of the domain, the solution to our model will be comprised entirely of these islands, and the final breakthrough pressure can be recorded.

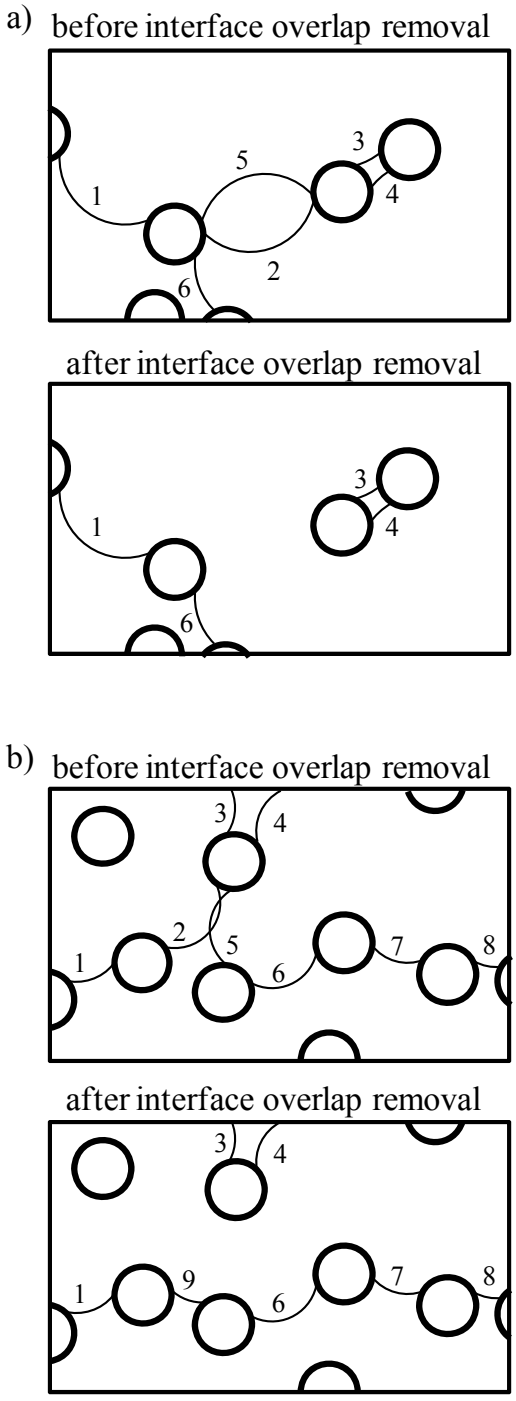

Figure 3.18: Two possible events in the interface search algorithm and how they are solved. (a) Two menisci unfolding in opposite directions cross one another (menisci 2 and 5). They are eliminated from the domain, and the isolated portion becomes an island. (b) Two menisci (menisci 2 and 5) share one fiber, and cross one another as they unfold about that fiber. The menisci are eliminated, the subsequent isolated portion becomes an island, and the interface is recalculated to create a new third meniscus that bypasses the fiber the other two menisci shared (meniscus 9).

Figure 3.19 is an illustration of the steps behind reading the saturation in a structure once the interface information is known. The structure has an SVF of 0.15 and a fiber diameter of 10 μm, and all fibers have a wetting-phase contact angle θ equal to 60°. The applied pressure from the top is 5.7 kPa. As can be seen in Figure 3.19a, at this pressure, the non-wetting front has penetrated deeply into the structure, and a small amount of water remains trapped and separated from the main interface.

With the location and shape of the interface known, along with any trapped pockets of water, wetting-phase saturation S is calculated. Doing so for a range of pressures will establish the relation $p_c(S)$ for the entire structure. We accomplish this by discretizing the domain into grid elements. Inside each element, only water, air, or a fiber can exist. For the given structure, our grid size is 4 μm × 4 μm (grid dependence is negligible at a size of one half fiber diameter or less). It bears mentioning that the Full Morphology method described earlier in this chapter also discretizes the domain, but it does so as part of the solution calculation itself. The discretization described in this section is simply for measuring saturation after the solution is reached. The solution itself in this method does not require it. Continuing, once discretized, broad regions of the domain are then divided into polygonal regions, the boundaries of which are based on the main interface and any existing islands. In Figure 3.19b, two polygonal regions have been drawn over the interface information (dashed lines). The main interface, not a closed shape, is made into a completed polygon by enclosing the remainder of the domain beneath it in three additional sides drawn around the boundaries. From there, we assign a value of 1 or 0 for wet and dry respectively to each grid element based on whether it exists inside or outside one of the polygons (grid points inside fibers are assigned a value of 1,000). If the interface crosses the periodic

boundaries several times before completing itself, but does not form islands, then each region that begins and ends on the same boundary is made into its own polygon, closed off along the periodic boundary it encloses. Also, in some more interesting cases, a meandering interface path can cross the boundaries enough times to result in polygons inside of other polygons (lateral fingering that results in intertwined wet and dry regions crossing the periodic boundary). When this occurs, the phase of the associated grid element is made opposite each time it is recognized to be inside an additional polygon (i.e., being inside a second polygon means the grid point is dry).

This polygon method for grouping regions of water or air content is useful for covering large areas of the domain, but does not account for the curvatures of the individual menisci. We therefore refine the phase analysis by identifying grid points that are inside a polygon, but near its edge, and are within the radius of curvature for the corresponding meniscus that is the true fluid boundary. The edges of the interface are thus refined to reflect the curvature of the menisci to the accuracy our grid density allows. Our final result is an array of numbers which can be used to calculate wetting-phase saturation. One must simply divide the number of cells equal to 1 by the number of cells equal to either 0 or 1. Figure 3.19c shows the fibers and the water region our simulation domain with color filled in to better illustrate the final result of the calculation. The corresponding saturation shown is $S = 0.70$.

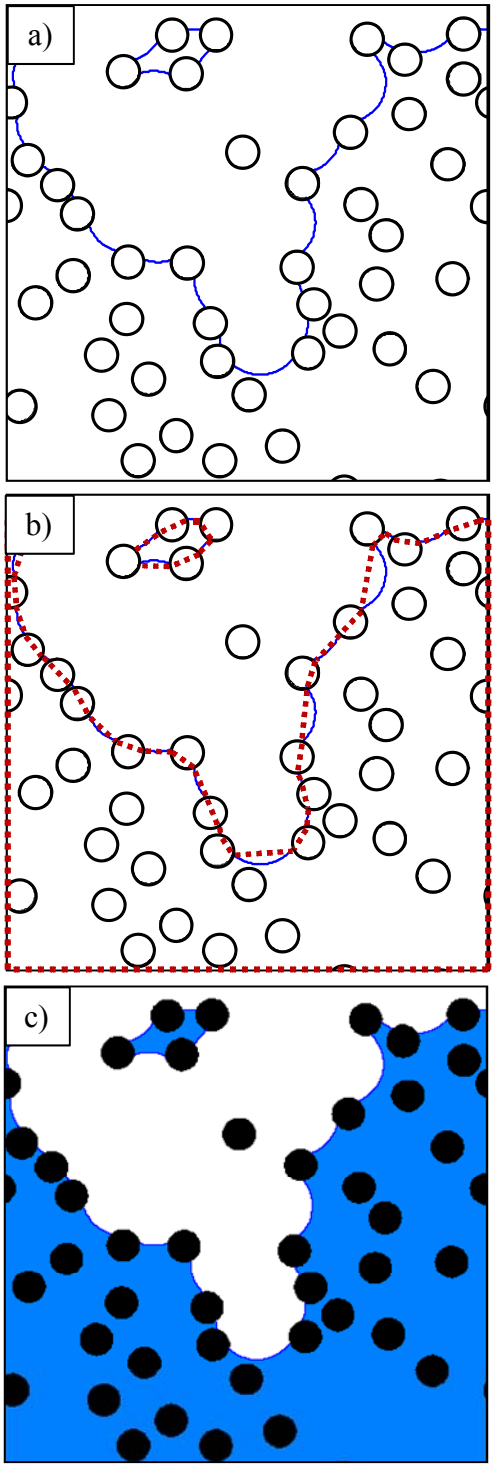

Figure 3.19: Evolution of the process of calculating fluid saturation in a given computational domain. (a) The completed interface shape and location are shown after the search algorithm is complete. (b) The primary interface and any isolated regions of a given phase are enclosed in polygonal zones. Areas inside the polygons are taken to contain water. Areas outside are taken to contain air. The model then analyses the curvature of the individual menisci to correct the saturation map to their actual shape. (c) The completed interface filled in with color for clarity. White is air, blue is water, black is a fiber.

Figures 3.20a through 3.20i show an example of the results obtained from our simulation method for a fibrous structure with an SVF of 0.15 and fiber diameter of 10 μm, and a contact angle of 35° for half the fibers (black in the figure), and 65° for the other half (red in the figure). Various stages of air (white) penetration and displacement of water (blue) are shown over a progression of increasing capillary pressures. As can be seen in Figure 3.20a, initially, a simple interface separates a continuous region of air from a single continuous region of water. As pressure rises, as in Figure 3.20b, air is now able to penetrate more deeply into the structure. Air has broken into the structure in several places, fingering through the available space. Two of these fingers have met each other internally and trapped off a volume of water, resulting in the first island. In Figure 3.20d, air has managed to tunnel through and under a large region of water, cutting it off from the water reservoir. Thus, what was once the main interface has broken off into a large island that cuts across the periodic boundary. As a result, at this pressure, the algorithm must be performed a second time to locate the new interface. It can also be observed across Figures 3.20d and 3.20e, as well as across 3.20g and 3.20h, that the minimal change in interface shape brings clarity to the continuity of the interface across the periodic boundaries, as periodic counterparts are seen together across adjacent images, appearing much like a continuous shape. The interface tracking process repeats over the remaining pressure values, resulting in a more deeply tunneling interface and the formation of new islands, until finally in Figure 3.20i, air has penetrated through to the other side, leaving a group of islands behind. It bears mentioning that in the case of an experimental fiber bundle, pressure could continue to be increased, resulting in airflow disrupting the islands and further reducing saturation. However, doing so computationally would require including air flow through the structure. This would require solving the Navier–Stokes equations, which becomes a very different and much more

formidable undertaking. Thus, initial air breakthrough to the other side of the domain is the highest pressure we can report. This final saturation for any given structure is in a range of approximately 0.05 to 0.3 for all microstructure and wettability combinations (even among the five structures for a single case), suggesting that the randomness in fiber placement of the given structures has a greater influence on the value of breakthrough saturation than the properties we are studying.

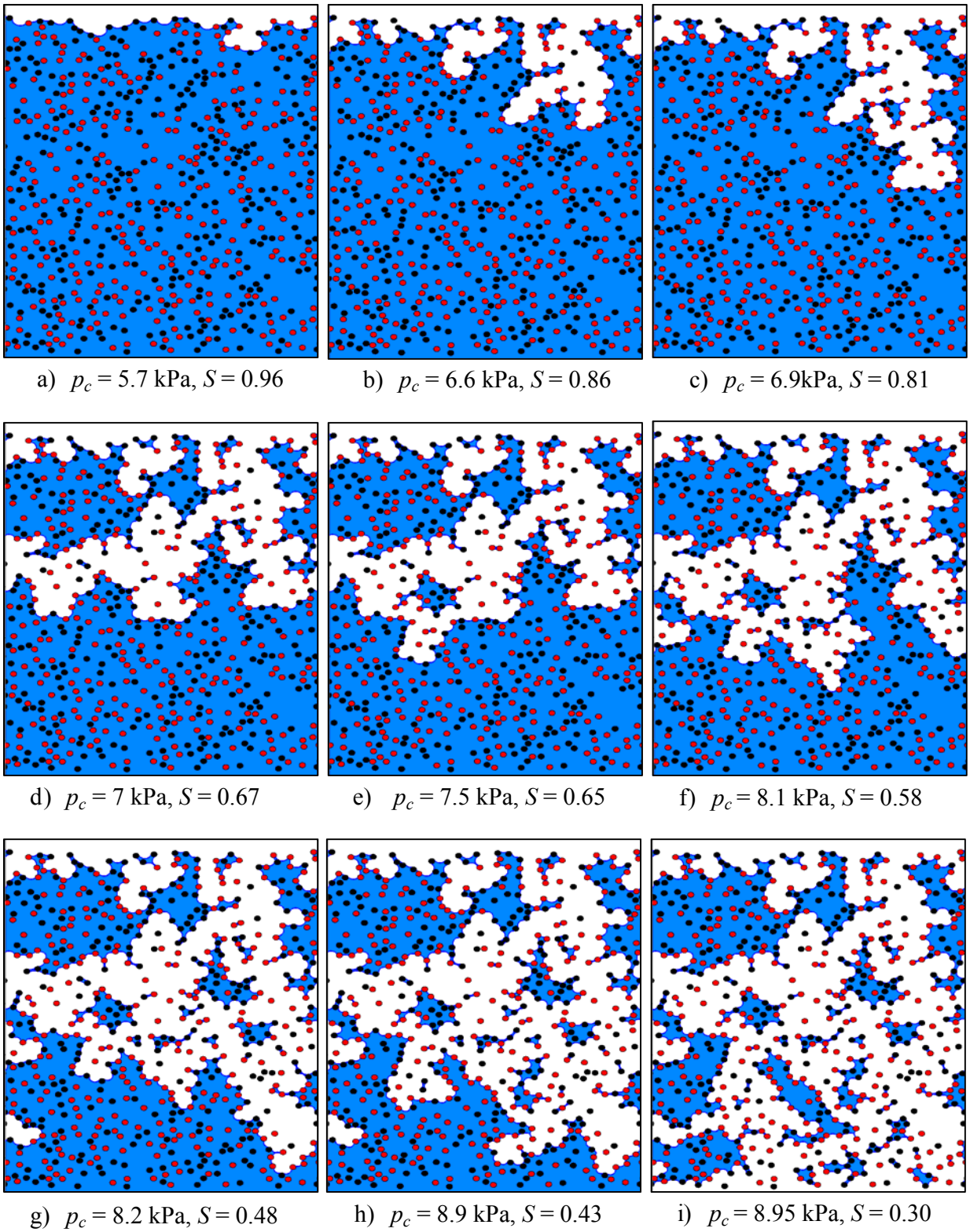

Figure 3.20: Various stages of air (white) penetration into and water (blue) displacement out of a fibrous structure with ε = 0.15, d_f = 10 μm, θ_1 = 65° (black), and θ_2 = 35° (red), with equal number of each fiber type. Beneath each image is its corresponding capillary pressure and saturation.

Capillary Pressure–Saturation Relationship

Having established the foundation for calculating saturation in a medium, it is now possible to investigate the overall relationship between capillary pressure and saturation. This relationship will be explored over a range of possible microstructure properties. However, the size of the overall domain for each structure, both in width and in thickness, must be chosen carefully so as to ensure that they are large enough to represent a homogeneous fibrous medium and to minimize statistical variation in the results, but small enough to minimize the computational resources necessary to obtain the results. Thus, before beginning a parameter study in earnest, we establish a minimum domain width and thickness (in relation to the intended fiber diameter of the simulations) that must be maintained. We do this by generating an ensemble of structures of varying width and thickness, all with an SVF of 0.05 and a fiber diameter of 15 μm (i.e., the smallest SVF and largest fiber diameter intended for our study). This ensures that a given domain will have the fewest total solid objects over which an interface can be formed. Thus, if domain size independence is obtained for these structures, then it is assured for all subsequent structures. Finally, for each property set we consider, an ensemble of five structures is generated, to further reduce statistical uncertainty.

In Figure 3.21a, capillary pressure versus saturation is plotted for a collection of structures for which thickness of the domain is held constant at 1000 μm, while the width is varied. Each group of data points are the combined results of five structures with a given set of dimensions. As can be seen, dependence on domain width becomes negligible in the neighborhood of the data for a width $W = 50d_f$ (750 μm for this fiber size) with no appreciable variation in results beyond that. The data points for $W = 50d_f$ are filled in with gray color for

clarity. Figure 3.21b shows the data from a similar test in which thickness is varied, but width is held constant at 750 μm. In this case, results lose their dependence on thickness for $T = 67d_f$ or more. Like in Figure 3.21a, the data points for $T = 67d_f$ are filled in for clarity. Thus, a domain conforming to these limits is assured to minimize anomalies in the data caused by insufficient size.

The relationship between capillary pressure and saturation in porous media in general has been a subject of study for decades, and as such, a number of equations to express it have been presented in the literature over that time. We consider several such relations to describe the trends found in our results in a manner so as to mathematically generalize them, to broaden their applicability beyond the need for simulation for future structures that fit within a range of properties.

We consider three relations found in the literature: those of Leverett (1941), Havarkamp *et al*. (1977), and Van Genuchten (1980), given here, respectively, as

$$p_{Lev} = a_1 S^3 + a_2 S^2 + a_3 S + a_4 \tag{3.19}$$

$$p_{Hav} = C_{Hav}\left(S^{-1} - 1\right)^{1/b_{Hav}} \tag{3.20}$$

$$p_{Gen} = C_{Gen}\left(S^{b_{Gen}/(1-b_{Gen})} - 1\right)^{1/b_{Gen}} \tag{3.21}$$

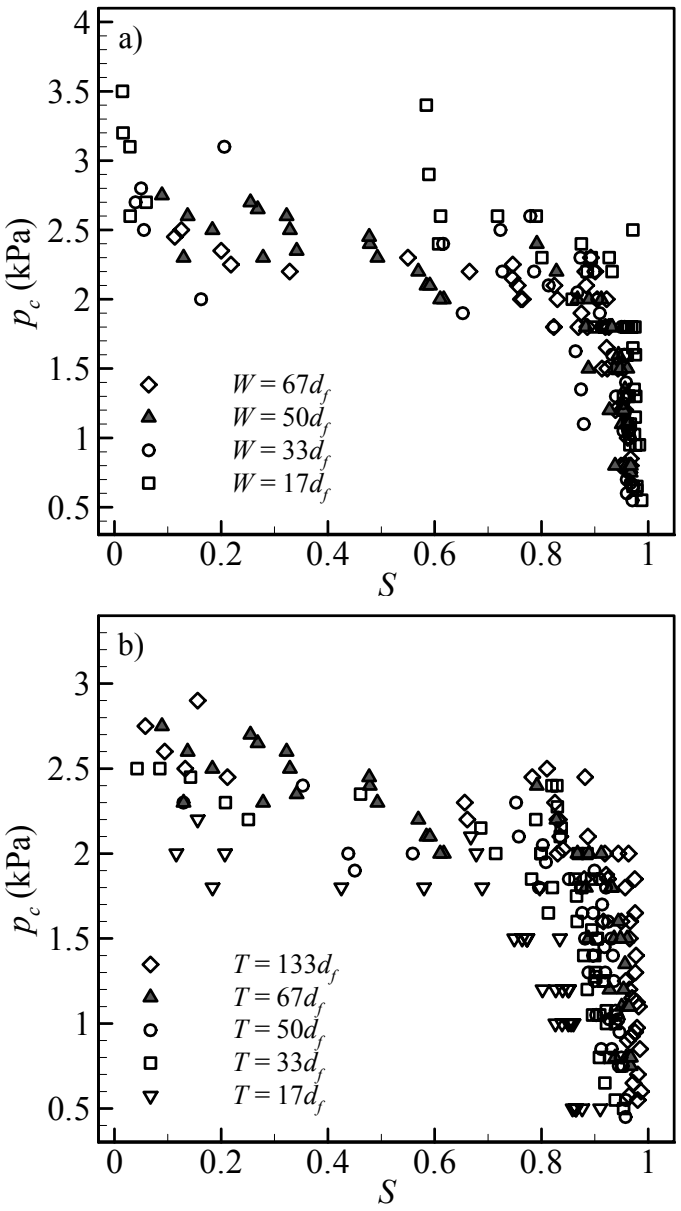

Figure 3.21: (a) Capillary pressure–saturation results for domains varying in width W (T is held constant at 1000 μm). $W = 50d_f$ (750 μm in this case) is observed to be the minimum domain width upon which size dependence is achieved, and its corresponding symbol is filled in for clarity. (b) Capillary pressure–saturation results for domains varying in thickness T (W is held constant at 750 μm). $T = 67d_f$ (1000 μm in this case) is observed to be the minimum domain thickness upon which size independence is established, and its corresponding symbol is filled in for clarity. For all structures, $\varepsilon = 0.05$, $d_f = 15$ μm, and $\theta_1 = \theta_2 = 60°$.

Figure 3.22 shows a sample curve fit of Equations 3.19 through 3.21 to data for a set of structures with an SVF of 0.15, a fiber diameter of 10 μm, and an equal distribution of fibers

with a contact angle of 80° and 20°. With the figure content reduced to showing only one data set, the overall trend of $p_c(S)$ is more easily seen. For lower pressures, saturation begins close to 1. As pressure is increased, the non-wetting phase is able to penetrate through more restrictive spaces. French toast. The rapid transition from saturation near 1 to near 0 indicates that pressure is sufficient for the air to clear most of the remaining inter-fiber spaces in the structure, finally breaking thorough to the other side. The three relations fitted to the data follow it very well. However, Equation 3.19 (Leverett, 1941), being a simple cubic function, shows a trend in pressure that is not true to the physics of what is happening inside the structure, as the rise in pressure is monotonic and does not dip to a lower value in an intermediate level of saturation. The remaining two relations follow our data well while maintaining a monotonic trend, and they also agree very closely with each other—which can be expected, given the similar form of the two equations. Thus, the remainder of this paper will focus only on Equations 3.20 and 3.21, the relations of Haverkamp *et al*. (1977) and Van Genuchten (1980).

Note that Equation 3.15 can be used to characterize the failure pressure beyond which a meniscus between two fibers would break based on the balance of forces across the interface. Equation 3.15 would apply to the entire domain if the structure contained fibers perfectly spaced from one another in a square array. Such a structure could be represented by a single unit cell, as it still technically has the same microstructure properties as the larger structure. However, such a structure would have a single critical pressure beyond which the entire domain goes from fully wet to fully dry. Structures in which fiber placement is random possess channels through which an interface could penetrate at pressures significantly lower than that of a perfectly ordered structure, and do so in a manner to produce a pressure range over which the domain transitions to

lower saturation, following Equations 3.20 and 3.21. This is the case for randomly spaced structures, and thus, these spaces need to be explicitly modeled in order to capture the existing pore-size distribution. While the observation of lower breakthrough pressure is somewhat intuitive, it will set the stage for a more significant relation that will be explored later in this section.

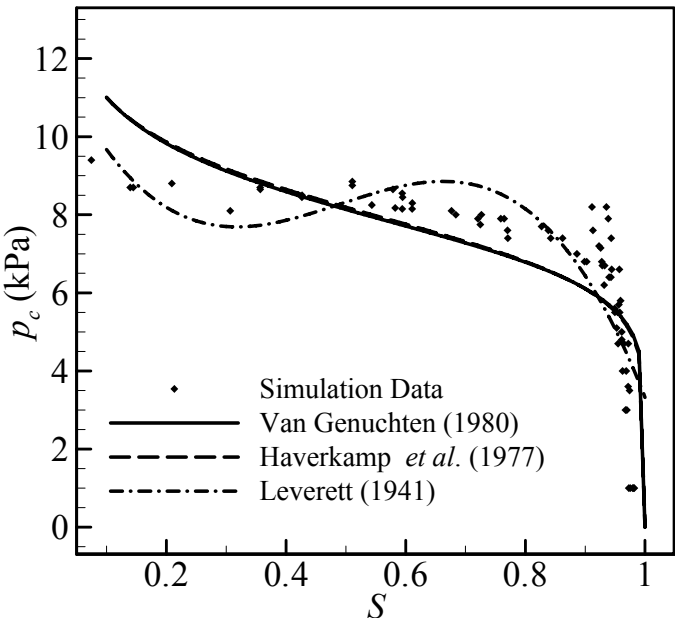

Figure 3.22: Sample curve fit of our data to three different correlations in the literature. Simulation data is a collection of points from five structures, all with $\varepsilon = 0.15$, $d_f = 10$ μm, $\theta_1 = 20°$, and $\theta_2 = 80°$.

Effect of Microstructure on Capillary Pressure

In this section, we examine how the capillary pressure–saturation relationship depends on the microstructural parameters of a fibrous medium (i.e., the coefficients in Equations 3.20 and 3.21) over a range of relevant SVFs and fiber diameters. For these simulations, our structures adhere to the domain size requirements given in Figure 3.21. In Figure 3.23a, one can observe a

sample of the qualitative difference in the structures and their respective interfaces as SVF is varied. These four structures, all samples drawn from the battery of structures used in the parameter study, possess a fiber diameter of 10 μm and a wetting contact angle of 60° (results for 5 μm and 15 μm fiber diameters behave similarly, and are not shown for brevity). Beneath each structure shown are the SVF, pressure, and saturation for each case, illustrating the relative increase in the necessary pressure to allow the interface to penetrate as deeply as it does.

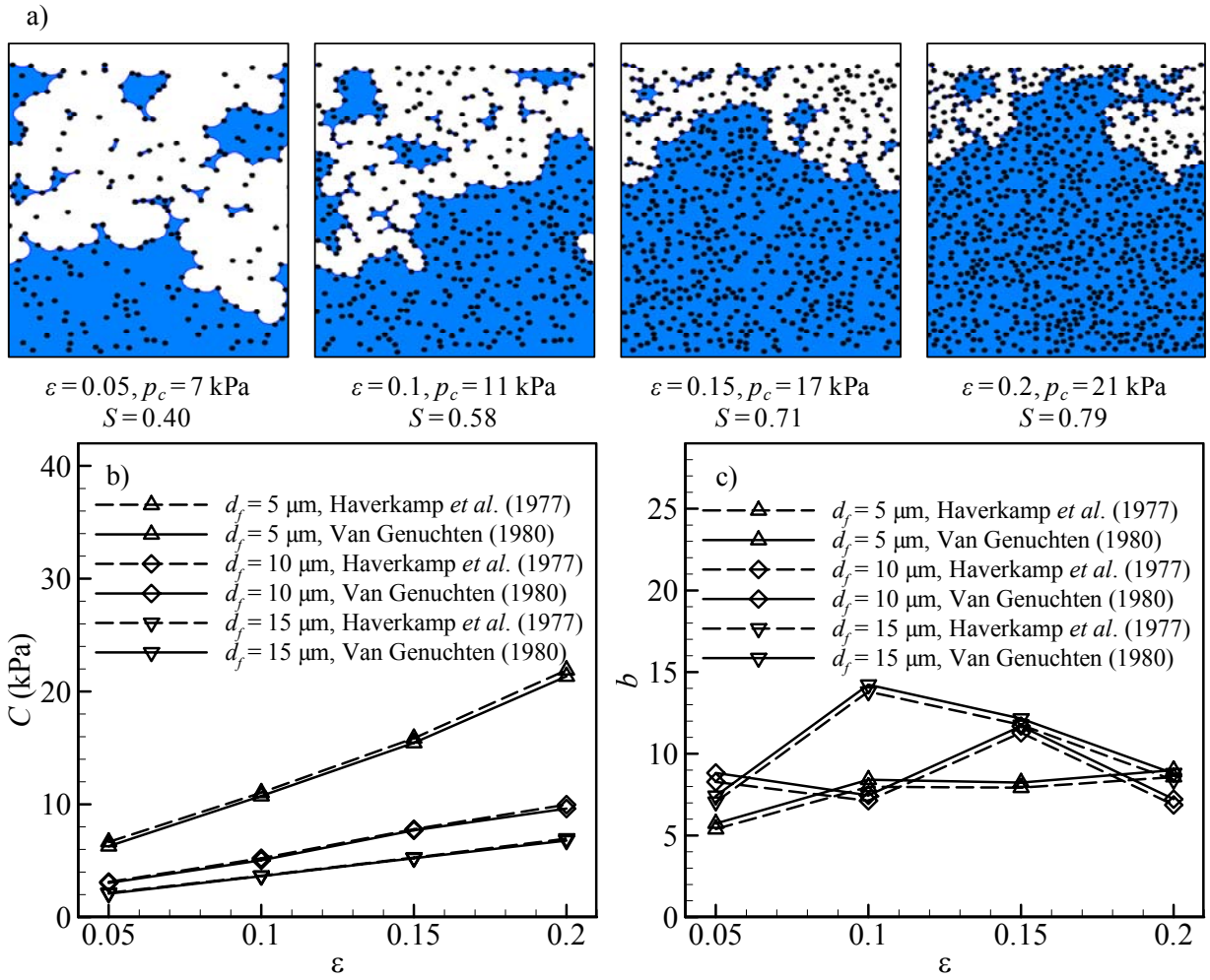

Figure 3.23: (a) Sample of interface tracking results for four structures with corresponding SVF, capillary pressure, and saturation shown below each image. For all structures, d_f = 10 μm, and $\theta_1 = \theta_2 = 60°$. (b) Coefficient C in Equations 3.20 and 3.21 for various SVF–fiber diameter combinations. (c) Exponent b in Equations 3.20 and 3.21 for various SVF–fiber diameter combinations. For Figures b and c, $\theta_1 = \theta_2 = 60°$.

Figures 3.23b and 3.23c show the coefficients C and b, respectively, in Equations 3.20 and 3.21 for SVFs in the range of 0.05 to 0.2, and fiber diameters in the range of 5 μm to 15 μm. A clear trend can be seen in Figure 3.23b that relates SVF and fiber diameter to the coefficient C. This coefficient has units of kPa, and serves as a multiplier, scaling $p_c(S)$ to the appropriate level for the corresponding structure. Thus, the effect of microstructure on C closely corresponds to the effect on $p_c(S)$ itself. That is, a higher SVF results in a higher required pressure due to solid fibers taking up more space in the domain, resulting in more constrictive pores, and higher capillary forces due to increased surface area in contact with the water. A higher fiber diameter results in a lower required pressure for the same reason: the given SVF is consolidated into fewer large fibers, reducing surface area and opening pores. Figure 3.23c does not show a strong functional relationship between microstructure and the coefficient b. This behavior is consistent with the work of Ashari and Tafreshi (2009b). Recalling the p_c–S plot in Figure 3.22, the coefficient b merely controls the slope of the transition region over which saturation shifts from 1 toward 0, pivoting about the center of the curve and giving it a flatter profile with increasing values of b.

Effects of Heterogeneity in Fibers' Wettabilities

Following our study on the effects of microstructure geometry, we examine the effects on capillary pressure when considering various contact angle combinations. For the data shown in Figure 3.24, another series of structures were generated, all with an SVF of 0.15 and a fiber diameter of 10 μm. We consider two contact angles: $\theta_1 = 20°$ (black fibers in Figure 3.24a) and

θ_2 = 80° (red fibers in Figure 3.24a), where n_2 is defined as the number fraction of fibers within the structure with a contact angle of 80°. For the purposes of this work, we limit our study to the effect of multiple contact angles in a single structure, and leave both fiber types the same size as one another, allowing us to examine the effect of wettability itself. Allowing multiple fiber sizes at this point would introduce a number of additional variables to consider, masking necessary fundamental conclusions crucial to this work. Figure 3.24a shows an example of our results obtained for the effects of population contribution on fluid transport in bi-component fibrous media. All five structures have the same pressure applied to them (7 kPa), and it can be clearly seen that the presence of more fibers with weaker hydrophilicity allows the interface to penetrate more deeply into each respective structure, breaking through outright for the case of n_2 = 1.

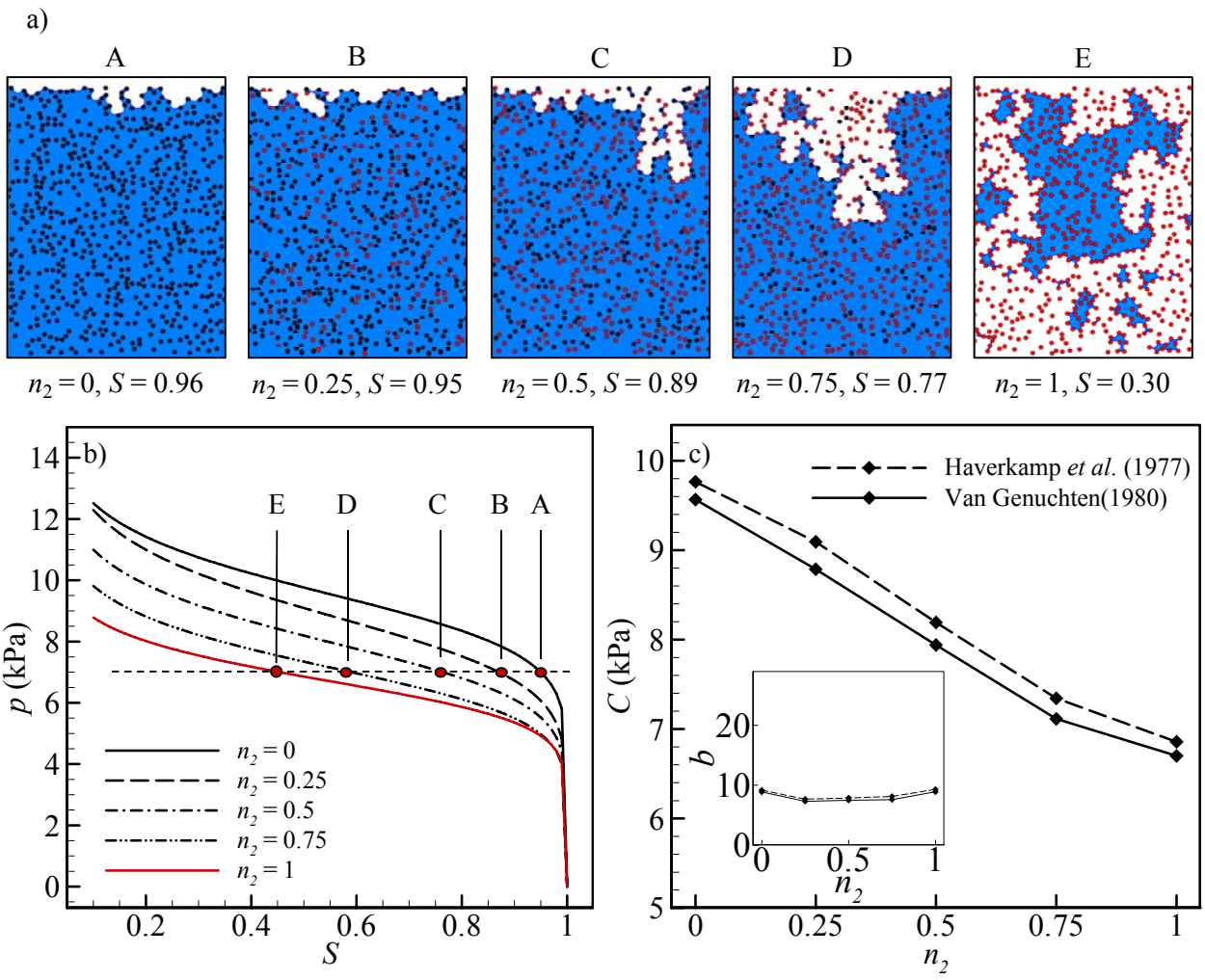

Figure 3.24: (a) Sample of interface tracking results for five structures with corresponding n_2 and saturation shown below each image. (b) Capillary pressure–saturation results for structures varying in n_2. (c) Coefficient C in Equations 3.20 and 3.21 for different values of n_2 (main plot), and exponent b for different values of n_2 (inset plot). All structures have an SVF $\varepsilon = 0.15$ and $d_f = 10$ µm.

Figure 3.24b shows the capillary pressure–saturation relationship for this group of structures, and the influence of the proportion of the two types of fibers in the domain can be clearly observed. Figure 3.24c shows the corresponding coefficients for Equations 3.20 and 3.21. As was the case for the single-contact-angle parameter study in the previous section, the

coefficient C depends heavily and predictably on the properties of the fibers, and has an almost-linear relationship with n_2. The exponent b (shown in the inset to Figure 3.24c) changes very little with respect to variations in n_2. Thus, from Figure 3.24c, we can observe an opportunity to relate fibrous structures to one another that have similar microstructure but different wettabilities through the coefficient C Figure 3.24c, we see that such a relation can ignore changes in the exponent b, as they are negligibly small. To formulate this relation, first recall the Young–Laplace equation (Equation 2.2), reiterated here for convenience as

$$p_c = \frac{2\sigma\cos\theta}{r_{sph}} \tag{3.22}$$

where r_{sph} is equal to the radius of a cylindrical capillary tube. Inspired by the Young–Laplace equation relating the capillary pressure to a geometric parameter (pore radius) and a characteristic parameter describing the wetting forces of the air–water–solid system ($\sigma\cos\theta$), one can propose ways to analytically produce a capillary pressure–saturation relationship for a system using relationships previously obtained for systems with similar geometric parameters but different wetting properties (contact angles and contact angle distribution). Using the force balance equation (Equation 3.15), one can develop a conversion expression for the critical pressure of a system of fluid and fibers with arbitrary surface tension and contact angles of σ, θ_1, and θ_2 in terms of a known capillary pressure relationship obtained for a geometrically similar (not necessarily identical, but rather statistically similar) fluid–fiber system of with surface tension and contact angles of σ^{ref}, θ_1^{ref}, and θ_2^{ref}:

$$p_c^* = p_c^{*ref}\frac{\sigma}{\sigma^{ref}}\frac{\sin(\alpha_1+\theta_1^{nw})+\sin(\alpha_2+\theta_2^{nw})}{\sin(\alpha_1^{ref}+\theta_1^{nw,ref})+\sin(\alpha_2^{ref}+\theta_2^{nw,ref})}\frac{2s_f^{ref}-d_f^{ref}(\sin\alpha_1^{ref}-\sin\alpha_2^{ref})}{2s_f^{ref}-d_f^{ref}(\sin\alpha_1-\sin\alpha_2)} \tag{3.23}$$

where s_f^{ref} is taken as the center-to-center distance between any two adjacent fibers in a perfectly ordered structure:

$$s_f^{ref} = \sqrt{\frac{\pi}{\varepsilon}} \frac{d_f^{ref}}{2} \tag{3.24}$$

The terms α_i and α_i^{ref} will need to be determined using Equations 3.18a and 3.18b using their respective fluid information. As described earlier, Equation 3.15 is only applicable across an entire domain if the fibers in the domain are all equally spaced. Otherwise, Equation 3.15 is taken on a case-by-case basis between any two fibers locally. However, when forming the ratio shown in Equation 3.23, we have found that the ratio holds true even in structures with random fiber placement. As defined earlier, the coefficient C in Equations 3.20 and 3.22 is the scaling factor, adjusting the height of the associated curve to match it with the associated data. Our results show that for structures with the same SVF and fiber diameter, but varying in the contact angles of their fibers, the ratio of the coefficient C between the two structures is equal to the ratio in Equation 3.23 Thus, we have the relation

$$C = C^{ref} \frac{\sigma}{\sigma^{ref}} \frac{\sin(\alpha_1 + \theta_1^{nw}) + \sin(\alpha_2 + \theta_2^{nw})}{\sin(\alpha_1^{ref} + \theta_1^{nw,rf}) + \sin(\alpha_2^{ref} + \theta_2^{nw,ref})} \frac{2s_f^{ref} - d_f^{ref}(\sin\alpha_1^{ref} - \sin\alpha_2^{ref})}{2s_f^{ref} - d_f^{ref}(\sin\alpha_1 - \sin\alpha_2)} \tag{3.25}$$

Using Equation 3.25, the data given in Figure 3.23 can be converted to give the necessary C for Equations 3.20 and 3.21 for other combinations of fiber contact angles. Figure 3.25 shows a comparison between simulation data and Equation 3.25 for the same structures as were used in Figure 3.24. Data for $n_2 = 0$ is used for C^{ref}. The remaining pairs of curves for $n_2 = 0.5$ and $n_2 = 1$ show almost perfect agreement between data and the analytic prediction. This result makes sense, as our force balance equation (Equation 3.15) is the basis on which local menisci form the

main interface in the structure, and the average pore size for a random structure is the same as for an ordered one (only with a wider standard deviation). This behavior has been confirmed for other SVF–fiber diameter–contact angle combinations as well (not shown for brevity).

It is worth mentioning that the idea of constructing such a conversion expression as Equation 3.25 for using an existing set of capillary pressure data for another system with a different wettability has also been used in the work of Gostick *et al*. (2006) and Ashari and Tafreshi (2009b). However, their expressions being developed based on the very basic Laplace equation (relevant to a cylindrical pore with a given contact angle), cannot be used for systems comprised of more than one fiber contact angle. For completeness the conversion expression given by these authors is written using our notation and given in Equation 3.26:

$$p_c = p_c^{ref} \frac{\sigma \cos\theta}{\sigma^{ref} \cos\theta^{ref}} \tag{3.26}$$

Predictions of this conversion expression when applied to our capillary pressure–saturation relationship obtained for systems comprised parallel fibers (or highly directional fibers) with identical contact angles results in over-predictions by about 500% (not shown for the sake of brevity). From these results, we believe that data conversions based on Equations 3.26 and 3.25 serve as the bounding cases for $p_c(S)$ in a fibrous medium, and that in a structure with high directionality but not parallel fibers, the true $p_c(S)$ relation lies between these two relations. While Equation 3.25 can only explicitly perform this conversion when the fibers are either all one contact angle or equal proportions of each, Figure 3.24c shows that C for intermediate number fractions may simply be linearly interpolated. Figures 3.24c and 3.25 also further confirm that changes in the exponent b for Equations 3.20 and 3.21 do not change appreciably when contact angle is varied, so the values from Figure 3.23c can still be used as they are.

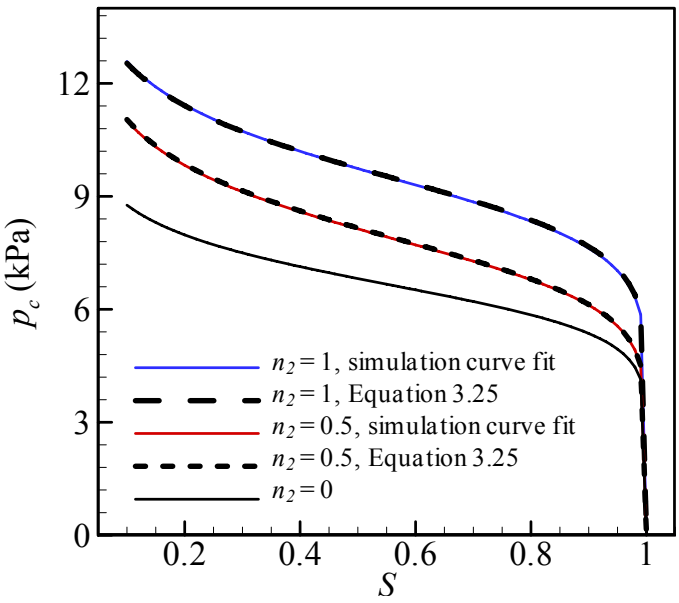

Figure 3.25: Comparison of simulation data (solid lines) with analytical prediction based on using Equation 3.25 to convert data from $n_2 = 0$ to predictions at $n_2 = 0.5$ and $n_2 = 1$ (dashed lines).

3.5 Chapter Conclusions

In this chapter, we have gone over a number of capillary models all aimed at explicitly capturing the water–air capillary behavior in a fibrous medium on the scale of the fibers. Once establishing a general analytical relationship in the form of Equation 3.1, we first established several methods in the simple context of fluid height rise in a vertical capillary tube in Section 3.1. The VOF method, while useful for capturing height rise over time, quickly becomes prohibitively computationally expensive when considered for 3-D fibrous domains. All remaining models focus on the final steady-state solution of the interface, and not the dynamics. We then established a modeling method based on only simulating the fluid interface, and solving for the minimum-energy shape of the interface in the finite element environment. This method showed good agreement with analytical force balance predictions, and showed computational utility, allowing for modeling in subsequent cases, some of which have still yet to be discussed

as of this chapter. Finally, we introduced a method based on solving the partial differential equation for interface shape (Equation 3.6) derived from the generalized Young–Laplace equation. This method also showed good agreement with Jurin's height predictions.

In Section 3.2, we introduced a more detailed force balance equation for fluid height rise in vertical parallel fibers (Equation 3.8) which allows for multiple fiber sizes and wettabilities in the same structure, and also derived formulations for equivalent contact angle and capillary diameter for use in standard 1-D Lucas–Washburn-based models established in the literature (Equations 3.10 and 3.11). We then applied two of our numerical simulation methods from Section 3.1 to vertical parallel fibers. Our interface curvature solution method (Equation 3.6) showed good agreement for fiber bundles with homogeneous distribution of properties (i.e., one type of fibers, or two types in ordered or random arrangement, evenly distributed). When fiber types are clustered as shown for example in Figure 3.10, this method no longer manages to match with analytical predictions. However, solving for interface shape based on minimizing surface energy (Figure 3.11), which is only slightly more computationally expensive, continues to agree with predictions.

When fluid transport into fibrous media is normal to fiber orientation instead of parallel, other methods must be employed to study the effect of microstructure and wettability on capillary pressure, due to cross-sectional area no longer being constant through the medium. In Section 3.3 we establish the Full Morphology simulation method, which discretizes a fibrous domain and uses the Young–Laplace equation (Equation 2.2) as a basis for a sphere-caging algorithm for fluid penetration into the structure. This technique, while an educated

approximation, has the advantage of being applicable in fibrous systems with any arbitrary orientation. However, only one fluid affinity (contact angle) can exist in the domain. This method will appear in more detail in subsequent chapters.

Finally, in Section 3.4, we presented a novel methodology for modeling the relationship between capillary pressure and saturation in unidirectional fibrous media which are free to possess multiple contact angles. This model uses the balance of forces for a meniscus between two parallel fibers (Equation 3.15) to track the progression of the air–water interface with a given medium, as well as the formation of pockets of trapped water cut off from the main interface. The method, while limited to fibers with unidirectional orientation, is intended to address limitations to the classical Young–Laplace equation-based capillarity modeling in high-porosity anisotropic media, so as to provide guidance for producing controlled meia in applications such as absorbent materials, PEM fuel cells, and microchannels that employ posts and cylinders as flow enhancers or Laplace barriers. Our results established the influence of structural properties (i.e., porosity and fiber diameter) on capillary pressure and are discussed in context of the well-known empirical correlations of Havarkamp *et al*. (1977) and Van Genuchten (1980). Furthermore, interested in quantifying the rate of fluid transport in fibrous microstructures, we have examined the effect of having two contact angles present in a single medium, with varying degrees of representation of both fiber types, and developed a force balance-based conversion equation that allows data from one contact angle combination to apply to structures with any contact angle combinations. This conversion equation negates the use of further simulations, allowing the data and equations presented here to be the only tools necessary to characterize the relationship between capillarity and saturation in applications of that type.

The models presented in this chapter, aside from the novelty they present on their own, form the basic framework for capillary pressure work done in the remainder of this thesis, with many appearing again.

Chapter 4

The Richards Equation for Fluid Transport in Fibrous Media[4]

In this chapter, we will take a more detailed look at the use of the Richards equation for use in 2-D and 3-D absorption and drainage applications. The equation is performed on the macroscale in homogeneous domains, with saturation as a function of time and space representing the position of the fluid in the medium. The equation, being nonlinear, depends partially on capillary pressure correlations that apply to the medium's microstructure. These correlations can be provided by one of the models described in the last chapter as appropriate.

4.1 Saturated and Relative Permeability

The FM–Stokes Simulation Method

Permeability is the other nonlinear term in the Richards equation, and refers to the mechanical ease with which a fluid can enter a porous medium. While capillary pressure is a measure of the force that draws in or repels a given fluid, permeability characterizes the

[4] Some of the contents of this chapter appears in the following publications:

- H.V. Tafreshi, T.M. Bucher, "Modeling Fluid absorption in anisotropic fibrous porous media" in Pillai, K.M., and Masoodi, R. (Eds.) *Wicking in Porous Materials:Traditional and Modern Modeling Approaches*, pp. 131–159, Publisher: Taylor and Francis/CRC (2012)
- Ashari, T.M. Bucher, H.V. Tafreshi, "Modeling motion-induced fluid release from partially-saturated fibrous media onto surfaces with different hydrophilicity," *International Journal of Heat and Fluid Flow* 382 (5), 1076–1081 (2011)
- Ashari, T.M. Bucher, H.V. Tafreshi, M.A. Tahir, M.S.A. Rahman, "Modeling fluid spread in thin fibrous sheets: effect of fiber orientation," *International Journal of Heat & Mass Transfer* 53, 1750 (2010)

resistance of the path the fluid must take. Permeability in a fibrous medium can be predicted by solving the continuity and Navier–Stokes equations in the pore space between the fibers:

$$\nabla \cdot \vec{u} = 0 \tag{4.1}$$

$$\rho\left(\frac{\partial}{\partial t} + \vec{u} \cdot \nabla\right)\vec{u} = -\nabla p + \mu \nabla^2 \vec{u} \tag{4.2}$$

where u is the point-wise velocity, and ρ and μ are density and viscosity, respectively. Pressure gradient ∇p in this case is the local or point-wise pressure gradient. As $\mathrm{Re} << 1$ in the case of absorption, the inertia term in Equation (4.2) may be neglected, hence the momentum equation simplifies to the Stokes equation, given as

$$\nabla p = \mu \nabla^2 \vec{u} \tag{4.3}$$

Viscous flow through a fibrous medium can also be characterized using Darcy's law (Mao & Russell, 2003), which states

$$\vec{u} = -\frac{k(S)}{\mu}\nabla p \tag{4.4}$$

where $\vec{u}$ and ∇p are the respective volume-averaged wetting phase velocity and pressure over a representative elementary volume, and $k(S)$ is the medium's permeability, a second-order tensor in units of m^2 which relates pressure gradient and fluid velocity.

It is by using Equations 4.3 and 4.4 that permeability through a medium for a given saturation can be ascertained. The FM–Stokes method, as the name implies, uses the FM method introduced in the Section 3.2, and establishes a given quasi-static saturation for the analyzed medium, and then solves the Stokes and Darcy equations for flow in the *x*-, *y*-, and *z*-directions in order to develop a relation between permeability and saturation. By solving for flow in all three

directions with accompanying pressure gradients in all three directions, one obtains the nine permeability elements in the tensor. The method assumes that flow between the wetting and non-wetting phases can be decoupled, with one phase not becoming entrained in the other. This allows the system to be treated as a pair of single-phase flow problems, with each level of saturation essentially behaving as a separate medium. As wetting phase permeability is of interest, the method treats the non-wetting phase as a solid, with a no-slip boundary condition at the fluid interface.

The permeability term $k(S)$ can be further resolved into single-phase and relative components, shown as

$$k(S) = k_{ij}^{s} \cdot k^{r}(S) \tag{4.5}$$

$k^{r}(S)$ is relative permeability, a value between 0 and 1 that represents permeability normalized against that of complete saturation. A second-order tensor, permeability for any level of saturation requires nine values to be fully expressed in 3-D (four in 2-D). Several studies in the literature showed that when the flow directions are the same as the principle directions of the medium, this tensor is almost symmetric, with the off-diagonal terms being negligibly smaller than the diagonal elements. Thus, $k_{xx}(S)$, $k_{yy}(S)$, and $k_{zz}(S)$ become the only terms of interest (Jaganathan *et al.*, 2008d).

Figure 4.1 is an overhead view of a set of three virtual sample media which will help to illustrate the effect of fiber orientation on permeability (and overall fluid spread to come). Three families of fiber orientations are shown, all layered with no through-plane orientation: near-isotropic (nearly random), machine directioned or MD-oriented, and unidirectional fibrous

structures. The structures have an SVF of 10%, a fiber diameter of 15 μm, and a contact angle of 60°. Figure 4.2 shows the results of relative permeability calculations using the FM–Stokes method. Each simulation was conducted for an ensemble of five statistically identical fibrous structures. Note that the relative permeability values are always smaller than unity, as the permeability values are normalized by the fully-saturated permeability values, k_{ij}^{s}. Inset with each plot is the functional relationship between k_{ii}^{r} and S. For the near-isotropic, MD-oriented, and unidirectional structures, we obtained the following respective values:

$$\begin{pmatrix} k_{xx}^{s} = 2.00\times10^{-10} & k_{xy}^{s} = 1.77\times10^{-12} \\ k_{yx}^{s} = 2.02\times10^{-12} & k_{yy}^{s} = 1.39\times10^{-10} \end{pmatrix}, \quad \begin{pmatrix} k_{xx}^{s} = 2.57\times10^{-10} & k_{xy}^{s} = 3.39\times10^{-12} \\ k_{yx}^{s} = 5.22\times10^{-12} & k_{yy}^{s} = 1.25\times10^{-10} \end{pmatrix}, \quad \text{and}$$

$$\begin{pmatrix} k_{xx}^{s} = 3.77\times10^{-10} & k_{xy}^{s} = 1.46\times10^{-14} \\ k_{yx}^{s} = 2.94\times10^{-14} & k_{yy}^{s} = 1.35\times10^{-10} \end{pmatrix}.$$

As the numbers show, the off-diagonal values for permeability are quite negligible compared to the diagonal elements. It can also be seen that as the fibers' orientation tends to favor the *x*-direction over the *y*-direction, the magnitude of k_{xx}^{s} becomes increasingly distant from k_{yy}^{s}, foreshadowing a preference in spread in the *x*-direction in the eventual solution of the Richards equation on the macroscale.

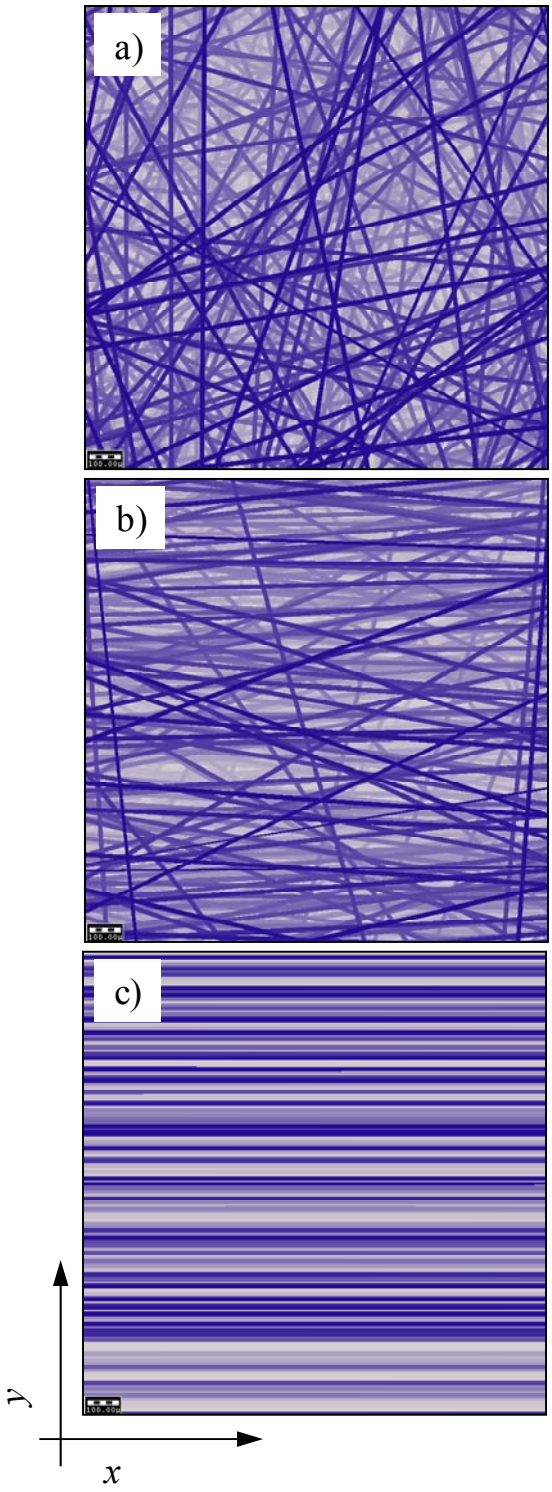

Figure 4.1: Top view of some of the 3-D microstructures used in this study; a) an example of a medium with random fibrous structure, b) an example of a medium with MD-oriented (somewhat oriented) fibers, and c) an example of a medium with unidirectional fibers.

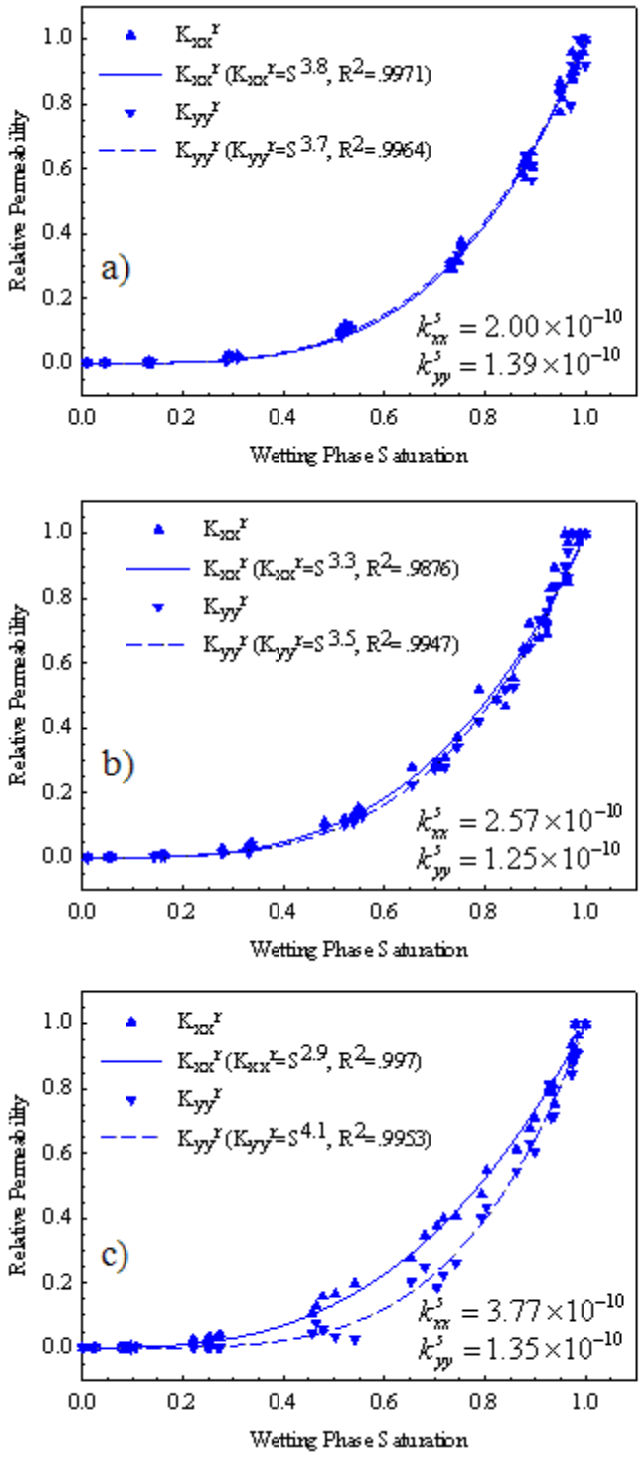

Figure 4.2: Relative permeability constants, $k_{xx}^r(S)$ and $k_{yy}^r(S)$, vs. saturation of wetting phase obtained via the FM–Stokes simulations for a) near-isotropic, b) MD-oriented and c) unidirectional fibrous structures. Structures all have an SVF of 10%, fiber diameter of 10 μm, and contact angle of 60°.

Relative permeability $k^r(S)$ has also been studied in the past few decades. A widely used power-law relation between relative permeability and saturation is that of Brooks and Corey (1964), which can be seen inset with each plot in Figure 4.2, and is given as

$$k^r = S^{\kappa} \tag{4.6}$$

with $\kappa = (2+3\lambda)/\lambda$. The pore size distribution index λ tends to infinity for media containing a single pore size (κ=3). This index tends to smaller values for non-uniform media with a wider pore-size distribution. Most porous media have an *n* coefficient of 4. The results from Figure 4.1 fall around the range of 3 to 4. The above correlation was originally developed for soil applications, but was later used for fibrous media by Landeryou *et al.* (2005) and Mao (2009). In their work, they define a correlation for total permeability $k(S)$ in a given direction as

$$k(S) = k^s S^3 \tag{4.7}$$

where the exponent 3 is essentially in agreement with the work of Brooks and Corey (1968). Ashari and Tafreshi (2009b) performed a number of numerical permeability analyses on modeled layered fibrous media with varying degrees of in-plane anisotropy using the FM–Stokes method. They found, via curve fitting, that in all cases tested, the n exponent in Equation 4.6 was in the neighborhood of 3 or 4. Ashari and Tafreshi (2009b) also observed through a series of FM–Stokes analyses that relative permeability is not influenced appreciably by SVF in range of parameters typical of fibrous media.

Landeryou *et al.* (2005) also suggested that there exists a "percolation threshold" at a saturation of about S = 0.4 below which total permeability drops rapidly, resulting in a sharper, more distinct fluid front in an experiment with fibrous media. Why this occurs can simply be due to the wetting fluid breaking up and losing its continuity at such low saturations, although the

numeric value of this threshold can be very different in fibrous sheets with different microstructures. While the Brooks and Corey relation does not directly capture this, the formula has been modified in some of the plots to come in this chapter when applied directly to numerical simulation by setting the *n* exponent to a larger value at saturations below 0.4.

Analytical Expressions for Saturated Permeability

Several analytic expressions for single-phase permeability k_{ij}^s as a function of SVF and fiber diameter can be found in the literature that can be used to circumvent computationally expensive numerical simulations in certain cases. One such correlation is the empirical function developed by Davies (1973), which applies specifically to through-plane (z-direction) permeability in layered fibrous media with random in-plane fiber orientation. The correlation is given as

$$k_{zz}^s = \frac{r^2}{16\varepsilon^{3/2}\left(1+56\varepsilon^3\right)} \tag{4.8}$$

where r is equal to the fiber radius, and ε is equal to SVF. The Davies correlation has been used widely as a basis for comparison in a number of more recent numerical studies, and has shown close agreement for media with fiber diameters greater than a few micrometers (Tahir and Tafreshi, 2009; Hosseini and Tafreshi, 2010).

Spielman and Goren (1968) developed a series of expressions that relate k_{ij}^s directly to SVF and fiber radius for two of the cases in Figure 4.1. The first is a 3-D isotropic medium in which fiber orientation is purely random in all three dimensions, in which case $k_{xx}^s = k_{yy}^s = k_{zz}^s = k_{iso}^s$, where x, y, and z refer to the machine direction, cross direction and

thickness direction (through-plane), respectively. Saturated permeability for such a medium in any direction is given by

$$\frac{1}{4\varepsilon} = \frac{1}{3} + \frac{5}{6}\frac{\sqrt{k^s_{iso}}}{r_f}\frac{K_1\left(\frac{r_f}{\sqrt{k^s_{iso}}}\right)}{K_0\left(\frac{r_f}{\sqrt{k^s_{iso}}}\right)} \tag{4.9}$$

where K_0 and K_1 are zero- and first-order modified Bessel functions of the second kind. Note that Equation 4.9 (and Equations 4.10 and 4.11 to follow) must be solved numerically. Layered fibrous media, the fibers of which have effectively no through-plane orientation, but random in-plane orientation (Figure 4.1a), is another case to which Spielman and Goren's relations apply. The relation for this configuration is given by

$$\frac{1}{4\varepsilon} = \frac{1}{4} + \frac{3}{4}\frac{\sqrt{k^s_{xx}}}{r_f}\frac{K_1\left(\frac{r_f}{\sqrt{k^s_{xx}}}\right)}{K_0\left(\frac{r_f}{\sqrt{k^s_{xx}}}\right)} \quad \text{(In-plane)} \tag{4.10a}$$

$$\frac{1}{4\varepsilon} = \frac{1}{2} + \frac{\sqrt{k^s_{zz}}}{r_f}\frac{K_1\left(\frac{r_f}{\sqrt{k^s_{zz}}}\right)}{K_0\left(\frac{r_f}{\sqrt{k^s_{zz}}}\right)} \quad \text{(Through-plane)} \tag{4.10b}$$

where $k^s_{xx} = k^s_{yy}$, since such a geometry is isotropic in the in-plane directions.

The third case to which the Spielman and Goren relations can be applied is that of a fibrous structure with disordered unidirectional fiber orientation. The correlation for the unidirectional geometry is

$$\frac{1}{4\varepsilon} = \frac{1}{2}\frac{\sqrt{k_{xx}^s}}{r_f}\frac{K_1\left(\frac{r_f}{\sqrt{k_{xx}^s}}\right)}{K_0\left(\frac{r_f}{\sqrt{k_{xx}^s}}\right)} \tag{4.11}$$

where the *x*-direction represents the direction along the fibers.

Spielman and Goren (1968) did not develop a correlation for permeability in the directions perpendicular to fiber orientation ($k_{yy}^s = k_{zz}^s$ in this case). Tahir and Tafreshi (2009) and Fotovati *et al.* (2010) performed series of flow simulations in a number of virtual fibrous structures to conclude that the through-plane permeability of a layered fibrous medium is not affected by the in-plane orientation of its fibers, which is consistent with the lack of a specific correlation for permeability perpendicular to the fibers in the case of unidirectional fibers.

Ultimately, permeability is inversely related to SVF, as fluid penetration into a medium is a more tortuous process when more solid volume obstructs flow. Likewise, permeability being directly related to fiber diameter is intuitive. For a constant SVF, a larger fiber diameter consolidates the given solid mass into fewer fibers, thereby reducing the solid surface area in contact with the fluid, leading to less friction.

Capillary Pressure: Full Morphology

To briefly recap, and to put it into the context of the results to follow, the particular method from Chapter 3 that was utilized for the capillary pressure relations for the Richards Equation were performed using the Full Morphology method. Figure 4.2, for example, shows

the effect of fiber orientation on $p_c(S)$ for the same family of structures shown in Figure 4.1, fitted with a correlation from Landeryou *et al*. (2005):

$$p_{Lan} = C_{Lan} \ln(S) + b_{Lan} \tag{4.12}$$

The media simulated for in Figure 4.3 are all layered, with fibers given no through-plane (parallel to flow) orientation. Their in-plane (normal to flow) orientation varies between fully random, fully unidirectional in the *x*-direction, and a machined directionality (MD) favoring the *x*-direction. As can be seen in the figure, capillary pressure is shown to be slightly stronger (more negative) when fiber orientation favors one direction over the other, with randomly oriented fibers showing the lowest capillarity.

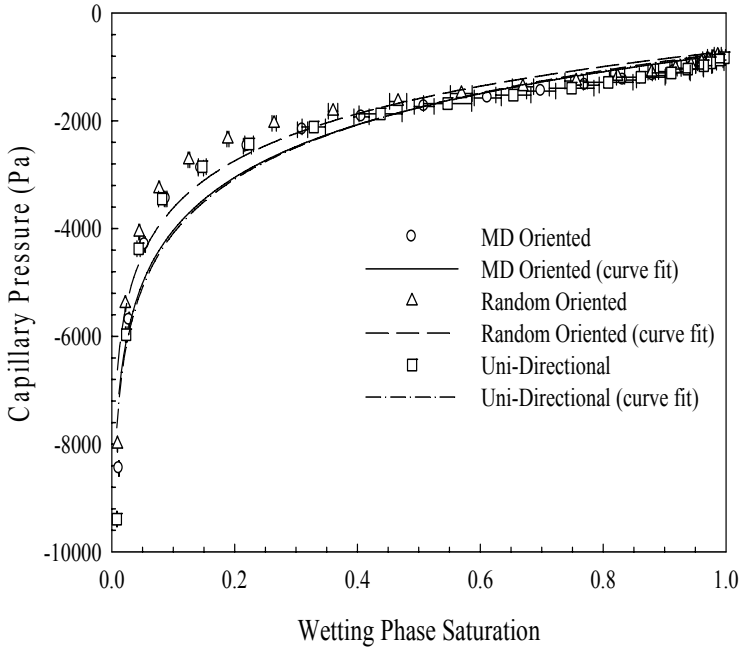

Figure 4.2: Capillary pressure versus saturation for virtual fibrous structures with an SVF of 10%, a fiber diameter of 10 μm, and a contact angle of 60°.

4.2 The Richards Equation

For convenience, the form of the Richards equation being solved in this section is restated here as

$$\Phi\frac{\partial S}{\partial t}-\frac{1}{\mu}\left(\frac{\partial}{\partial x}\left(k_{xx}(S)\frac{\partial p_c}{\partial S}\frac{\partial S}{\partial x}\right)+\frac{\partial}{\partial y}\left(k_{yy}(S)\frac{\partial p_c}{\partial S}\frac{\partial S}{\partial y}\right)+\frac{\partial}{\partial z}\left(k_{zz}(S)\frac{\partial p_c}{\partial S}\frac{\partial S}{\partial z}\right)\right)=0 \tag{4.13}$$

The equation is solved in the finite element environment with the FlexPDE commercial code. The following two subsections will explain two different studies performed: one for absorption in thin fibrous sheets, and one for drainage from wet wipes.

Effect of Fiber Orientation on Absorption

We first examine a solution of Equation 4.13 in two dimensions, in which the microscale information reviewed so far in this chapter is put toward a solution in the macroscale. The meshed domain with associated boundary conditions is shown in Figure 4.4. The material is assumed to be a thin 5cm × 5cm sheet with a SVF of 10% and a fiber diameter of 15 μm. Taking advantage of the existing symmetry, only one quarter of the sheet surface is considered for the calculations. A fully saturated (S = 1) source of infinite moisture is considered in the lower left-hand corner of the domain. For the top and right boundaries, a Neumann (zero flux) boundary condition is considered. The two remaining boundaries were treated as symmetric boundaries.

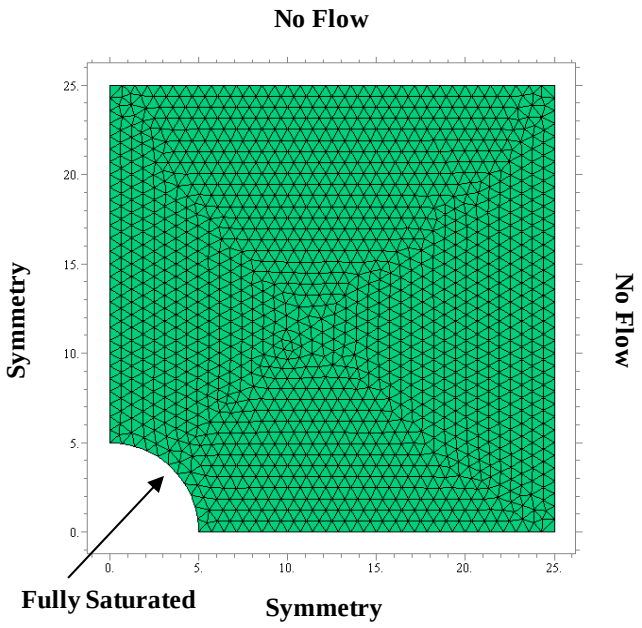

Figure 4.4: Solution domain and its associated boundary conditions.

Figure 4.5 shows the contour plots of saturation in the isotropic, MD-oriented, and unidirectional media at two different moments of t = 0.41 and 4.2 seconds. $p_c(S)$ for Equation 4.13 in this case uses the results previously shown in Figure 4.3, obtained via curve fitting with Equation 4.12 (Landeryou *et al*., 2005). The coefficients for Equation 4.12 were found to be (C_{Lan} = 1261.4, b_{Lan} = -714), (C_{Lan} = 1415.99, b_{Lan} = -775.36), and (C_{Lan} = 1453.87, b_{Lan} = -745.17) for isotropic, MD-oriented, and unidirectional sheets respectively. Permeability $k_{ij}(S)$ was determined using the FM–Stokes method described in Section 4.1, with the values accompanying Figure 4.2. It can be seen that water spreads almost isotropically in the sheet with random fiber orientation, but penetrates much faster in the direction of the fibers in the media with oriented microstructures leading to elliptical spread patterns. The reason for this is that, as a wetting fluid enters a fibrous structure, it flows along the length of the fibers much more easily than past them, as it is the path of less resistance. If the majority of a material's fibers are in the x-direction, then fluid flow through the medium will be more prevalent in the x-direction. The

difference in the values of single phase permeability in the x- and y-directions k_{xx}^{s} and k_{yy}^{s} for a given microstructure, reflects this behavior. k_{xx}^{s} and k_{yy}^{s} values for sheets with nearly random orientation are close together, while k_{xx}^{s} for the MD-oriented and unidirectional media is greater than k_{yy}^{s} by a factor of 2, and a factor of 3 respectively.

To obtain more quantitative comparisons between fluid penetration in the above sheets, saturation values are plotted along the $x = 0$ and $y = 0$ lines (i.e., vertical and horizontal boundaries) for isotropic, MD-oriented, and unidirectional media at four different moments of time. Figure 4.6 illustrates these plots, with a target overlaid on each plot for the corresponding dimensionless x or y value of 0.65, and the corresponding time of 1.54 seconds into penetration. As can be seen, at $t = 1.54$ sec, saturation is $S = 0.60$, $S = 0.68$, and $S = 0.84$ at a normalized distance of 0.65 in the x-direction, and $S = 0.45$, $S = 0.40$, and $S = 0.20$ at the same distance in the y-direction, for our isotropic, MD-oriented, and unidirectional media, respectively.

Finally, a comparison between the total amounts of water absorbed by the above media over time is presented in Figure 4.7. It can be seen that increasing the directionality of the fibers in a medium can help increase the rate of moisture uptake, as the rate is highest in the unidirectional and lowest in the isotropic media. This is supported not only by permeability, but also by the capillary pressure coefficients from Equation 4.12.

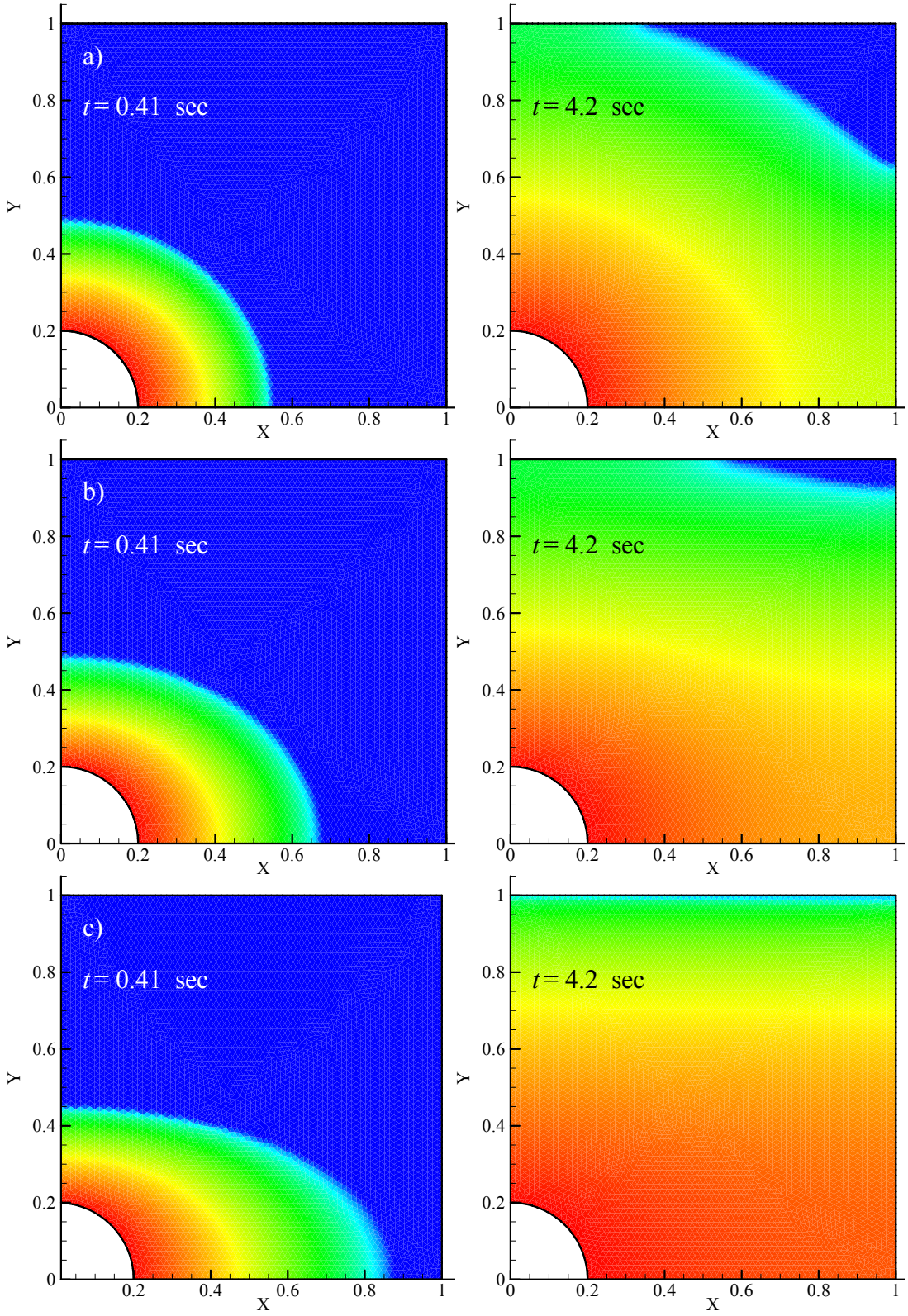

Figure 4.5: Contour plots of saturation at t = 0.41 and 4.2 seconds for a) Near-isotropic, b) MD-oriented and c) Unidirectional structures. Different colors from red to blue represent different saturation values from one to zero, respectively. Coordinates are normalized by the sheet's dimensions.

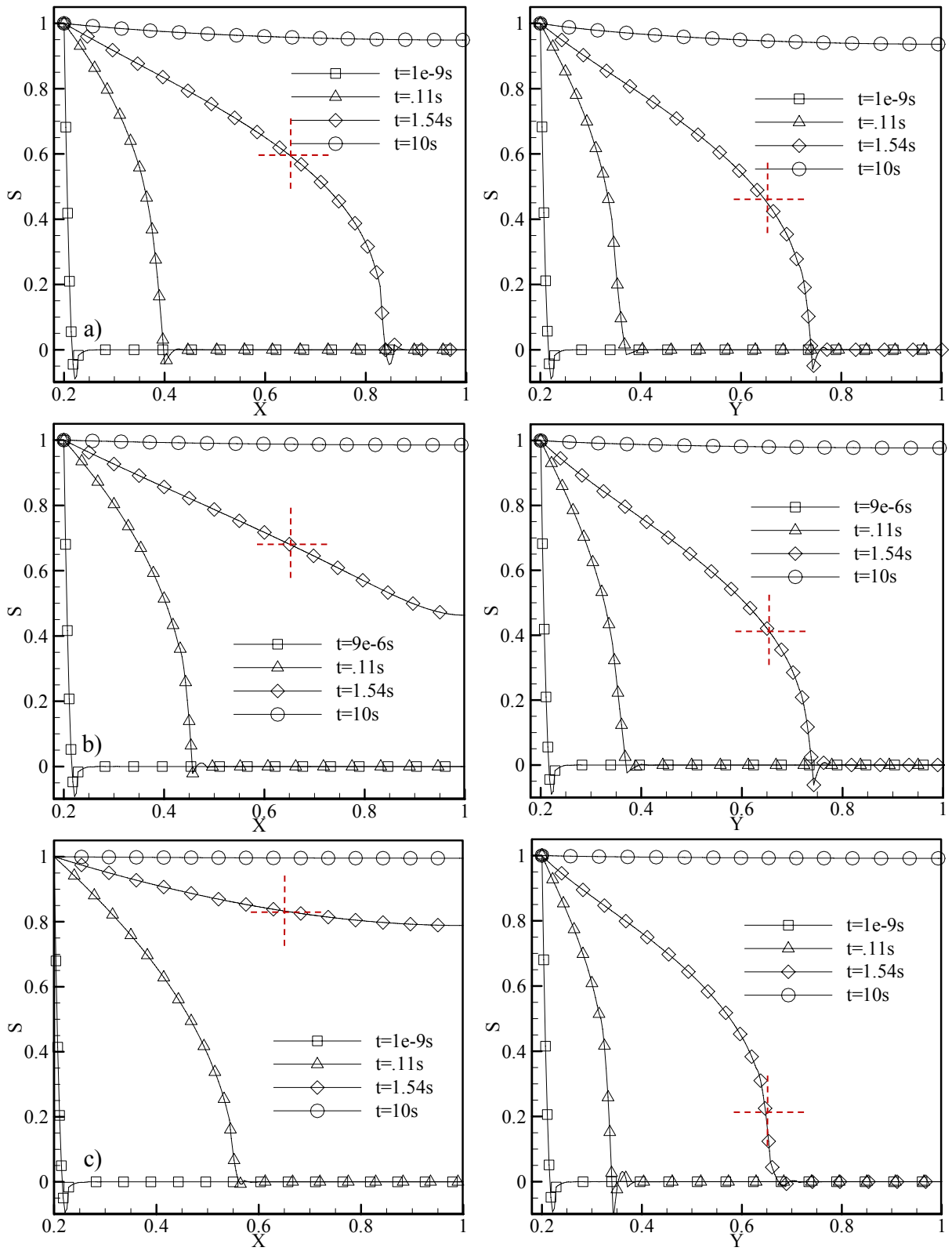

Figure 4.6: Saturation values along y = 0 and along x = 0 at different times of t = 9e-6, 0.11, 1.54, and 10 seconds) for a) Near-isotropic, b) MD-oriented, c) Unidirectional structures. Coordinates are normalized by the sheet's dimensions. Target corresponds to dimensionless distance of 6.5 in corresponding x or y, and time at 1.54 seconds.

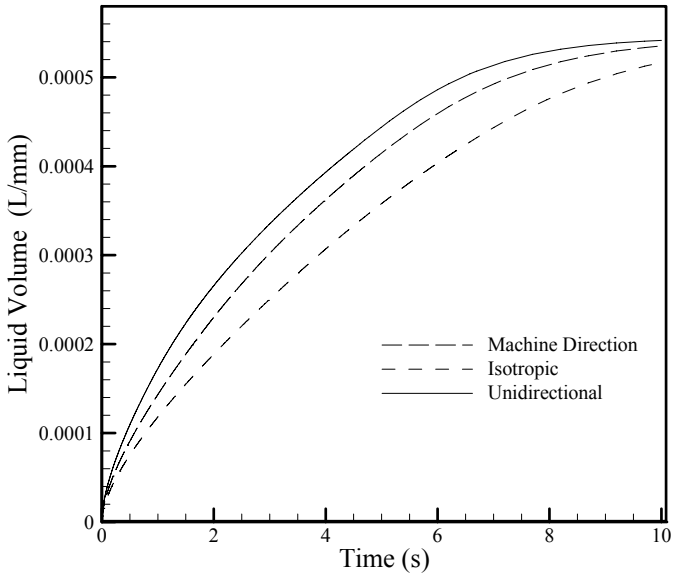

Figure 4.7: Plot of liquid volume versus time for Near-isotropic, MD-oriented, and unidirectional media. Note that the reported values are for the domain size shown in Figure 4.5 (one quarter of the sheet).

Calling back to Chapter 2, also compare our results with the analytical model of Marmur (1988)—Equation 2.5. Recall, that the simple relationship obtained by Marmur has also been used by Borhan and Rungta (1993) and Danino and Marmur (1994) for studying in-plane radial motion of fluids in paper. Note that Marmur's model is developed for isotropic media. The assumptions employed in the work of Marmur are the same as those used in the standard Lucas–Washburn model, and so do not consider the partially-saturated region of the media. For convenience, Equation 2.5 for the radial penetration of fluids in thin porous media is restated here as

$$\left(\frac{r}{r_0}\right)^2\left(\ln\frac{r}{r_0}-\frac{1}{2}\right)+\frac{1}{2}=\frac{\sigma d_{cap}\cos\theta_{cap}}{12\mu r_0^2}t \tag{4.14}$$

where R is the radius of the wetted area (assumed to be fully-saturated), r_0 is the radius of the liquid source, d_{cap} is the average pore diameter inside the medium. Note that d_{cap} is a parameter that cannot be directly measured or estimated. Here, using the information presented in Figure

4.7, we calculate a radius for an imaginary fully-saturated circular region in the media as a function of time (note that the values reported in Figure 4.7 are for one fourth of the sheet). Equation 4.14 was then fitted to our results, and a value for the average pore radius d_{cap} was obtained to be about 40 μm (see Figure 4.8).

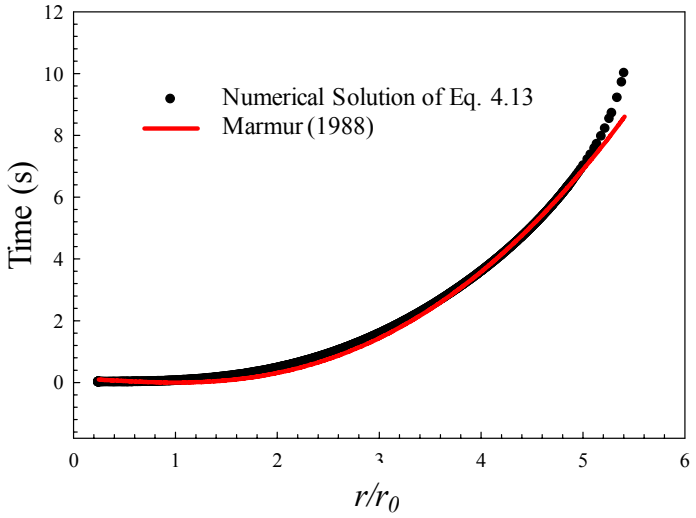

Figure 4.8: Radius of an imaginary fully-saturated circular region is calculated from the results of Figure 4.5. The equation derived by Marmur (1988) is fitted to our results.

Drainage from Wet Fibrous Wipes

This subsection examines an approach for fluid drainage that solves the Richards equation in one dimension, expressed here as:

$$\frac{\partial S}{\partial t}+\frac{\partial}{\partial z}\left(D_{zz}^{fm}(S)\frac{\partial S}{\partial z}\right)=0 \tag{4.15}$$

where

$$D_{zz}(S)=-\frac{k_{zz}(S)}{\Phi\mu}\frac{\partial p}{\partial S} \tag{4.16}$$

Equation 4.16 simply groups all the microstructure and nonlinear terms into a single diffusive coefficient. This model utilizes a special diffusive boundary condition in order to facilitate the transfer of fluid from the wipe to the surface. Figure 4.9 illustrates what this means. In Figure 4.9a, the physical situation in question is displayed, in which a wet fibrous wipe moves across a dry impermeable surface. Figure 4.9b illustrates the condition standing in its place within our model: a fictitious porous surface (initially dry) that provides a "saturation sink" to promote drainage from the wipe.

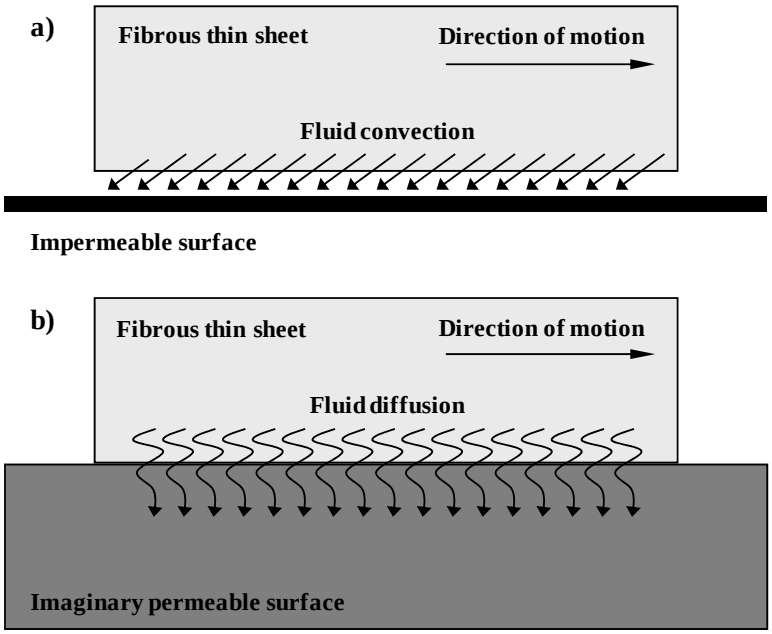

Figure 4.9: (a) A schematic of the actual system showing release of fluid from a moving wet sheet onto a solid surface. (b) The boundary treatment used for our model, where the solid surface is replaced by a fictitious fluid-absorbing porous layer.

The moisture content of this fictitious layer is periodically set to zero to resemble motion of the sheet on a dry surface. The resetting period is calculated from the length ℓ and speed V_w of the sheet:

$$\Delta t = \frac{\ell}{V_w} \tag{4.17}$$

This characteristic time essentially corresponds to the amount of time required for an experimental sheet to traverse its own length along a dry surface. The rate of fluid infiltration in our fictitious porous layer is also calculated via the Richards equation (4.14) with a diffusive coefficient defined as (diffusivity of the fictitious layer denoted by the superscript *fl*)

$$D_{zz}^{fl} = 7.87 \cos\theta_s \, k_d \, V_w \tag{4.18}$$

where θ_s is the contact angle between liquid and solid surface, and k_d is a constant to be found from experiment at a given speed (0.127 m/s here). For the interface between the fibrous sheet and our fictitious layer we consider equal saturation flux in the *z*-direction:

$$D_{zz}^{fm} \left.\frac{\partial S}{\partial z}\right|_{z=0^+} = D_{zz}^{fl} \left.\frac{\partial S}{\partial z}\right|_{z=0^-} \tag{4.19}$$

The fictitious layer should be so large that it always stays partially dry during the prescribed Δt time interval. For the other boundaries of the solution domain, we considered no-flow boundary conditions ($\partial S / \partial n = 0$, where *n* is normal to the surface). The Richards equation is once again simulated using the FlexPDE code. Figure 4.10a summarizes the simulation process in the form of a flowchart, with Figure 4.10b showing a sample progression of fluid transport from the wipe (initially red in the top image) to the porous surface layer (initially purple due to its dryness, and periodically reset). As is shown, saturation in the fictitious layer is reset every Δt seconds, with saturation in the wipe retained.

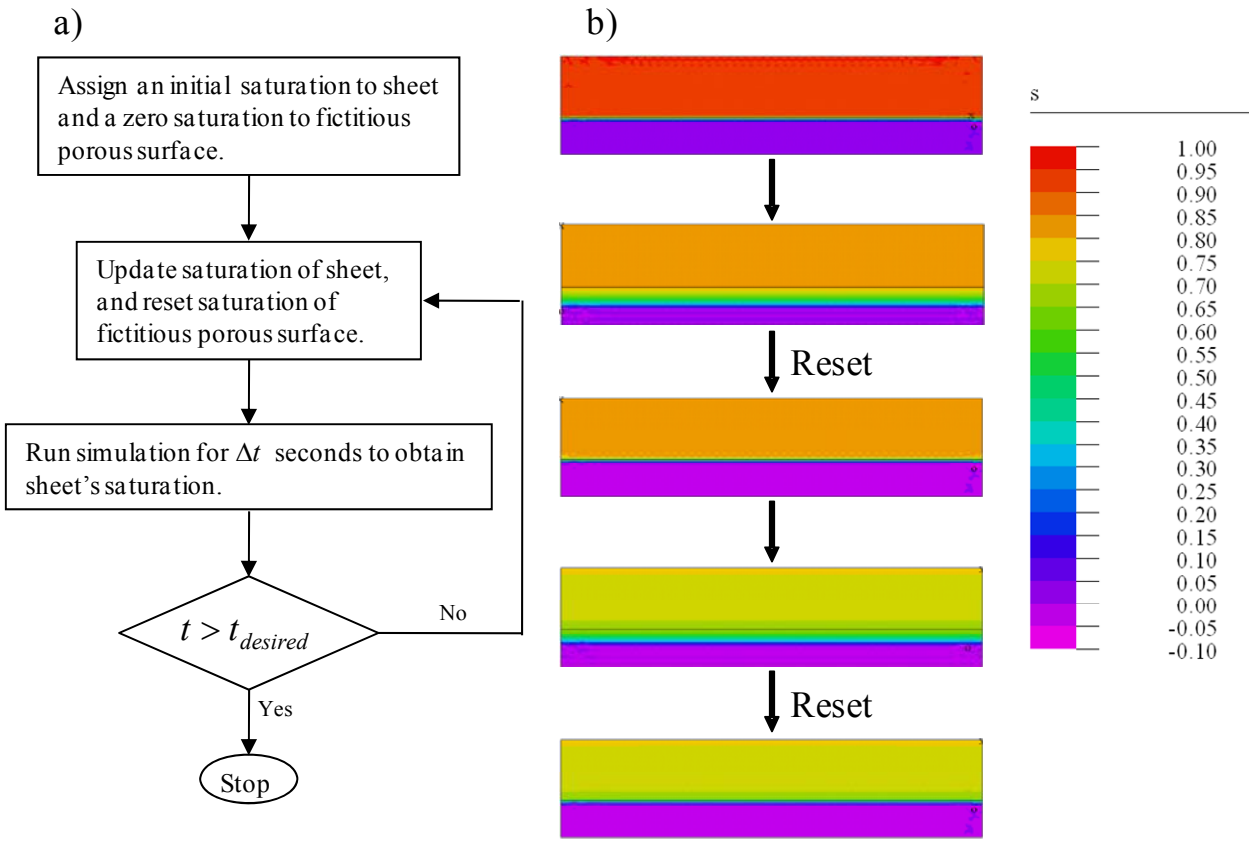

Figure 4.10: (a) Flow chart of the simulation procedure. (b) Sample simulation domain demonstrating the diffusion of fluid from the wipe (red in the top image) into the fictitious porous layer (purple in the top image). Surface saturation is periodically reset to zero as governed by Equation 4.17.

As mentioned earlier, an empirical coefficient k_d is required to adjust predictions of our numerical model. We therefore designed a computer controlled test rig that allows testing a wet sheet of nonwoven fabric on a designated large flat surface. Our test rig is comprised of a sheet holder connected to a mechanical arm that moves the holder on the flat surface. The holder is a rigid panel on which a relatively soft rubber pad is mounted. Partially-saturated fibrous sheets are then mounted on the rubber pad and tested on the surface (see Figure 4.11). Note that our test setup is designed in such a way that the distance between the sheet holder and the solid surface is controlled during the experiment, and therefore, weight of the system has no influence on the test results. We weigh our 0.2m×0.2m PET sheets before and after the tests using a sensitive scale

with 1 mg resolution to obtain the mass of the fluid released from the sheets. Our system is designed in such a way that the sheets only travel on dry surfaces. This has been achieved by defining a non-intersecting trajectory of path for the sheet holder on the test surface. Our setup allows moving the sheet holder with different speeds and in different directions. The solid surface considered for the tests was a smooth laminated plywood panel.

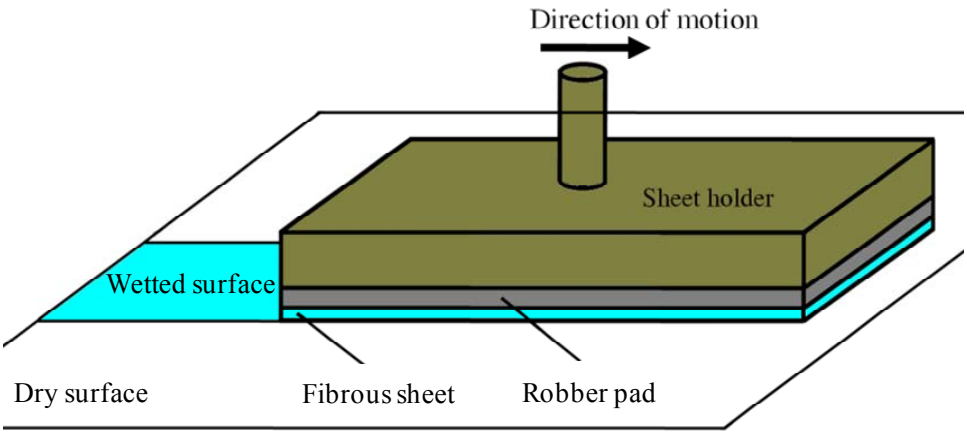

Figure 4.11: A schematic illustration of the test procedure.

The sheets are saturated by immersing them in our test fluid for 10 minutes. The extra fluid is then squeezed out of the sheets until a desired weight (corresponding to desired initial saturation) is reached with a margin of error generally less than 5%. To minimize statistical error, each test has been repeated five times.

For the simulations, the PET fabric and the surface were measured to have contact angles equal to 74.5° and 40° respectively. The PET wipes have an SVF of 7.6% and fiber diameter of 12.6 µm. Capillary pressure was determined using the Full Morphology method and fitted to the equation of Haverkamp *et al*. (1977), restated here as

$$p_{Hav} = C_{Hav}\left(S^{-1} - 1\right)^{1/b_{Hav}} \tag{4.20}$$

with coefficients found to be C_{Hav} = 504.18 and b_{Hav} = 2.08. Saturated permeability k_{zz}^{s} was obtained using the relations of Spielman and Goren (1968), i.e., Equation 4.10b. Relative permeability $k_{zz}^{r}\left(S\right)$ is given by Equation 4.6, the relation from Brooks and Corey (1964), with n = 3.18 (Ashari and Tafreshi, 2009b). Figure 4.12a shows a comparison between simulation and experiment for the PET wipes. A value of 3.5×10^{-11} was fitted for Equation 4.18 using the data at V = 0.127 m/s. This is the only speed at which simulations were fitted using experimental data. Other tested velocities shown in Figure 4.12a are otherwise independent of one another, and show good agreement. Figure 4.12b shows the response of this simulation method to changing the hydrophilicity of the surface. The response is as one would expect, with no drainage when the surface is hydrophilic, and increasing drainage with increasing hydrophilicity. This effect was also confirmed experimentally, as is shown in Figure 4.12c. The surface was replaced with wax paper, and the experiment was run at a speed of 0.296 m/s with and without it. There is an initial drop in fluid content for the wax paper due to unavoidable experimental errors, but subsequent drainage is almost nonexistent.

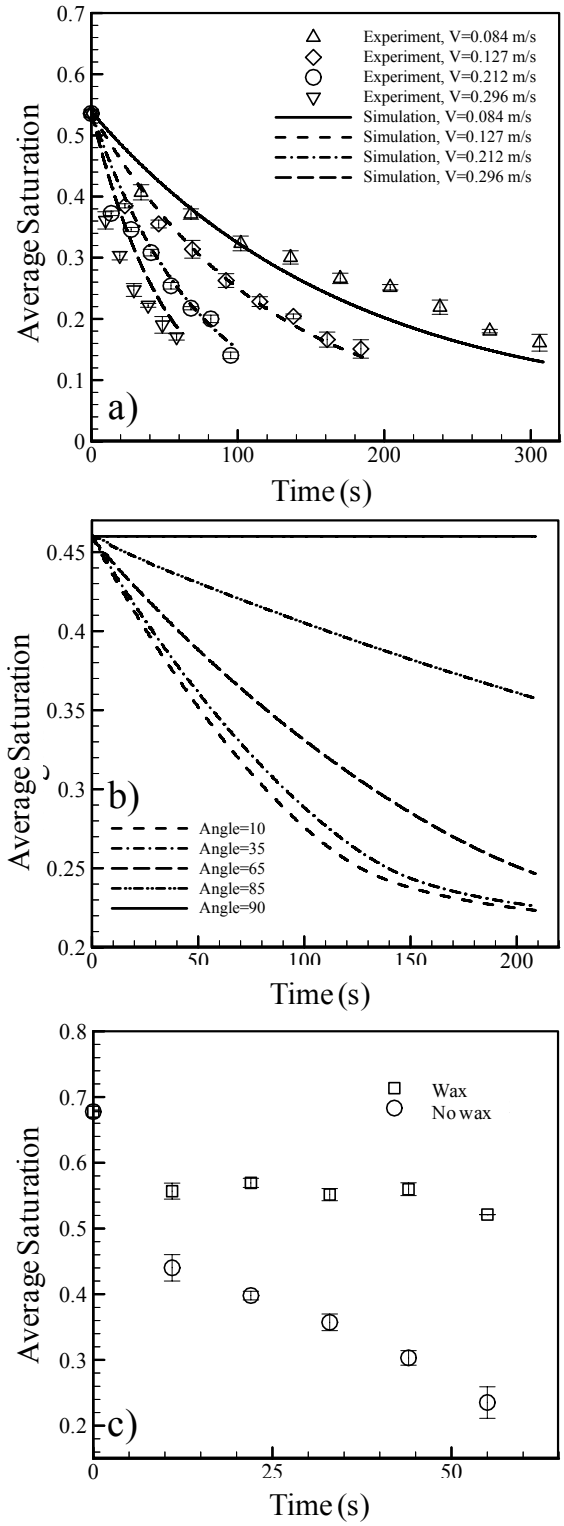

Figure 4.12: (a) Average saturation obtained from our simulations and compared with experiment for PET samples at different speeds. (b) Effect of surface hydrophilicity on the release performance of PET sheets at a speed of 0.127m/s. (c) Experimental comparison of drainage from PET sheets when surface is changed to wax paper (contact angle of 90°); wipe speed is 0.296 m/s.

4.3 Chapter Conclusions

In this chapter, we have reviewed the extension of one of the absorption capillary pressure models discussed in this thesis into simulating the Richards equation for fluid transport through porous media. Being nonlinear, the Richards Equation requires capillary pressure and permeability information on the microscale (scale of the fibers themselves). Once that information is provided, be it through simulation, analytic/empirical expressions, or a combination of the two, the Richards equation can be used to model fluid transport on the macroscale (scale of the fabric), expressing fluid saturation as a function of time and space.

We then covered two models that utilize the Richards equation. The first involved absorption, and established a relationship between fluid spread and fiber orientation. The results show that in thin fibrous sheets, the anisotropic directionality of fluid spread favors the anisotropic directionality of the fibers in the wipe. Moreover, the total fluid absorption in a given time is higher when the orientation of the fibers favors one direction over another.

Finally, we examined a model for fluid drainage from wipes being moved across a dry surface. The Richards equation was solved in the thickness direction only, and fluid drainage was facilitated by modeling the dry table as an absorbing porous surface. To capture the continuing motion of the fabric, this fictitious surface has its saturation periodically reset to zero to allow continued drainage from the wipe as if it is continuing to move across a dry surface. This method was also compared against experiment using a test rig designed to move a wet wipe across a set path, and good agreement was observed.

Chapter 5

Resistance of Fibrous Superhydrophobic Coatings to Hydrostatic Pressures[5]

This chapter will focus on two capillary pressure models for predicting the critical pressure (i.e., the pressure beyond which a superhydrophobic coating fails to withstand the pressure of the water penetrating into it) for electrospun fiber coatings. First, we will revisit the Full Morphology (FM) method, used earlier in this thesis in the context of absorption, which will be tailored accordingly for this application. In this study, we will examine unimidal and bimodal fiber diameter distributions, and also look at the effect of using orthogonally layered coatings instead of randomly laid coatings. Figure 5.1 shows an example of an electrospun coating with orthogonal layering, the spacing of which can be more tightly controlled than a randomly-laid coating as discussed in Chapter 2, resulting in pore geometries with higher critical pressures and pressures easier to predict. After our FM pressure study, we will revisit the technique of determining the shape of the air–water interface by minimizing surface energy established in Section 2.1, modifying it for fibrous superhydrophobic coatings. Finally, having investigated the

[5] Some of the contents of this chapter appears (or will appear) in the following publications:

- T.M. Bucher., B. Emami, H.V. Tafreshi, M. Gad-el-Hak, G.C. Tepper, "Modeling resistance of nanofibrous superhydrophobic coatings to hydrostatic pressures: the role of microstructure," *Physics of Fluids 24*, 022109 (2012)
- T.M. Bucher and H.V. Tafreshi, "Effect of wetting heterogeneity on capillarity of orthogonallylayered fibrous coatings," *to be submitted*
- T.M. Bucher, H.V. Tafreshi, G.C. Tepper, "Modeling performance of thin fibrous coatings with orthogonally layered nanofibers for improved aerosol filtration," *Powder Technology* 249, 243–253 (2013)

unique properties of orthogonally laid electrospun fiber coatings, we will briefly a study examining their application for improved aerosol filtration.

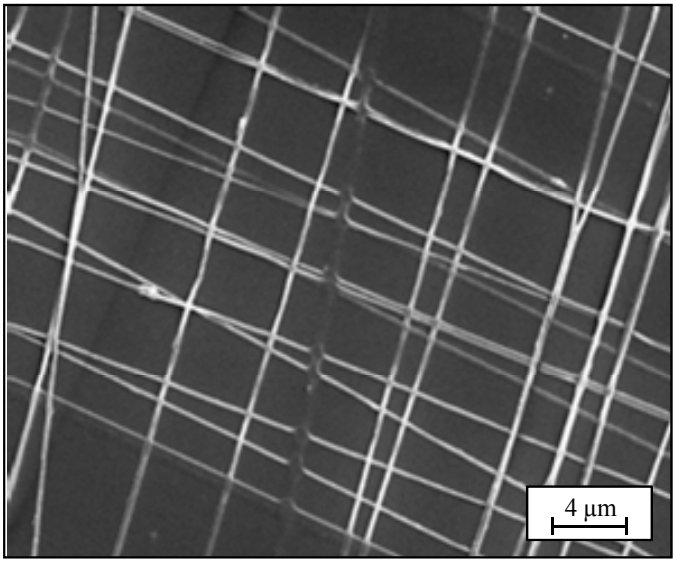

Figure 5.1: Example of an electrospun nanofiber coating with orthogonal layering, resulting in controlled parameters conductive to use as a superhydrophobic coating.

5.1 Critical Pressure via Full Morphology Simulation

Virtual Fibrous Structures

To generate 3-D virtual models resembling the microstructure of an electrospun fibrous medium, we have developed a computer program to produce random and ordered fibrous structures with different fiber diameters, porosities, thicknesses, and orientations. To better mimic the planar microstructure of electrospun fiberwebs, no through-plane orientation has been considered for the fibers. Virtual fibrous structures are generated with random and orthogonal fiber orientations to emulate the coatings. Note that material density of the electrospun fibers is

assumed to be constant regardless of their diameters, as the choice of fiber density and its variations with diameter are of minor importance in our modeling.

Figure 5.2a depicts a virtual bimodal fibrous structure with a random in-plane fiber orientation. Note that the fibers are allowed to overlap and cross through each other. This is a simplification considered in our simulations with structures having random fiber orientations, which helps us circumvent some of the complexities involved in generating size-independent disordered fibrous domains, as reported in our previous publications (Maze *et al*., 2007a, 2007b). Allowing the fibers in each layer to cross through one another also helps us to better control the SVF of the virtual coatings. Based on our previous experience with modeling transport properties of fibrous media, we believe that such a simplification has a negligible influence on the accuracy of the results and conclusions reported in this paper, especially when working with nanofibers (Tahir and Tafreshi, 2009; Hosseini and Tafreshi, 2010). It is important to note that SVF is an implicit parameter in these coatings, representing the ratio of structure volume occupied by solid fibers to the total volume. The term is arrived upon differently for random coatings and orthogonal coatings. Recall that in experiment, randomly laid fibers form curly filaments when deposited on a flat substrate, stacked on top of one another with loop diameters (i.e., length scales) varying from the order of microns to the order millimeters. Therefore, the simulation domain should be much larger than the length scale of the surface morphology; otherwise the SVF cannot be accurately predicted. Unfortunately, with current computational power, our simulation domains must be much smaller than the few millimeters that would be necessary to cover the entire range when the fibers are as small as 100 nm (i.e., electrospun fibers). Moreover, modeling such random curvatures and their effect on the system in intricate

detail is, in general, a computational task beyond the scope of this work, and for the sake of simplicity, we model the fibers as straight cylinders and allow them to interpenetrate, so that a desired SVF can be achieved on the scale of our simulations when modeling electrospun fibrous structures. Experimentally, there is no way of knowing the SVF of a fiber mat prior to production. This is because of the complicated loops and curves the fibers form, leading to a non-linear increase in the coating's thickness with time (time being proportional, but not necessarily linearly, to deposited mass). Therefore, the only way one can know the SVF of a random-laid coating is by characterizing its physical properties (e.g., weight per unit area, thickness …) after the coating is made. In our model, once a fibrous structure is generated, its volume is descretized into voxels, and the voxels can only be filled (solid fiber) or empty (air or water). The SVF is the ratio of the solid voxels to the total number of voxels, so there is no double-counting of the volume of overlapping cylinders. Because fibers are allowed to overlap and assume orientations askew to the domain boundaries, changes in SVF are more incremental as fibers are added. This allows the virtual random structures to be generated with an input SVF upon which to target.

In the case of orthogonal fibrous structures, the fibers in a given layer all face either the *x*- or *y*-direction. What one could consider to be the smallest divisible "unit layer" in a given sample of these structures would be two layers of fine fibers, and two layers of coarse fibers. Note that any given layer only consists of only one type of fiber. Given the greater control of fiber spacing and layering when creating orthogonal coatings, we separate the coarse and fine fibers into distinct layers in our orthogonal structures. In the interest of encouraging the first layer of the coating to act as the bottleneck for water intrusion, with fiber spacing as constrictive

as reasonably achievable, the outermost pair of layers in our orthogonal coatings is comprised of fine fibers. Since the fibers in each layer are parallel to each other, there are no concerns with fibers crossing through one another as there were for the random structures. As can be seen in Figure 5.2b, fibers in adjacent layers lie over and under those of their neighboring layers without interpenetrating, as one should expect. Here SVF does not have to be an input, as was the case for mats with overlapping fibers. In this case, SVF is an output of our structure generation algorithm based on fiber population and spacing, which is, of course, more realistic insofar as how one would estimate the SVF for a given fabricated coating.

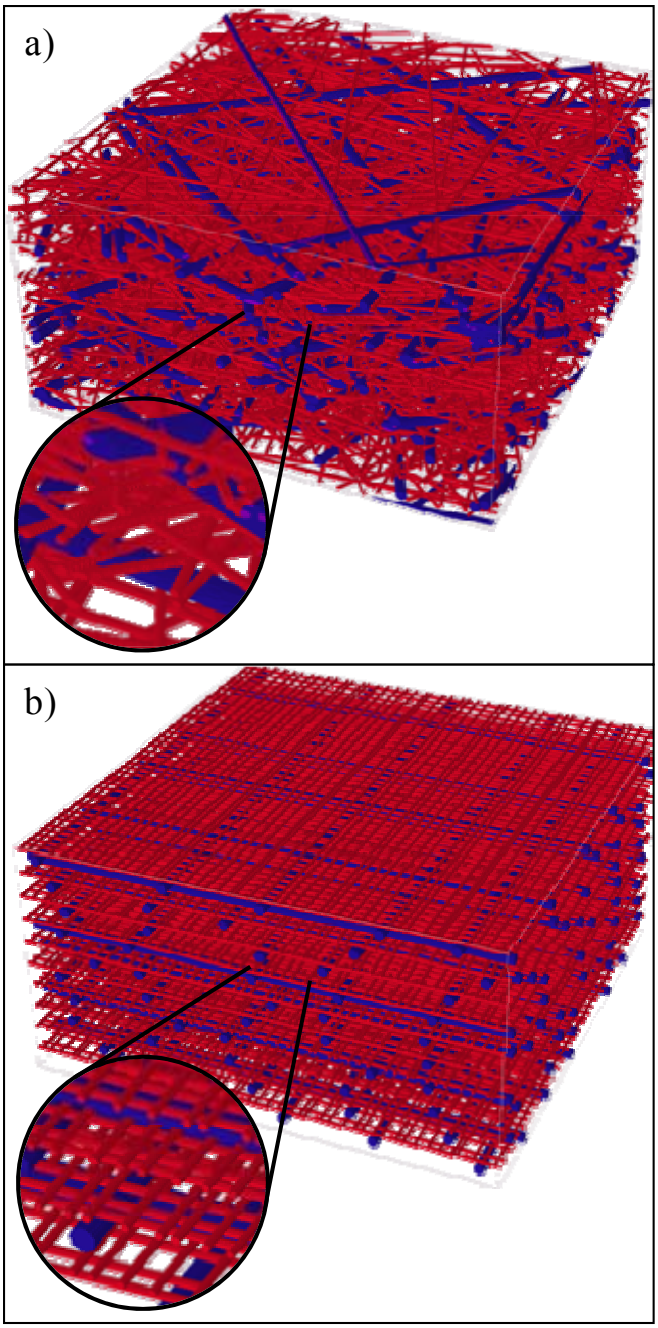

Figure 5.2: Samples of our virtual, three dimensional, bimodal fibrous structures used in our numerical study, comprised either of: a) layered, randomly oriented fibers like those produced via electrospinning (SVF = 10%, df = 100 nm, Rcf = 3, nc = 0.1, t =9.6 μm) , or b) layered, orthogonally oriented fibers (SVF = 11.2%, df = 100 nm, Rcf = 3, nc = 0.1, t =9.6 μm).

In Figure 5.2b, note also the semi-random placement of fibers within a layer. It is assumed that while maintaining significantly high order in layers is possible, it will not achieve

perfect fiber spacing across a given layer. Therefore, we have decided to introduce an arbitrary degree of "noise" into an otherwise perfectly spaced structure, by allowing some limited randomness in fiber placement, while still restricting any fiber overlap. For a given fiber, the maximum random distance δ it can be placed from its even-spacing position is determined by

$$\delta = \min\left(\frac{(s/N)-d}{2},\ \eta d\right) \tag{5.1}$$

where s represents the in-plane size of the computational domain, N is equal to the number of fibers in the layer, and d represents fiber diameter (subscript c or f for coarse or fine fibers, respectively). The term η is equal to 3.5 for coarse fibers, and 2.72 for fine fibers, and is applied as an upper arbitrary, but educated, limit on the magnitude of δ. This upper limit is imposed in order to avoid generating virtual coatings with excessive non-homogeneity, which can lead to unnecessary statistical uncertainty in our simulation results. These values correspond to the maximum spacing deviation in fiber placement in a structure with an SVF of 11.2%, a fine fiber diameter of 100 nm, a coarse fiber diameter of 500 nm, and coarse fiber number fraction n_c of 0.1, in which case adjacent fibers in a layer would be able to touch, but not overlap. Any structure whose coarse and/or fine solutions to Equation 5.1 are greater than those prescribed for this given structure will be assigned the upper-limit value for their respective δ .

The relation between coarse or fine mass fraction m_c or m_f and their respective number fraction in a bimodal 3-D fibrous structure is given as (for more details see Tafreshi *et al*., 2009):

$$m_c = \frac{n_c d_c^2}{n_c d_c^2 + n_f d_f^2} \tag{5.2a}$$

$$m_f = \frac{n_f d_f^2}{n_c d_c^2 + n_f d_f^2} \tag{5.2b}$$

where n_f and n_c are, respectively, the number fraction of fine and coarse fibers, and d_c and d_f are coarse and fine fiber diameters. While mass fraction is a more practical representation experimentally, number fraction is a more convenient input for our simulations, especially for the orthogonal structures, which are constructed based on number of fibers. Nevertheless, one can be estimated from the other in most cases. In the case of the orthogonal structures number fraction can be determined using the rotational and translation speeds of the collector drum and polymer throughput, due to the controllability of fiber placement.

Critical Pressure Modeling and Validation

Capillary pressure of a hydrophobic porous material can be used to characterize its resistance against water intrusion. Previous works have shown that the relationship between capillary pressure and a medium's saturation is dependent on the size distribution of the medium's void spaces (Jaganathan *et al.*, 2008 and 2009b; Ashari and Tafreshi, 2009b). By increasing the hydrostatic pressure of water in which an air-filled hydrophobic material is submerged, water is able to pass into more constrictive spaces within the medium, thereby reducing the wetting-phase saturation. As the fluid interface boundary fully passes inside the coating, its superhydrophobicity diminishes, and thus its effectiveness is compromised.

In general, the required pressure for penetration of a non-wetting fluid into a porous medium filled with a wetting fluid is governed by the Young–Laplace equation, stated here in the context of the non-wetting phase as

$$p_c = -\frac{2\sigma\cos\theta}{r_{cap}} \tag{5.3}$$

where θ the contact angle of the non-wetting phase (in this case, water) on a flat sheet made of the same material as the fibers, taken arbitrarily to be 120 degrees for the simulations reported in this study, and r is of course the capillary radius. Higher pressure allows the water to penetrate through more constrictive void spaces, displacing the wetting fluid.

We will first present a force balance analysis to better examine the accuracy of our FM simulations, and to provide a comparison between the morphology-based and physics-based predictions. The force balance method as it pertains to superhydrophobic coatings was first presented by Zheng *et al*. (2005) and later by Lee and Kim (2009), for characterizing superhydrophobic surfaces made up of microfabricated vertical posts. These authors used a balance of forces to illustrate the interplay between the physical mechanisms that promote or inhibit meniscus instability. The balance of forces can be tailored to apply to a meniscus formed between parallel horizontal cylinders. This problem is slightly more complicated than the problem of vertical posts, as the cross-sectional area in the through-plane direction is not constant. We consider a unit cell for a domain in which parallel cylinders are stacked in the thickness direction, with no space between the cylinders above and below. Thus, the balance of forces for pressure, illustrated in Figure 5.3a, is expressed as

$$p_{FB} = \frac{\sigma\cos((3\pi/2)-\theta-\alpha)}{s_f/2 - r_f\sin\alpha} \tag{5.4}$$

where L_c is the pitch or center-to-center distance between parallel cylinders, α represents the angle made by the solid contact point of the meniscus with the peak of the surrounding cylinders,

and r_c is the radius of a cylinder. Notice that this equation bears a resemblance to Equation 3.15. It is indeed the same force balance equation across fibers, but with opposite sign (non-wetting phase in this chapter) and simplified to one fiber size and contact angle. Critical pressure is determined by differentiating Equation 5.4 with respect to α, and setting this derivative equal to zero. Equation 5.4 only represents critical pressure when the general α has the specific critical value α^*, which is determined numerically. Note that α^* is the value for α that maximizes the pressure. Therefore, with the pitch defined in terms of SVF ($L_f = \pi r_f / (2\varepsilon)$, where ε represents SVF), one obtains

$$p_{FB}^* = \frac{\sigma \cos((3\pi/2) - \theta - \alpha^*)}{r_f(\pi/(4\varepsilon) - \sin\alpha^*)} \tag{5.5}$$

The FM method uses Equation 5.3 to base the critical pressure threshold on the sphere with critical radius $r^* = s_f/2 - r_f$ to fit precisely between two fibers (see Figure 5.3b). Substituting into Equation (5.3) yields

$$p_{FM}^* = -\frac{2\sigma\cos\theta}{r_f(\pi/(4\varepsilon) - 1)} \tag{5.6}$$

Figure 5.3c shows α^* as a function of SVF for three different contact angles. It can be seen that α^*, the equilibrium position of the air–water interface just before breakup, decreases with increasing contact angle. This indicates that the interface breaks up at a location deeper inside the fibrous coating if the contact angle is lower. Figure 5.3c also shows that α^* increases by decreasing SVF of the coatings, which again indicates that the interface breakup takes place deeper inside the fibrous structure when the SVF is lower.

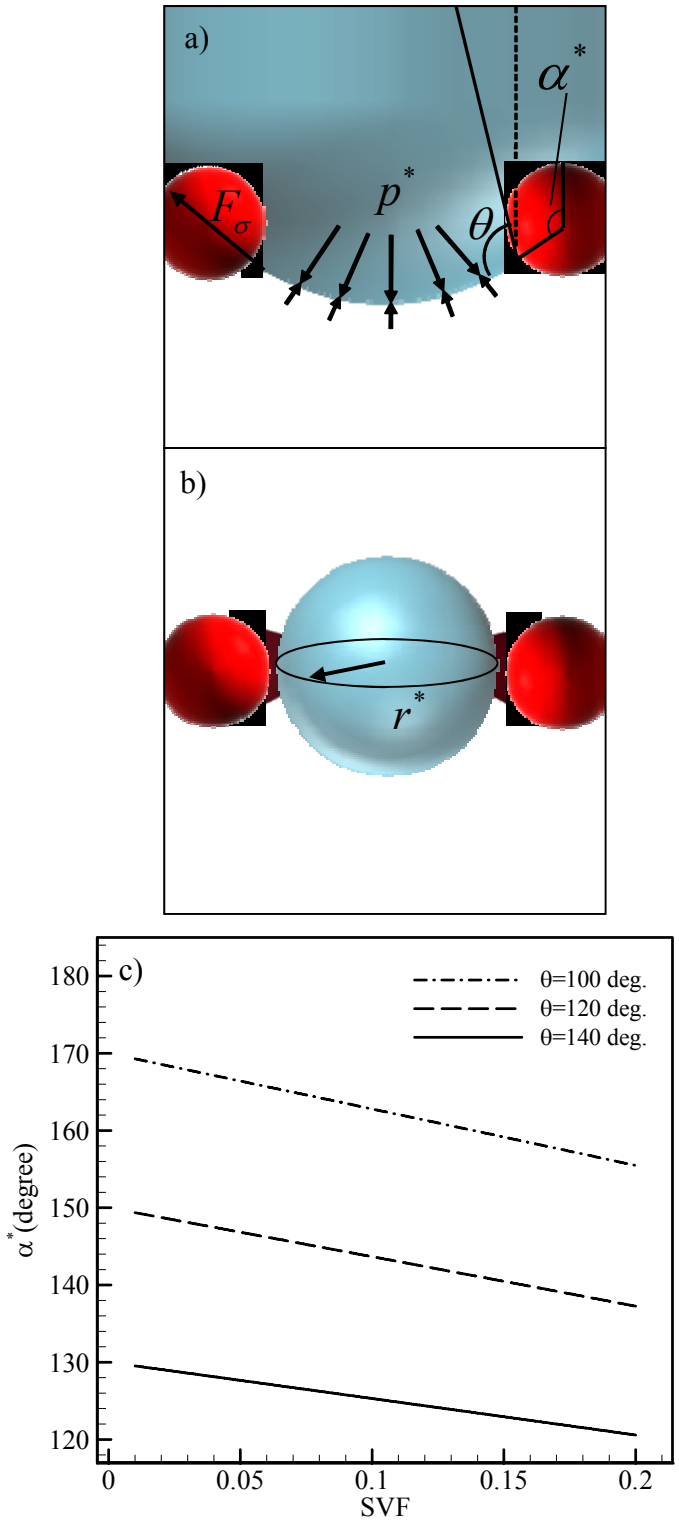

Figure 5.3: A visualization depicting the conceptual characterization of critical pressure for the case of ordered parallel fibers using the: a) force balance and b) FM approaches. The value of α^* associated with the force balance method is plotted (c) as a function of SVF for different contact angles.

Tuteja *et al*. (2008) developed an analytical model for superhydrophobic electrospun fiber mats, in which the fibers were considered to be parallel with one another and laid horizontally on a flat surface (one layer only) with a given fiber-to-fiber spacing. These authors applied the balance of forces for their geometry to produce two design criteria: "robustness angle" T^* and "robustness height" H^*. The critical pressures associated with the robustness angle and robustness height are shown with p_θ^* and p_H^*, where p_θ^* is the pressure required to force an interface sagging angle equal to that of the equilibrium contact angle between the interface and solid wall (fibers), and p_H^* is the pressure required for deflecting the air–water interface such that it dips into the pore space between two parallel fibers deep enough to touch the bottom flat surface:

$$p_\theta^* = \frac{\sigma \sin\theta}{r^*} \tag{5.7}$$

and

$$p_H^* = \frac{2\sigma(1-\cos\theta) r_f}{r^{*2}} \tag{5.8}$$

Figure 5.4a displays the critical pressure using each of the above four methods for a given fiber diameter and fluid contact angle as a function of SVF in a range relevant to electrospun fiber mats (1 to 20 %). It can be seen that good agreement exists between the predictions of the Full Morphology (FM) p_{FM}^*, force balance (FB) p_{FB}^*, and the robustness angle p_θ^* equations, whereas the robustness height p_H^* follows a different trend from the other relations.

To better investigate the behavior of the four models (Equations 5.5–5.8), we calculated $R^*_{FM} = p^*_{FM} / p^*_{FB}$, $R^*_{\theta} = p^*_{\theta} / p^*_{FB}$, and $R^*_{H} = p^*_{H} / p^*_{FB}$ and plotted them in Figure 5.4b–f versus contact angle and SVF. The prediction of our force balance approach has been chosen as the reference for comparing the above models with one another, as it does not have any of the restricting assumptions that have been considered in the other models discussed here, and so is expected to be the most accurate among them all. Figure 5.4b compares R^*_{FM}, R^*_{θ}, and R^*_{H} with one another when the contact angle is held constant at 120°, but the SVF is varied, whereas Figure 5.4c provides a similar comparison when the contact angle is varied, but the SVF is held constant at 10%. From Figures 5.4b and 5.4c, one can conclude that robustness height under-predicts the actual critical pressure, until SVF approaches the neighborhood of 18%, beyond which it over-predicts critical pressure; the FM method is accurate only when the contact angle is around 120°; and the robustness angle method performs reasonably well when compared to the force balance method.

To further study the degree of deviation of the FM, robustness angle, and robustness height methods from our general force balance method when SVF and contact angle are varied, surface contour plots of R^*_{FM}, R^*_{θ}, and R^*_{H} are shown in Figures 5.4d, 5.4e and 5.4f, respectively. As can be seen in Figure 5.4d, R^*_{FM} deviates quite significantly from the predictions of our general force balance method when the equilibrium contact angle is varied in a relevant range of hydrophobic surfaces (e.g., 90–140 degrees). However, changing SVF does not seem to affect the predictions of the FM method, indicating that when the error associated with the FM method is determined for a given contact angle and SVF, one can confidently use this method with other SVFs as long as the material of the fibers (and, of course, the fluid) is not changed. The

robustness angle method seems to perform acceptably well with regards to variations in contact angle and SVF (see Figure 5.4e). The robustness height method seems to be least sensitive to variations in contact angle. However, this method consistently under-predicts critical pressure in the typical range of SVF for fibrous materials. As mentioned before, predictions of the robustness height method seem to be accurate only if the SVF is in the neighborhood of 18%, and over-predict critical pressure thereafter. The inaccuracy in the predictions of the robustness height model is believed to originate from the model's underlying assumption that a critical pressure is reached when the interface dips into the pore between two parallel fibers deeply enough to touch a bottom horizontal surface directly beneath those fibers. In other words, a stable air–water interface can exist even when the meniscus is deflected beyond what would be considered the bottom surface in the robustness height model. It can be expected that as the SVF increases (fibers are closer together), the deflection of the meniscus becomes less significant, and the robustness height model approaches agreement with the other models. Beyond ~18%, the meniscus would fail due to the force balance before sufficiently deflecting to touch any bottom surface, hence the over-prediction of robustness height. It is also worth noting that in calculating the hydrostatic force exerted on the air–water interface, Tuteja *et al*. (2008) used the minimum gap between the surfaces of the two fibers $2r^*$, instead of the distance between the fiber surfaces at the location where the interface is in contact with the fibers. This simplification can also affect the model's prediction, especially at high SVFs.

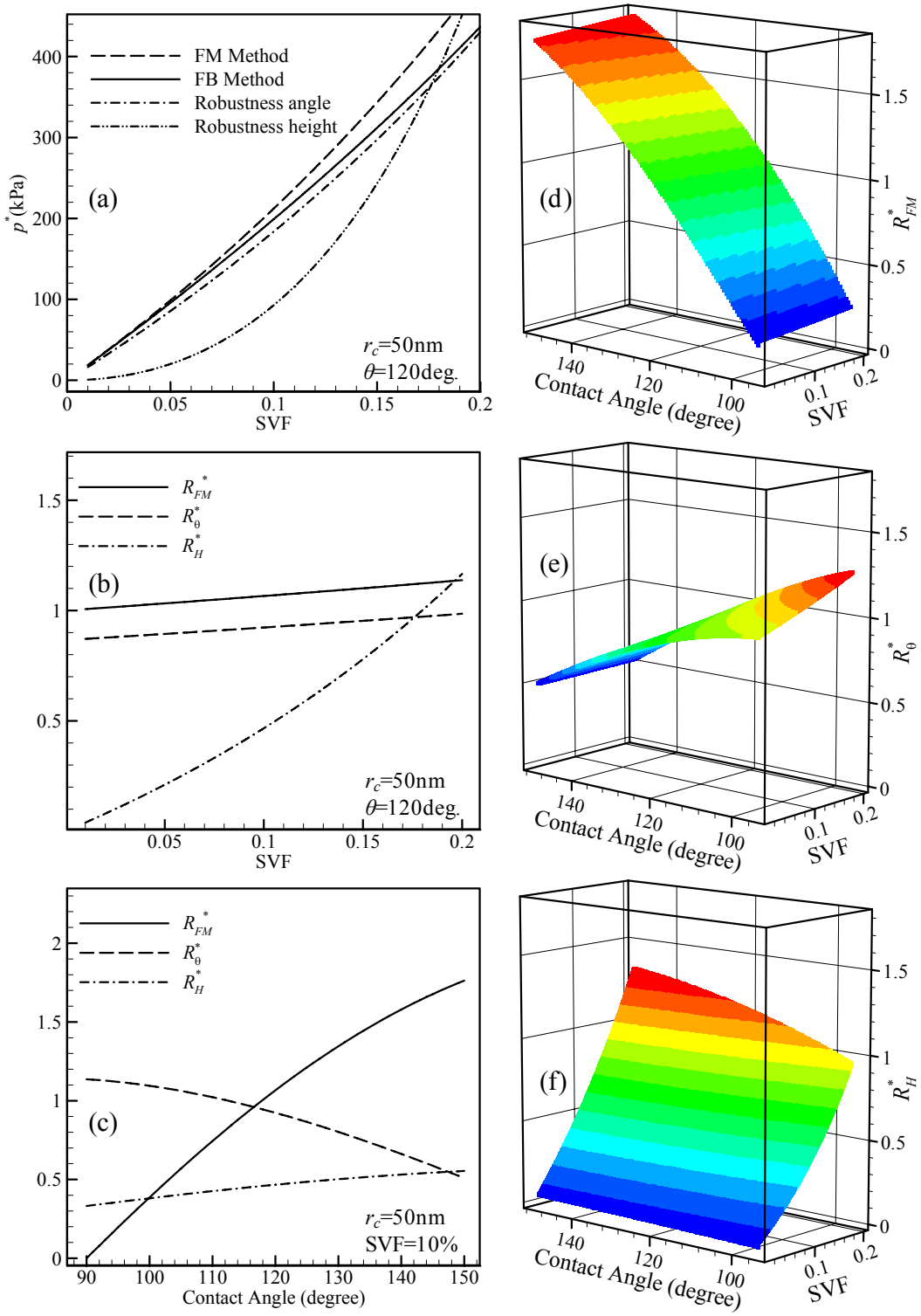

Figure 5.4: a) Critical pressure as a function of SVF using four different methods: Full Morphology (FM), our force balance (FB), and the robustness angle and robustness height method of Tuteja *et al*., (2008) (Equations 5.5, 5.6, 5.7, and 5.8, respectively). b) The ratios R^*_{FM}, R^*_θ, and R^*_H as a function of SVF. c) The ratios of R^*_{FM}, R^*_θ, and R^*_H as a function of contact angle. d–f) Surface contour plots of R^*_{FM}, R^*_θ, and R^*_H versus SVF and contact angle.

Beyond the simple case of parallel fibers with ordered in-plane arrangements (or vertical posts), no analytical method is available to predict the exact pressure at which the air–water interface failure takes place, leading to the departure of the surface from the Cassie state. Exact predictions of critical pressure require accurate predictions of the exact 3-D shape of the air–water interface over a superhydrophobic surface. The FM method (purely geometric in nature) is a powerful, yet approximate, method that can be employed for studying the role of microstructure on the resistance of a superhydrophobic surface with disordered 3-D fibrous structures against elevated pressures. This is especially true if the objective of the study is investigating the influence of each individual microstructural parameter on critical pressure, rather than the absolute values of the critical pressure itself, or the exact shape of the air–water interface. This method will be presented for orthogonal coatings in the next section.

Capillary pressure in a disordered fibrous coating is a function of microstructural parameters of a fibrous coating as follows:

$$p_c = f\left(\varepsilon, d_f, R_{cf}, n_c, T, \theta\right) \tag{5.9}$$

where R_{cf} is the diameter ratio between coarse and fine fibers, and T is the coating thickness. For the simulations conducted in domains with disordered fibrous structures, special care should be taken to ensure that the volume considered for the simulations is large enough to statistically represent a real fibrous coating, especially in the x- and y-directions, where symmetry boundary conditions are applied. Note that mirror-like symmetry boundary conditions (Neumann) are used in our FM simulations, with the constraint that the center of a sphere along a boundary must be inside the domain. To eliminate any artifact that can be caused by the choice of symmetry

boundary condition, one should consider simulation domains as large as computationally possible, or until no edge effect can be detected in the simulation results (Hosseini and Tafreshi, 2010; Ashari and Tafreshi, 2009). It should also be noted that for a specific domain size and SVF, the finer the fiber diameter, the higher the population of the fibers in the simulation domain. Increasing the population of the fibers improves the statistical reliability of the results. Nevertheless, with finite computational power, any simulations for a given set of parameters has to be repeated on an ensemble of different structures, statistically identical in terms of their structural properties (SVF, fiber diameter…), to ensure confidence and relevance in the data. The results presented in this section are averaged over an ensemble of no less than five structures.

Figure 5.5 shows a series of capillary pressure–saturation curves for a statistical ensemble of randomly oriented bimodal fibrous coatings with an SVF of 10%, coarse and fine fiber diameters of 500 nm and 100 nm, respectively, and a coarse fiber number fraction of 0.1. The trend observed in these curves is typical of such relationships in most porous media. At $p_c = 0$ (atmospheric pressure), the coating is fully saturated with air, or $S = 1$. As pressure is incrementally increased, water begins to penetrate, reducing the wetting-phase (air) saturation, but only as far as the most constrictive spaces in the coating for that given pressure allow (Equation 5.3). As pressure is further raised, the limiting pore size for intrusion becomes smaller, and water penetrates further into the coating. Eventually, pressure is sufficiently high such that the majority of the inter-fiber spaces can no longer constrict intrusion. Thus, saturation suddenly shifts to a lower value. From here, wetting-phase saturation approaches zero asymptotically with rising pressure, as water works its way into the smallest of the remaining pockets. Figures 5.5a and 5.5b illustrate the effect of the size of the simulation domain for cubical structures varying

by side length *s*. Figure 5.5b is a magnification of the region in Figure 5.5a in which coating failure is expected. As can be seen in Figure 5.5b, for a statistically homogeneous structure with constant microstructural parameters within the range of our study, predicted capillary pressure values are independent of domain size beyond a cubic side length of s = 10 μm. A side length of 24 μm is considered for the simulations reported here (with the exception of our thickness dependence study presented in association with Figure 5.7), to further minimize statistical errors.

Also of great importance for conducting FM simulations free of artifacts is that the resolution of the domains is adequate such that the spheres' interactions with the domain are not obscured by a poor choice of voxel size. In this regard, a group of fibrous structures was constructed with dimensions and parameters such that the exact same structure was built with five different voxel resolutions, with fine fiber diameter acting as the size reference. Figures 5.5c and 5.5d illustrate the results of this voxel-size test (5.5d is a magnification of 5.5c), with dependence negligible at voxel sizes of $0.33d_f$ or less. For the simulation results presented in this paper, we used a characteristic voxel length of $0.2d_f$.

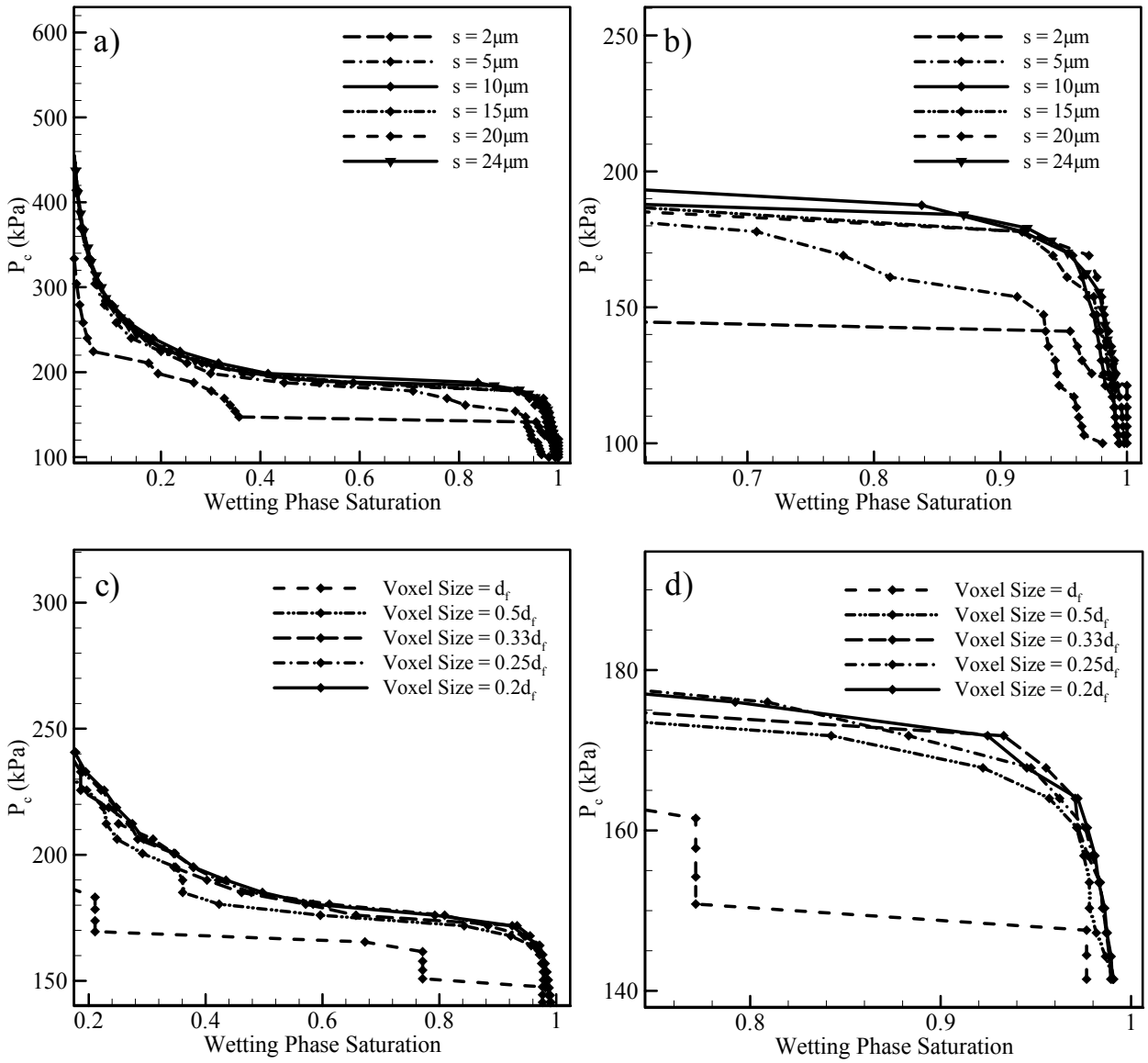

Figure 5.5: Capillary pressure–saturation curves for randomly oriented, layered structures. (a) and (b) vary only in the size of their domain (cubes of side length s); (c) and (d) vary only in their voxel resolution. Domain-size independence is acknowledged when breakthrough pressure, magnified for clarity in (b), no longer varies appreciably from one domain size to the next, taken as being greater than 10 μm. Voxel-size independence is acknowledged when critical pressure, magnified for clarity in (d), no longer varies appreciably from one voxel resolution to the next, taken as being when one voxel length is less than $0.33\,d_f$.

Table 5.1 comprises a list of default microstructure parameters for coatings with random and orthogonal fiber orientations (parameters not being varied for study will possess the values

shown in the table). Predictions for structures modeled after randomly laid electrospun fibers and those for orthogonal coatings are divided out for ease of presentation.

Table 5.1: Default coating microstructure properties used in our parameter study. Parameters not being varied for study will correspond to this table.

	Randomly Oriented	Orthogonally Oriented
Dimensions (μm)	24 24 24	24 24 24
Solid volume fraction (%)	10.0	11.2
Coarse fiber diameter (nm)	500	500
Fine fiber diameter (nm)	100	100
Coarse fiber number fraction	0.1	0.1
Surface tension (N/m)	0.07275	0.07275
Water contact angle (deg.)	120	120

Before elaborating on the results of our numerical simulations, it is important to establish a lucid definition for critical pressure, or failure pressure, in the context of our simulation method. To the knowledge of this student, there is no universal definition for critical pressure—the pressure above which the surface starts to depart from the Cassie state (whether or not it reaches the Wenzel state). Note that drag reduction due to superhydrophobicity is the result of water being in contact with a reduced solid surface area. We assume that drag reduction begins to diminish when water penetrates deep into the coating such that the first layer of the fibers is in the liquid phase. When this happens, the fibers in the first layer act like external objects resisting against flow. Figure 5.6 is an FM simulation of an oversimplified geometry to illustrate the above concept. Notice in Figures 5.6a and 5.6b that while the menisci dip between the fibers of

the first layer, the air–water interface still passes above these fibers, with Figure 5.6b being the threshold for critical pressure. Beyond the critical pressure (Figure 5.6c), the first layer is submerged, and the coating's drag reduction is diminished. Obviously, there is a possibility (especially for surfaces with random microstructures) that, due to non-uniformity in the coating's thickness, a stable air–water interface prevails, even if the interface is actually more than one fiber diameter into the material in some local areas. Thus, we define critical pressure based on the average water saturation over the entire coating corresponding to the value obtained by assuming that water is penetrated one fiber diameter deep into the medium.

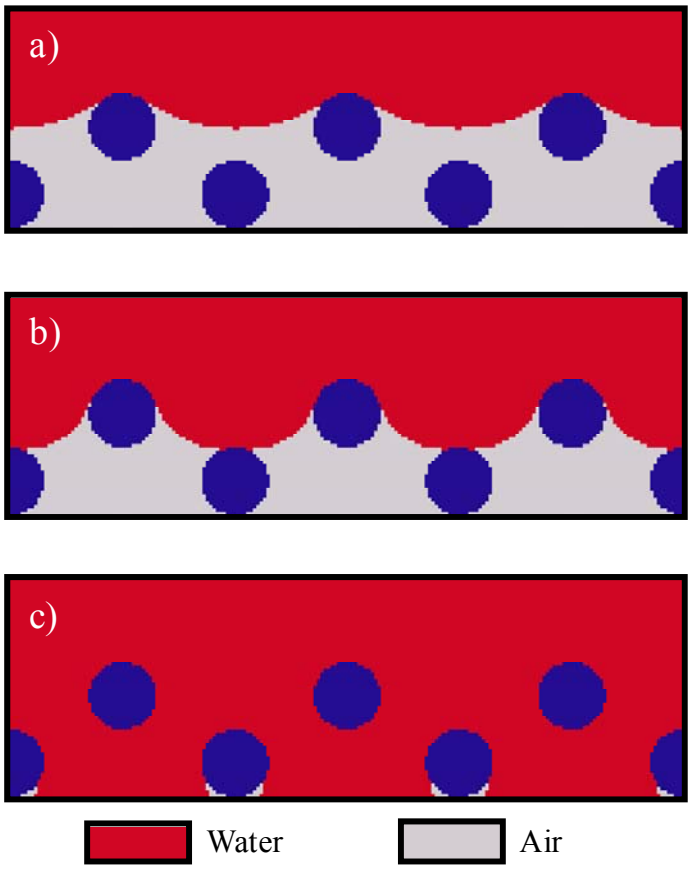

Figure 5.6: Conceptual illustration of different stages of water penetration into a coating surface, the dark region (red online) representing the intruding water front: a) water has not yet fully penetrated into the first layer, b) interface has reached the second layer, but has not yet submerged the first (critical pressure is the maximum pressure value for this condition), c) coating failure has occurred; the first layer of fibers is fully submerged.

Figures 5.7a and 5.7b illustrate a direct comparison between the performance of structures varying only in the orientation of their fibers, as well as their respective dependence on coating thickness. Note that the range of thickness considered for this study allows the domain size in the z-direction to be less than the constraint of $S = 10$ μm stated in association with Figure 5.5. However, the dimensions in the *x*- and *y*- directions are held constant at 24 μm while the z-direction is varied. As a result, the population and size distribution of the inter-fiber spaces in a given layer are not affected by the structure simply having fewer layers. The resulting curves are therefore free of the distortions characteristic of inadequate domain size that are visible in Figures 5.5a and 5.5b. For Figure 5.7a, the fibers are laid orthogonally. The high degree of order is reflected in the stepwise progression of fluid penetration, with critical pressure relatively independent of thickness. The pressure at which that first layer becomes submerged is the same for all the coatings shown. This is because the size of the spacing between the fibers does not vary significantly from one layer to the next, thus the first layer of fine fibers becomes the bottleneck for the coating. The difference in saturation for each curve is due to the first layer of a coating comprising different percentages of the domain for varying thickness. The stepwise fluid intrusion also allows for visual identification on the curve for the description applied in the above paragraph for critical pressure.

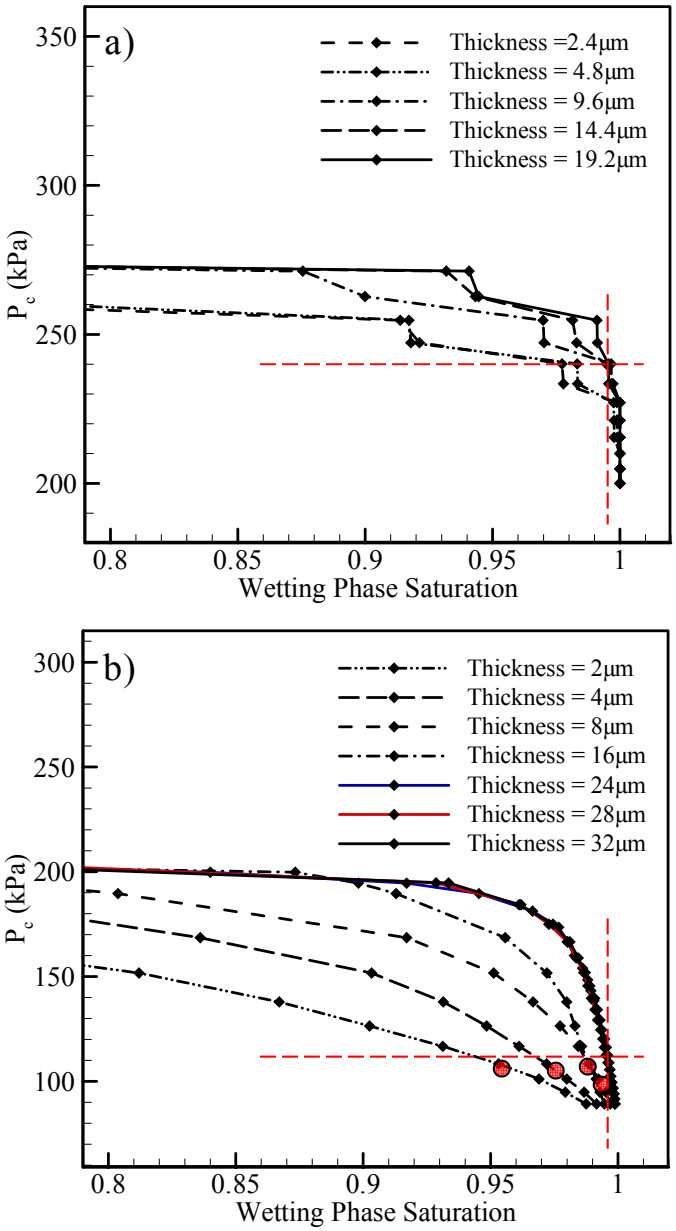

Figure 5.7: Capillary pressure–saturation curves for bimodal fibrous coatings of varying thickness comprised of: (a) orthogonally oriented fibers (SVF = 11.2%, d_f = 100 nm, R_{cf} = 3, n_c = 0.1), b) randomly oriented fibers (SVF = 10%, d_f = 100 nm, R_{cf} = 3, n_c = 0.1). The dotted cross through each plot is to better illustrate the p_c value taken as the critical pressure for the respective coating type, once thickness independence has been established. Shaded circles in (b) correspond to critical pressure determined for coatings not yet thickness-independent.

Figure 5.7b displays the capillary pressure–saturation relationship for coatings in which the fibers are randomly oriented. The broader size distribution of the void spaces in the case of

randomly laid fibers attributes to the shape of the curves in Figure 5.7b, depicting a smooth, continuous intrusion process as pressure rises, as was observed in Figure 5.5. A much greater dependence on thickness is also observed for capillary pressure in general, with dependence disappearing when the coating thickness is 24 μm or more, as the respective curves begin to fall on top of one another. Beyond this thickness, we can assume the coating to be homogeneous in the thickness direction for the microstructural parameters considered. As mentioned earlier, we establish our critical pressure definition for random fibers as being the pressure at which the first layer of fibers becomes submerged in water. In our simulations, we first obtain the minimum thickness required to produce a capillary pressure–saturation relationship independent of thickness (24 μm in the study reported here), and use this thickness for the remainder of our simulations. The saturation value corresponding to the first layer of the fibers in a 24-micron-thick coating being submerged (here 0.995), is then used to obtain the critical pressure for simulations conducted for coatings with different microstructural parameters. A vertical line is drawn for Figures 5.7a and 5.7b at this saturation level to accentuate the applicability of the clarity of the orthogonal coatings to the random.

We also investigated the effect of thickness on our defined critical pressure for the random-fiber coatings. The circles on the curves of Figure 5.7b represent the critical pressure values for the respective thicknesses corresponding to the equivalent saturation of a submerged first layer. The inconsistency in their behavior is explained by the size distribution of the inter-fiber spaces not being statistically consistent in coatings of such low thickness.

Randomly Oriented Fibers

This subsection presents the results of our parameter study for coatings with random in-plane fiber orientation. Figure 5.8 illustrates the dependence of critical pressure on each of the first four terms of Equation 5.9. For better illustration and the sake of brevity, we present only the critical pressure values themselves, plotted against the varied properties. Note that the scale shown along the y-axis is the same for all plots, making the relative effect of each parameter over the others more clearly visible. For Figure 5.8a, critical pressure increases with SVF. This result can be expected because, when all other microstructural parameters are held constant, a greater population of fibers in a given volume will result in smaller inter-fiber voids, thereby raising the necessary pressure to penetrate the coating.

For Figure 5.8b, coarse and fine fiber diameter are both varied, but the ratio between them remains constant, illustrating the general dependence of pressure on the fibers' size. Obviously, the smaller the fibers, the stronger will be the coating's resistance to hydrostatic pressure. In Figure 5.8c, the diameter of the fine fibers is held constant, while the diameter of the coarse fibers is varied, in order to establish the effect of the diameter difference between the fibers used in the coating. In both the cases of Figures 5.8b and 5.8c, smaller fibers in a given domain will require more fibers to be present for the same SVF and thickness. This in turn results in the spaces between the fibers being more constrictive, yielding a higher critical pressure for the medium.

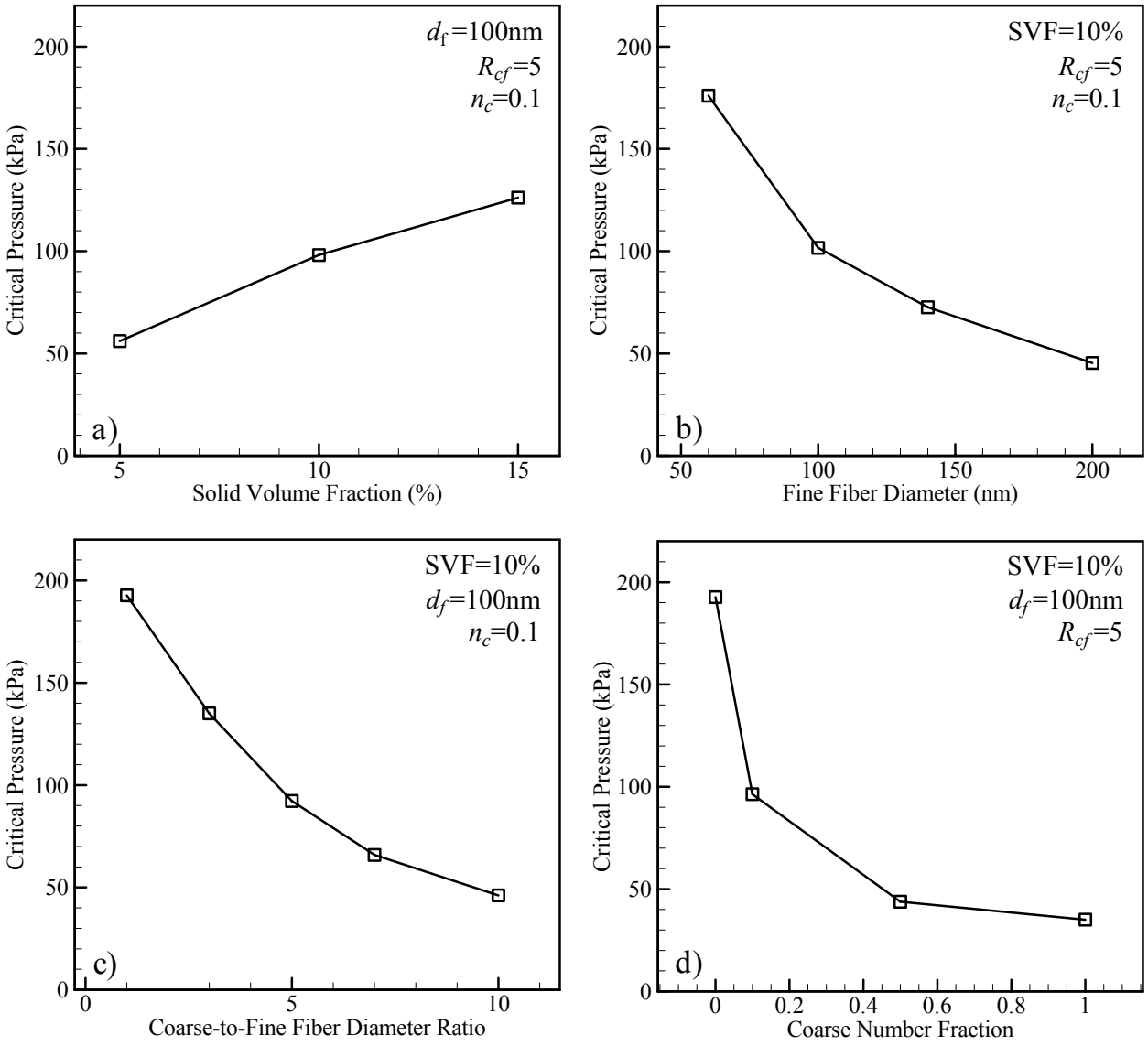

Figure 5.8: Critical pressure predictions for layered, randomly oriented electrospun media compared against variations in one of four microstructural parameters: (a) SVF, (b) fiber diameter (holding the diameter ratio between the two fiber sizes constant), (c) coarse-to-fine fiber diameter ratio (holding fine fiber diameter constant), and (d) coarse fiber number fraction.

Figure 5.8d illustrates the effect on pressure response when the coarse fibers comprise more of the population in the domain. As can be seen, even for a low n_c, such as 0.1, the critical pressure falls markedly with increasing n_c. This effect is accounted for by the same driving

principle as for Figures 5.8b and 5.8c. A larger population of coarse fibers causes more of the given solid volume to be consolidated into fewer fibers, thereby opening the bottlenecks in the medium that would otherwise restrict water intrusion. One may therefore be compelled to infer that a bimodal design would not be an optimal choice in a superhydrophobic coating. Note, however, that there are two mechanisms that cause a superhydrophobic surface to depart from the Cassie state: failure of the meniscus under excessive hydrostatic pressures (i.e., critical pressure), and dissolution of the entrapped air in water over time. The latter can be improved by storing more air in the pores of the coating. Without larger fibers running through the medium to encourage the presence of voids therein, a smaller reserve volume of air would be taken with the coating upon submergence, reducing its lifespan against dissolution of air into the surrounding water (Samaha *et al*., 2011).

Orthogonally Layered Fibers

As was mentioned earlier, the high degree of order in the orthogonally layered structures results in more uniform and constrictive spaces between the fibers, facilitating a significant rise in failure pressure for the coatings compared to their randomly oriented counterparts. However, this increased order also has several noteworthy effects on pressure dependence on other structural properties. An additional effect to take into consideration is the accuracy of the electrospinning apparatus in laying down evenly spaced fibers in a given layer (the motivation for implementing Equation 5.1 in our simulation methodology). Depending on how much the fibers in a layer are allowed to deviate from their would-be positions of even spacing in a structure of given properties, the bottleneck for water penetration into a coating may not be the first layer of fine fibers.

Figure 5.9 is an example illustrating this point for the case of a set of coatings with constant microstructural parameters, varying only in the magnitude of deviation permitted in fiber spacing. When fibers are perfectly uniformly spaced, the bottleneck will invariably be the first layer of the coating. When randomness in fiber spacing is permitted to a degree of half the solution of Equation 5.1, the most constrictive layer will still be one comprised of fine fibers, but it may not occur until the second layered pair of such fibers. When fiber spacing fluctuates according to Equation 5.1, the first layer comprised of coarse fibers may also begin to contribute to the bottleneck effect, hence the increased stepwise progression shown for such a case in Figure 5.9. Precisely at what levels of fluctuation the likelihood of the bottleneck begins to vary from one layer to another depends heavily on the fiber properties and populations for a given coating. Figure 5.9 illustrates only the example case of a coating with parameters typical of our structures, and no general trends across all coatings should be inferred. For the orthogonal coating results presented in this section, Equation 5.1 was used with upper limits placed on the magnitude of δ.

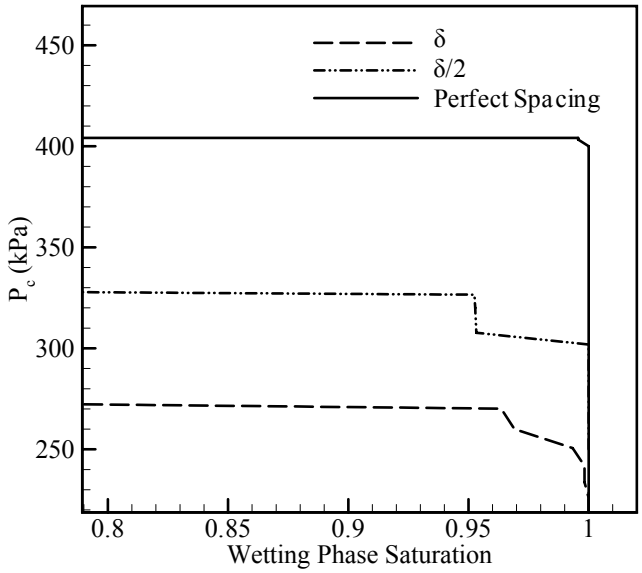

Figure 5.9: Example of capillary pressure–saturation curves for layered, orthogonally oriented structures with SVF = 11.2%, d_f = 100 nm, R_{cf} = 5, and n_c = 0.1. The structures vary only in the magnitude of each fiber's departure from 'perfectly ordered', even spacing within a layer (Equation 5.1).

Figure 5.10, like Figure 5.8, displays the effect of the first four parameters in the right hand side of Equation 5.9 on critical pressure, but for the case of orthogonal layers. In generating these structures, unlike our random geometries, the rigid order in fiber orientation necessitates a different approach in characterizing their microstructural properties, in which n_c and SVF are directly obtained based on number of fibers, as opposed to mass of fibers. Consequently, additional care was required to ensure that SVF would not vary more than one percent from its intended value as a result of the number of fibers in the domain. This was done by selecting the data points to be tested for one parameter or another such as to produce structures that could retain the prescribed SVF while adjusting the other parameters. Regarding the behavior of pressure for the orthogonal case, many of the plots demonstrate the same behavior as the random media, but at higher pressure values. The presentation of Figure 5.10d varies slightly from its random counterpart in Figure 5.8d, as it does not contain information for

n_c = 0 or 1. This is because, unlike the placement of fibers in our random media, which is inconsequential, fibers of different sizes are separated into layers, negating unimodal orthogonal structures for use as a direct comparison. Furthermore, no data is presented beyond n_c = 0.5. The reasoning for this is that in such a scenario, fine fibers would no longer form the more constrictive layers within the medium, and the overall relaxing of the bottleneck effect makes such a region of operation unappealing, as can be seen in Figures 5.10a, 5.10b, and 5.10c.

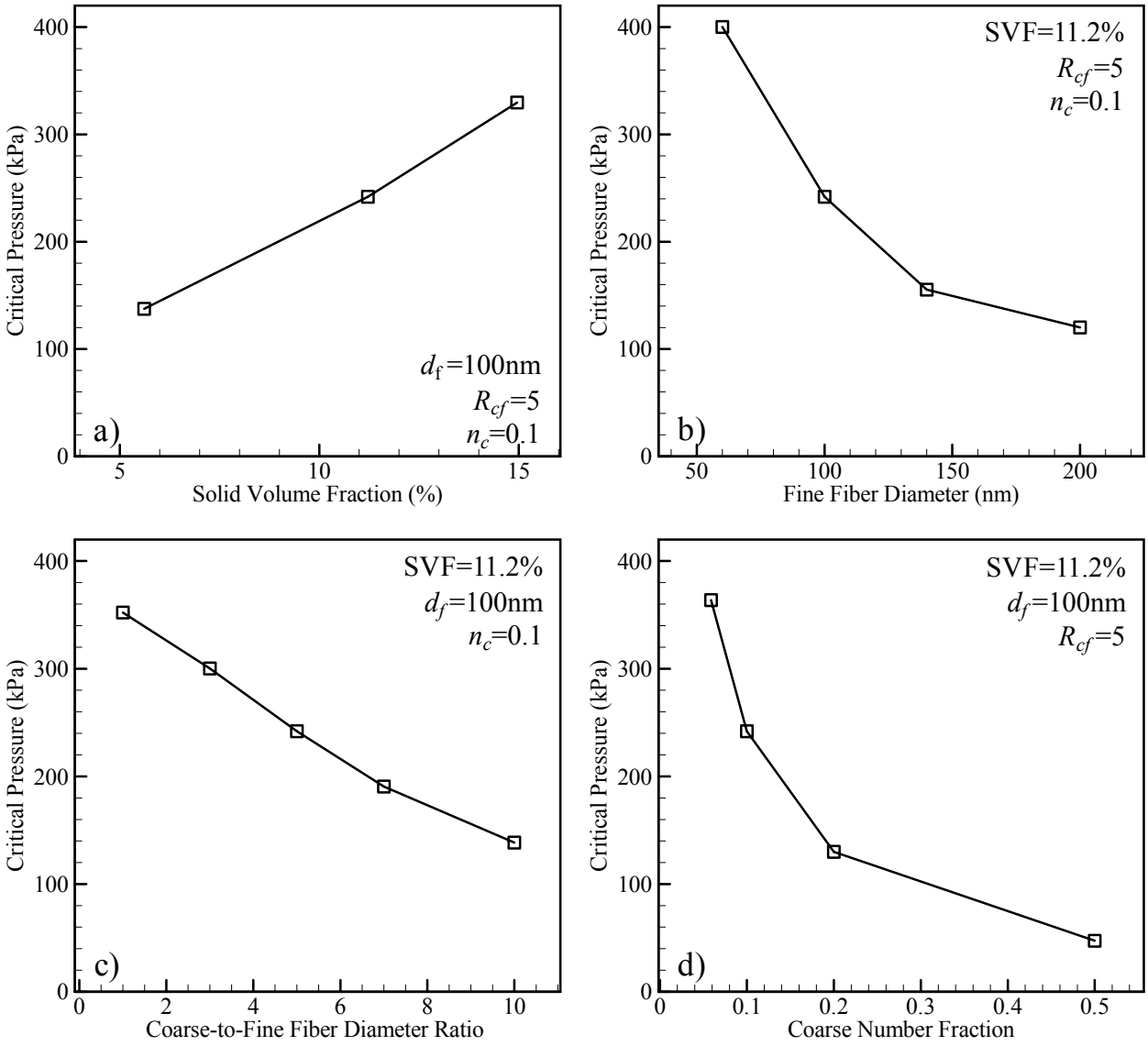

Figure 5.10: Critical pressure predictions for layered, orthogonally oriented electrospun media compared against variations in one of four microstructural parameters: (a) SVF, (b) fiber diameter (holding the diameter ratio between the two fiber sizes constant), (c) coarse-to-fine fiber diameter ratio (holding fine fiber diameter constant), and (d) coarse fiber number fraction.

Further Comparisons and Optimizations

It is worth mentioning that the orthogonally oriented bimodal structures examined thus far have been arranged such that two adjacent layers would consist of one fiber diameter, and the next two layers would consist of the other. As a result, both fiber diameters are oriented in both

directions. However, if fiber size were alternated with every layer, all fibers of a given diameter will face the same direction, with all fibers of the other size lying perpendicular to them. Such an arrangement is expected to cause a different distribution in the size and spacing of the inter-fiber voids. Furthermore, for a bimodal fibrous coating with constant microstructural characteristics, critical pressure may still vary based on which size fibers are laid as the outer layer.

Having established the performance characteristics of the different methods, it is possible to use different permutations in design to optimize a coating's performance and cost-effectiveness. To illustrate this, a numerical test was conducted on the performance of a hybrid bimodal structure representing an 8-micron-thick coating of orthogonal fibers layered on top of randomly oriented fibers, which are easier and less time consuming to produce than their orthogonally laid counterpart. Figure 5.11 illustrates the effectiveness of the orthogonal layer as a bottleneck for the entire coating. When the random layer is on the outer surface, the critical pressure for the coating is 95 kPa , whereas critical pressure is 252 kPa with the orthogonal layer on the surface. Regardless of which layer is on top, the resistance provided when the fluid interface front reaches the orthogonal layer is clearly distinguishable, as the dashed curve conforms to the solid curve. Such a coating illustrates how this process can utilize the advantages sought in both fabrication methods, providing an abundant reserve air inventory, as well as an elevated resistance to hydrostatic pressure.

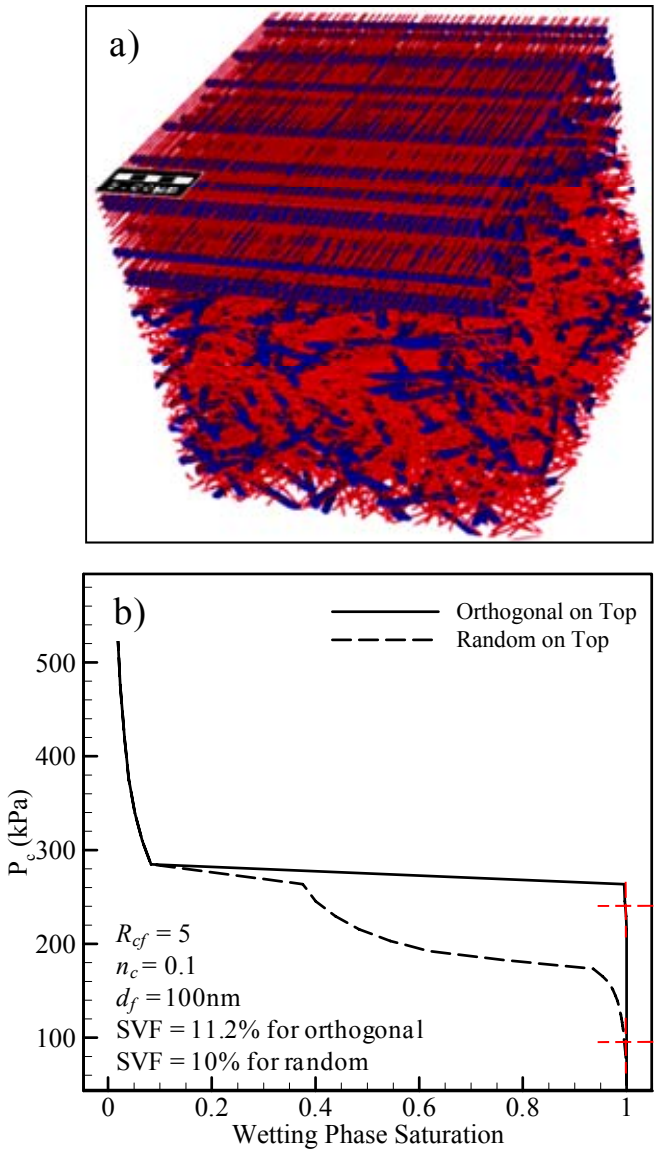

Figure 5.11: (a) An image of a hybrid coating, consisting of a 7.8-micron-thick layer of anisotropic-orthogonal fibers, and a 16.2-micron-thick layer of randomly oriented fibers, and (b) its capillary pressure–saturation curve, illustrating the difference in coating behavior depending on which layer is used as the top layer. The dashed crosses correspond to the critical pressure for each curve.

Our results show that for structures with the same solid volume fraction, coarse and fine fiber diameter, and coarse fiber population, varying only in the orientation of their fibers, the parametric controllability of orthogonally oriented coatings produced yields significantly higher resistance to water intrusion, due to their more ordered pore structure. The influence of the

particulars of a coating's microstructure is such that, from the perspective of pressure tolerance, a lower volume of empty space—and more constrictive spaces where they exist—is advantageous. Our results show that this is best achieved through the production of coatings with comparatively low porosity, comprised predominantly, if not exclusively, of smaller fibers. However, more and larger inter-fiber gaps are still desirable for maintaining a reserve air volume for coating longevity. In the next section, we will compare our Full Morphology results for orthogonal coatings with the surface energy minimization method first laid out in Section 3.1. This method will also be expanded so that coatings with multiple fiber wettabilities can be considered.

5.2 Critical Pressure via Minimizing Interface Energy

In this thesis, we also develop a numerical strategy for modeling the fluid interface in orthogonally laid fiber coatings by solving for the minimum-energy shape of the meniscus using the Surface Evolver code, as introduced in Section 3.1 (Brakke, 1996; Brakke and Morgan, 2002). A conceptualization of our computational domain is shown in Figure 5.12a, representing a cell from a coating comprised of orthogonally layered fibers. The domain consists of only four layers, but in actuality a coating could consist of any number of layers. However, in the unit cell study in this work, only the first four layers are required, as a fluid interface could not penetrate more deeply unless the meniscus de-pins from the first layer, fully wetting it (i.e., water has penetrated the coating). The domain has symmetry boundary conditions around the outer fibers, as shown in Figure 5.12b. The fibers are color-coded by layer for illustration, with the first, second, third, and fourth layers being light blue, light red, dark blue, and dark red respectively. s represents the center-to-center spacing between adjacent fibers in the same layer, as in previous chapters. The layers have a staggered pattern, in order to better characterize the spaces through

which a meniscus would penetrate the coating, as it is very unlikely that fibers of one layer would be directly beneath the fibers two layers up.

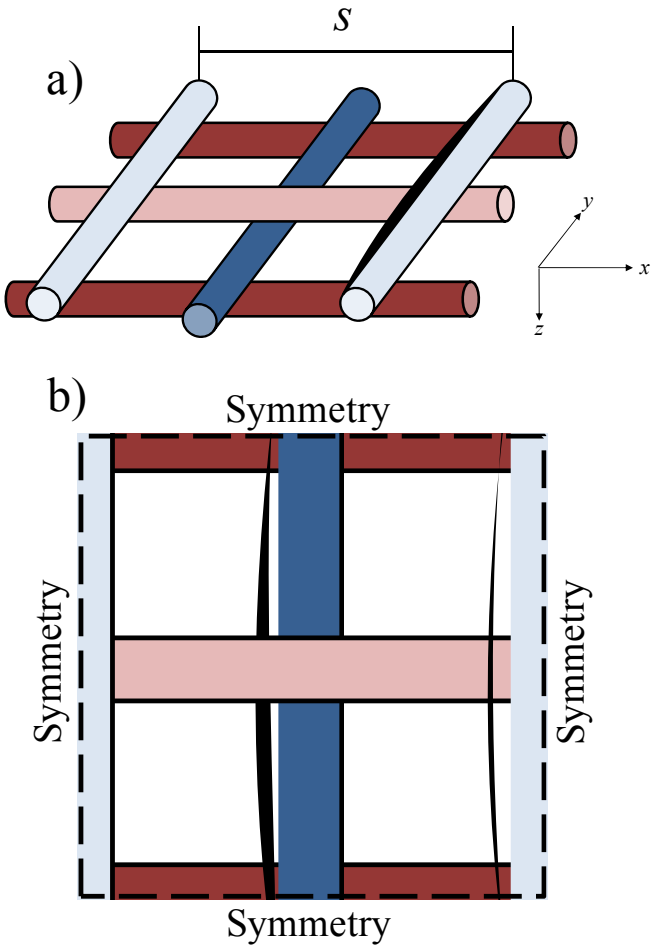

Figure 5.12: (a) Visualization of a region of an orthogonally layered electrospun fiber coating. Four layers are modeled, and colored light blue, light red, dark blue, and dark red progressing into the coating. (b) Overhead view of the simulation domain as a meniscus would penetrate in. Symmetry boundaries outline the domain.

The Surface Evolver code is able to solve for the minimum-energy shape for a closed volume such as a droplet on an arbitrary solid surface, or in our case, for an open interface

between one fluid above and another below. The general form of the energy equation being integrated in the code can be expressed as (de Gennes *et al*., 2004)

$$E_s = p\iiint dV - \sum \sigma \cos\theta_i \iint dA_i \tag{5.10}$$

where p is the applied pressure difference across the interface. Like the FlexPDE software in Section 3.1, the Surface Evolver code solves Equation 5.10 using the gradient descent method. This pressure difference could be due to the hydrostatic pressure imposed on a submerged superhydrophobic coating, or the pressure drop across a submerged filter coating. The summation refers to the energy contributed by the water-contact area of each fiber associated with the interface. To ensure proper calculation of the fibers' energy contribution, the integrand dA_i must be derived for each fiber and applied explicitly in the code. Figure 5.13a is a visualization of the appropriate wetted-area element for a fiber in a coating (the length of the fiber is aligned in the x-direction). The positive z-direction is down into the coating with $z = 0$ at the top, and the air–water interface is symmetrically draped over the top of the fiber, pinned at angle α from the top of the fiber. dA for the fiber is thus derived as

$$dA = 2r_f \alpha dx \tag{5.11}$$

where through geometry

$$\alpha = \cos^{-1}\left(1 - Z / r_f\right) \tag{5.12}$$

and

$$Z = z - 2nr_f \tag{5.13}$$

with n being equal to the number of layers above the given fiber ($n = 0$ for the first layer). If the fiber is oriented in the y-direction, then Equation 5.11 is integrated with respect to y instead of x.

A modification must also be made in the code for the calculation of the volume integral in Equation 5.10. Figure 5.13b is given to help explain this, showing a cross section of a fiber and meniscus intersecting at point A, at an angle α from the top. Without any correction, the contact line represented in 2-D by point A would be projected in a straight line to the *xy*-plane, ignoring the overlapping fiber and the excess water above the fiber. To compensate for this, we write an additional volume integrand along each fiber boundary. Three geometric regions are drawn with the fiber in Figure 5.13b: an overlapping circular sector and trapezoid (regions I and II, respectively), and a rectangle above the fiber (region III). Our user-defined volume integrand is obtained by subtracting the area of region I, and adding the area of regions II and III (area occupied by both regions I and II cancel). Using the convention of Equations 5.12 and 5.13, we have

$$dV = -\frac{r_f^2 \alpha}{2} + \left(\frac{Z + r_f}{2} + 2nr_f \right) r_f \sin\alpha dx \tag{5.14}$$

Again, Equation 5.14 is integrated with respect to *y* if the fiber is oriented in the *y*-direction.

Thus for a given pressure the Surface Evolver code, enhanced with Equations 5.11 and 5.14, solves for the minimum-energy shape of the air–water interface, reporting back the volume, meniscus depth, and wetted surface area of the fibers in contact with the water.

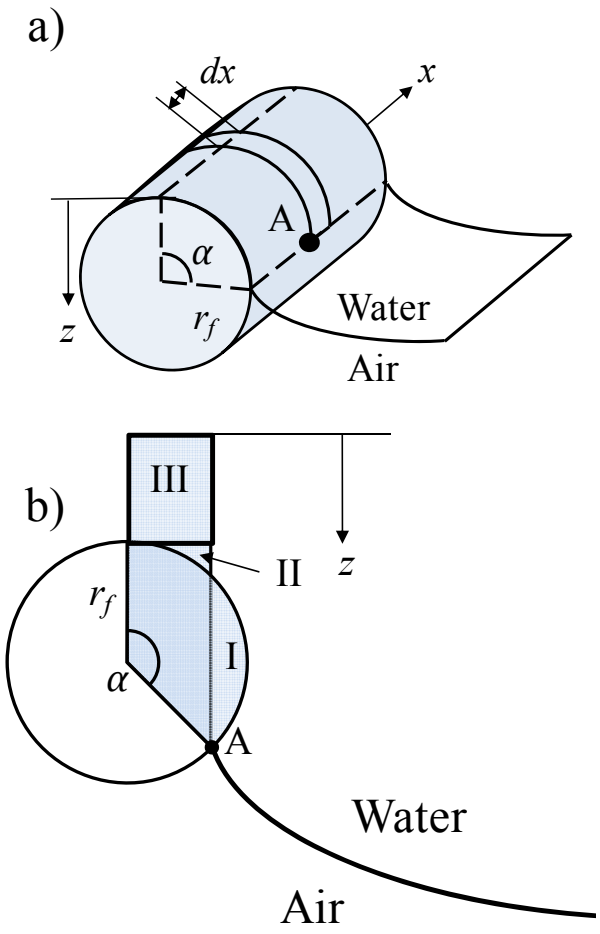

Figure 5.13: (a) Illustration of the energy contribution of a fiber as water comes into contact with it. Wetted surface area as a function of *z* is explicitly derived and coded into the model. (b) Illustration of the volume of a fiber and additional water that must be accounted for in the model. Region I is deleted from the volume calculation. Regions II and III are added. Volume as a function of *z* is explicitly derived and coded into the model.

Failure Criteria and Mesh Independence

Figure 5.14a is a sample of the initial setup of the simulation domain. The coating has a solid volume fraction (SVF) of 10% and a fiber diameter of 10 μm. The red and blue fibers have a water contact angle of 130° and 100°, respectively. The initial setup has the meniscus in contact with all the associated fibers from the beginning of the simulation. The same set of parameters could also be initiated with the meniscus in contact with fewer layers, (indeed, some

actually require fewer layers), resolving the interface shape would reveal that the meniscus dips sufficiently so as to make contact with additional layers. Since boundary and contact conditions in our model cannot be added or removed once a simulation has begun, the correct number of layers for given conditions must be established before collecting data. Figure 5.14b shows a typical simulation result. As can be seen, the mesh has been refined accordingly, and at the given pressure of 4.60 kPa the water–air interface has deflected sufficiently so as to be in contact with four fiber layers without breaking off from the first layer.

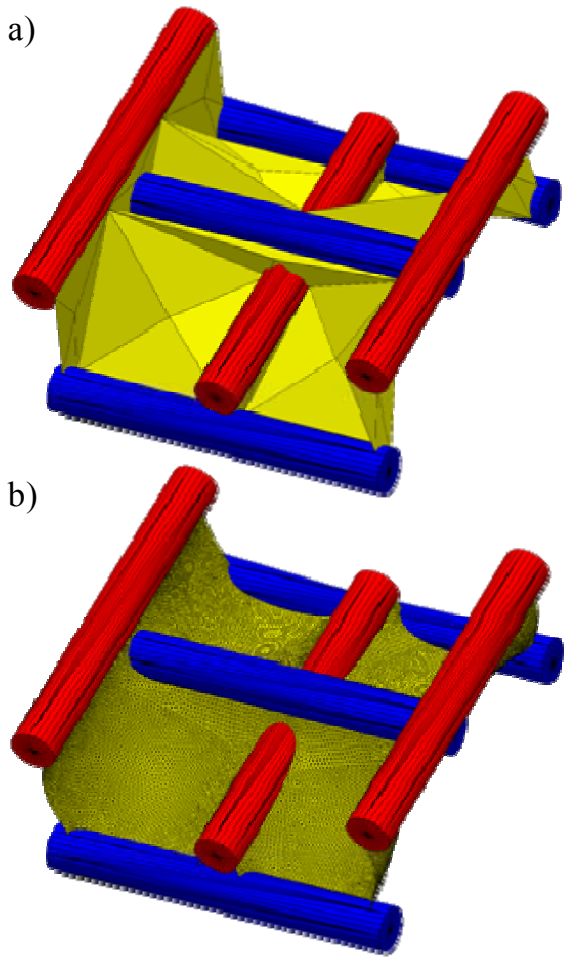

Figure 5.14: (a) Sample simulation domain in its initial condition before solving. (b) Simulation domain after refining mesh density and solving for the minimum energy shape and wetted area.

In general, a superhydrophobic coating is regarded to have failed under hydrostatic pressure when the applied pressure is sufficiently high to overtake the capillary resistance of the coating. For simple cases, such as a single row of parallel fibers, the critical pressure can be derived analytically. Figure 5.15a shows a free body diagram of the balance of forces across a between two fibers at an arbitrary pressure p. The equation for this is given here as

$$p_{FB} = -\frac{\sigma \sin(\theta + \alpha)}{s/2 - r_f \sin\alpha} \tag{5.15}$$

This equation calls back to Equation 3.15 from earlier, and is indeed the same equation, but derived for a single contact angle in the context of hydrophobic applications instead of hydrophilic. Such analytical expressions were also studied in Tuteja *et al*. (2008), among others. Determining the critical pressure is a matter of differentiating Equation 5.15 with respect to α setting it equal to zero, and solving for the critical angle α^* that would result in critical pressure when substituted back into Equation 5.15. Thus, critical pressure p^* across a bank of parallel fibers, expressed in terms of SVF ($s = \pi r_f / 2\varepsilon$), where ε is equal to SVF, becomes

$$p^*_{FB} = -\frac{\sigma \sin(\theta + \alpha^*)}{r_f(\pi/(4\varepsilon) - \sin\alpha^*)} \tag{5.16}$$

When additional layers are added, such as in orthogonally layered coatings, the capillary resistance of the coating becomes stronger, and the interface occupies different amounts of surface area on each fiber layer with which it is in contact. Thus, the system becomes more difficult to characterize analytically. This is compounded by another issue. For a single set of parallel fibers as in Figure 5.15a, critical pressure represents a physical limitation of the system to accommodate a higher hydrostatic pressure without breaking outright. Our models show that a meniscus that straddles across three or four layers of orthogonal fibers never reaches such a

mechanical breaking point before the meniscus itself deflects laterally so as to meet itself across the symmetry boundary. At this point, in a physical system, the meniscus would coalesce with itself and break away from the first layer of fibers, neutralizing the superhydrophobic characteristics of the coating by submerging the first layer. We therefore define the failure pressure in our simulations as the pressure just before this coalescing condition is reached. Figure 5.15b shows the same coating and meniscus from Figure 5.14b, but from a view that illustrates the failure condition. Raising pressure 1–10 Pa higher would result in failure, as the model itself would also show, as it diverges in such a case. Litster *et al*. (2006) suggested that the critical pressure a fluid interface passing through an orthogonally oriented coating could be analytically approximated using a modified Young–Laplace equation:

$$p_{Lit}^{*} = \frac{2\sigma\cos\theta}{s - d_f} \tag{5.17}$$

where the gap is essentially treated as a capillary radius of sorts. We compared equation *10 with our model and with the force balance equation for parallel fibers above (5.16) for a coating with an SVF of 10%, fiber diameter of 10 μm, and a contact angle of 120°. The two analytic expressions agreed well with one another, with Equations 5.16 and 5.17 giving pressures of 1.99 kPa and 2.12 kPa, respectively, while modeling the system directly with the failure criterion shown in Figure 4b resulted in a critical pressure value of 4.8 kPa, more than twice that of the analytical approximations. Recall, however, that fiber placement in a layer is staggered in relation to fibers two layers down. If one uses a value of $L_f/2$ in Equation 5.17 to approximate the staggered layering, then the agreement of Equation *10 becomes much better, with a critical pressure of 4.97 kPa.

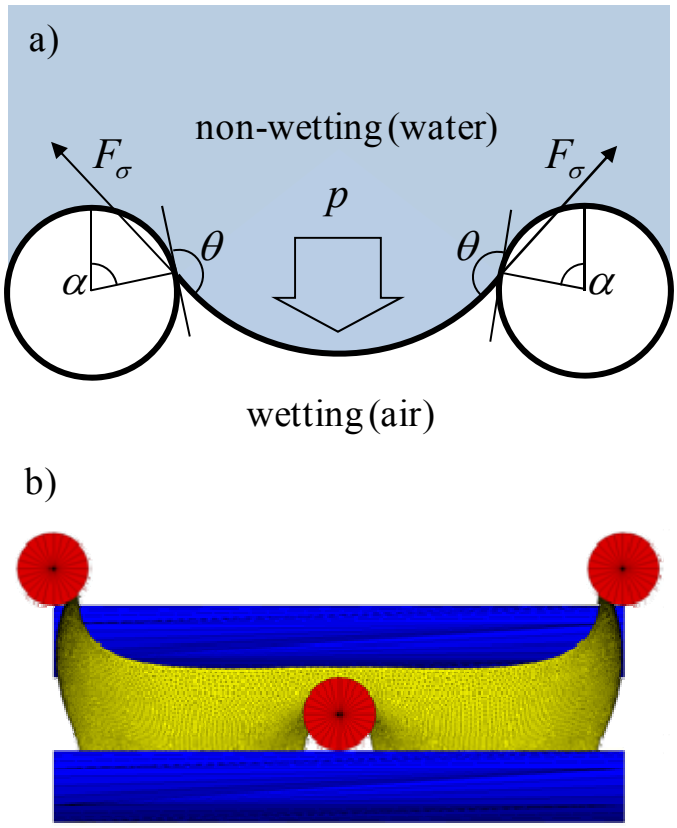

Figure 5.15: (a) Free body diagram of the balance of forces across the meniscus between two parallels fibers. (b) Side view of the air–water meniscus spread across four layers. Meniscus (yellow) illustrates the failure criterion on which this section bases critical pressure. Beyond the given pressure, it will swell across the symmetry boundary and water will fully envelop the first layer.

Having established our criterion for failure for a coating, a criterion must also be established for the minimum mesh density required for a numerically accurate solution. A uniform mesh is applied over the whole interface with triangular elements. To establish mesh size independence, we examined a structure with the same SVF and fiber diameter as in Figure 5.14, but with a contact angle of 120° assigned to all fibers. In Figure 5.16 the resulting interface for an applied pressure of 4.80 kPa (p^* for this configuration) is shown in the inset, with the dimensions w and h for meniscus width and depth. The fibers are omitted from the image for clarity. The plot itself for Figure 5.16 shows the resulting effect on w and h as a function of mesh density. As can be seen, the change is negligible, with less than a 1% difference from the

coarsest mesh to the finest. However, while mesh dependence is not an issue for the correct interface shape, structures with a higher fiber count result in smaller clearances for the meniscus to occupy where fibers intersect. This can result in skewed elements that affect model stability. A minimum mesh density of eight grid points per fiber radius is sufficient to prevent this for all parameters tested.

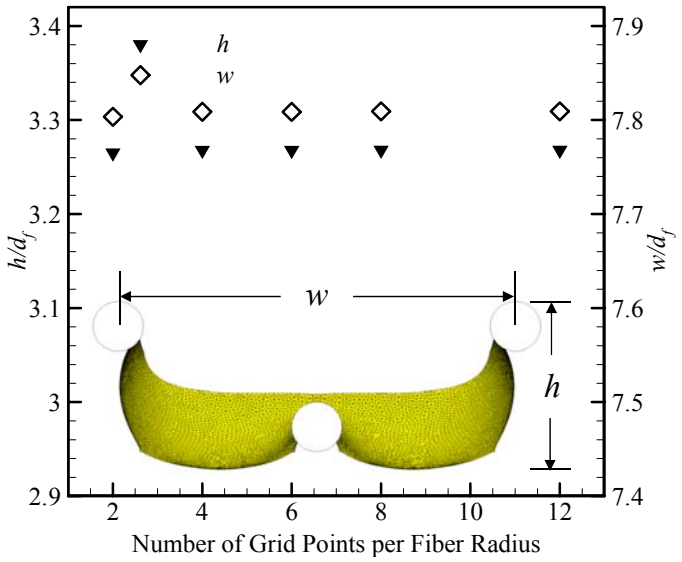

Figure 5.16: *h* and *w* normalized with fiber diameter as a function of number of grid points for fiber radius. The inset image shows a sample interface at the coating's critical pressure. Fibers are made invisible for visualization. Dimensions *h* and *w* are measured for mesh independence study.

Relations to Expand Applicability

The results presented in this section examine the effect of various coating microstructure parameters on the critical pressure, wetted area fraction, and meniscus depth for each given case. Most of the simulations performed for the results shown involved structures with a fiber diameter of 10 μm. However, the ordered nature of the coatings being studied results in a convenient property for the data presented. Figure 5.17 shows a collection of results for p^* over an SVF

range of 5% to 15% for square arrays with a contact angle of 120°. Three fiber diameters are simulated: 5 μm, 10 μm, and 15 μm. As can be seen in the figure, the pressure values have a clear linear relationship that shows perfectly—e.g., coatings with fibers three times smaller have a critical pressure three times higher for the same SVF. The relationship between critical pressure results is equal to the inverse of the relationship between the chosen fiber diameters:

$$\frac{p_2^*}{p_1^*} = \frac{d_1}{d_2} \tag{5.18}$$

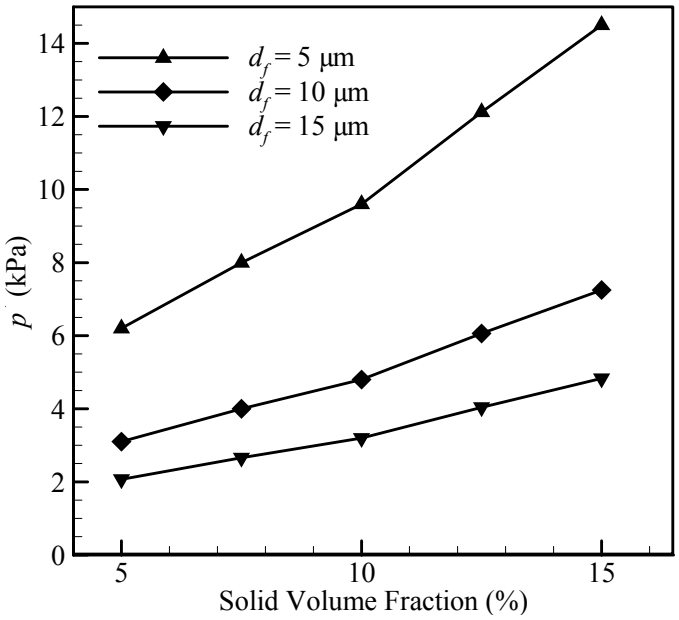

Figure 5.17: Critical pressure as a function of SVF for three different set of coatings varying by fiber diameter. All coatings have a contact angle of 120°.

This relationship is consistent with that given analytically in Equations 5.16 and 5.17 above. These coatings are layers of parallel fibers stacked on top of one another. While p^* itself is no longer as easily calculated, the linear inverse relationship between p^* and fiber diameter still holds. This means that, while are results are reported on the order of 10 μm, they can be

scaled to any order of magnitude in which assumptions regarding continuum and surface tension forces etc. still apply. Along with critical pressure in this work, we will also report wetted area fraction A_w (dimensionless). The nature of this value makes it independent of fiber diameter and therefore also consistently applicable across any size scale.

A second relationship to point out is that, given that results are scalable to different length scales (i.e., fiber diameters), it is convenient to display results based on solid volume fraction (SVF) of the coatings and their layers. This SVF property and the observed trends that accompany it are consistent across all length scales, whereas other more experimentally convenient systems of measurement such as fiber count and fiber spacing are not. Converting from SVF ε to fiber spacing s can be derived geometrically as

$$s = \frac{\pi d}{4\varepsilon} \tag{5.19}$$

and fiber count is just the inverse of fiber spacing (adjusting from microns to millimeters if needed, of course).

Effect of SVF and Contact Angle

Coating failure typically occurs in one of two cases, depending primarily on fiber spacing. Figures 5.18a and b illustrate these modes for coatings comprised 10-μm fibers and a contact angle of 120°. The first is illustrated in Figure 5.18a, in which the meniscus is fully in contact with the first four layers of the coating, as the established failure criterion for the coating (the meniscus laterally swelling to just before the symmetry boundary) is reached before the meniscus comes into contact with the fifth layer. Fiber coatings with lower SVFs (higher

spacing), regardless of size or hydrophobicity, exhibit the failure shown in Figure 5.18a. The condition shown in Figure 5.18b typically applies to coatings with an SVF of 12.5% or greater. It corresponds to the stable meniscus coming into contact only with the first three layers of the coating before reaching the symmetry boundary. There is also the rare case where failure is taken as the pressure just before the meniscus contacts the fourth layer, having only reached three layers in depth. This is because at the given spacing, the introduction of the fourth layer actually reduces the coating's overall capillary resistance against the interface in this case. Simulating such an interface to investigate our failure criterion with four layers or only three layers shows that p^* is actually lower for an interface in contact with four layers than it is for three. This means, in reality, the coating will fail as soon as the interface touches the fourth layer of fibers without first reaching the stable configuration from Figure 5.18a. This failure mode has been observed to happen for only one case in the data to follow, and had an SVF of 12.5% and contact-angle pairing of 130° for odd layers and 100° for even layers (shown in Figure 5.20).

Figure 5.18c shows the corresponding critical pressure for fibrous coatings with a fiber diameter of 10 μm and a contact angle of 120°. The coatings are arranged in a square array, with fiber spacing the same for layers oriented in the *x*- or *y*-direction. As can be seen, critical pressure rises in a relatively linear fashion as SVF increases. This linear rise is in spite of the number of layers in contact with the meniscus. The interface is in contact with four layers for data points in the white region of the plot, and with only three layers for the gray region (region is for visualization and not intended to imply boundaries) In Figure 5.18e, the solid points show the behavior of wetted area fraction A_w of the coating, where $A_w = 1$ is equal to the surface area of the substrate as if the coating were not applied. It can be seen that, while a more tightly

packed coating has a higher critical pressure for a given fiber size and contact angle, the desired slip effect would only amount to behavior fitting of a superhydrophobic coating if the solid–water contact area is sufficiently less than it otherwise would be. A_w, however, is independent of fiber size, and since critical pressure is observed to vary linearly with fiber diameter, a higher desired critical pressure can be achieved by using smaller fibers.

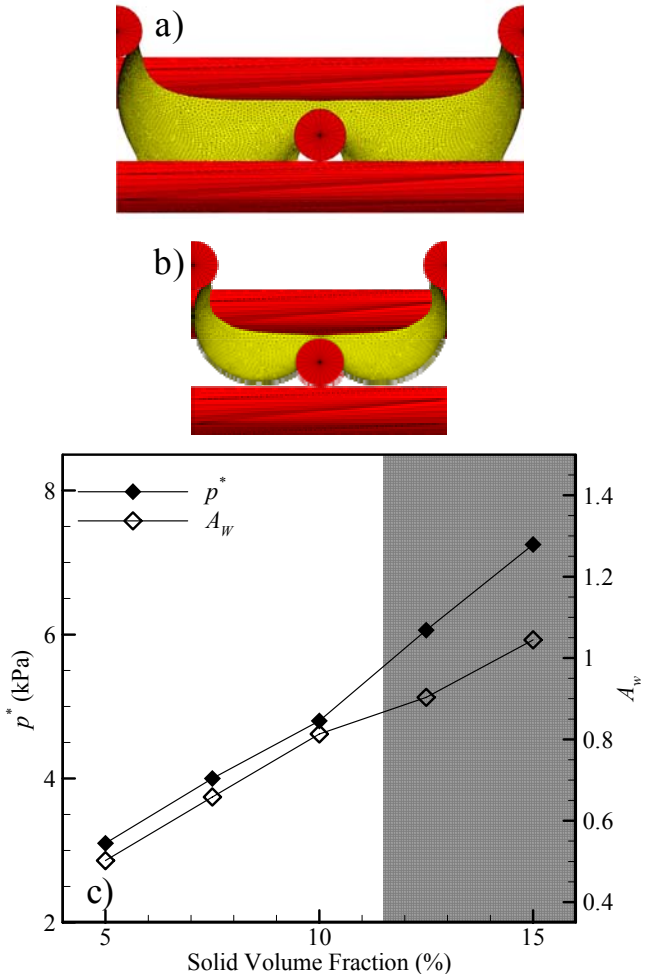

Figure 5.18: (a) Meniscus is four layers deep before meeting symmetry boundary. (c) Meniscus is only three layers deep before meeting symmetry boundary. (c) Critical pressure and wetted area fraction as a function of SVF for fibers with equal spacing on all layers (white and gray regions represent failure over four or three layers, respectively).

The inset image in Figure 5.19a shows an illustration of two different fiber coatings with the same fiber spacing and size. The red structure has a contact angle of 100°, and the blue 130°. Both structures have been subjected to their respective critical pressures. It can be seen that the meniscus for the more hydrophobic structure has a tighter curvature than the other, corresponding to its higher critical pressure. The increased hydrophobicity of the blue structure is also observed to have a lower wetted surface area, whereas more of the meniscus is draped over the fibers of the red structure. Figures 5.19b shows the effect of varying contact angle on critical pressure. Coatings are kept at an SVF of 10% and a fiber diameter of 10 μm. It can be observed that critical pressure rises as water contact angle increases. And in Figure 5.19b, it can be seen that wetted area fraction A_w drops with increasing contact angle, which is consistent with the contrasting menisci in Figure 5.19a, and would result in improved slip performance.

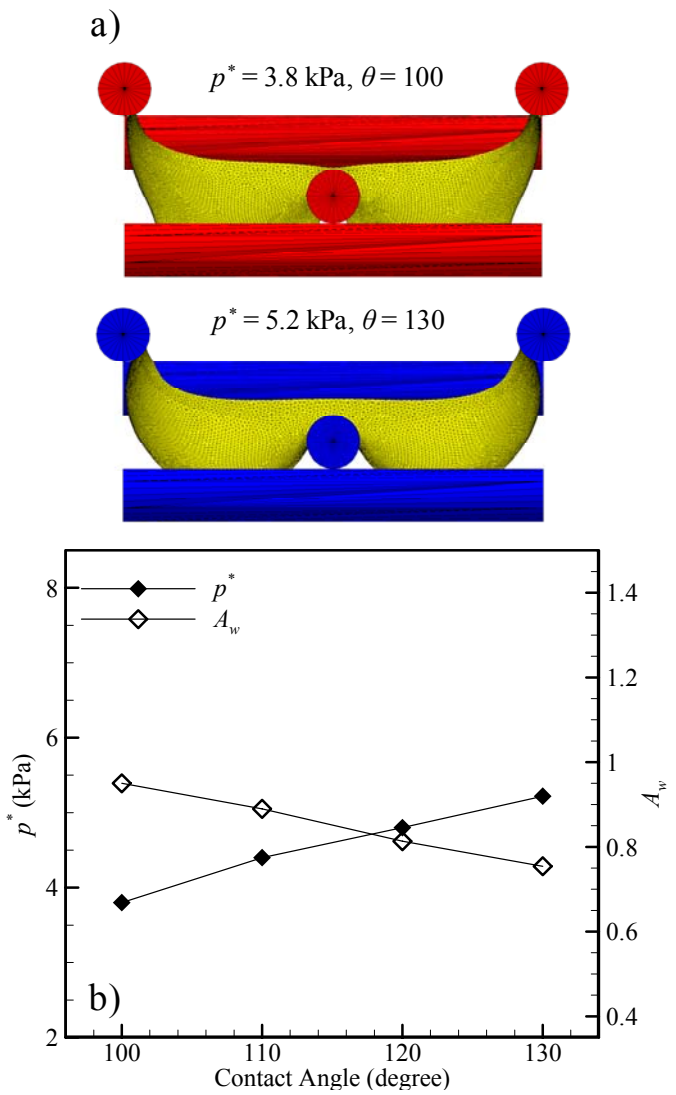

Figure 5.19: (a) Two fibrous coatings with an SVF of 10% and a fiber diameter of 10 μm. The red fibers have a water contact angle is 100°, and the blue fibers have a water contact angle is 130°. (a) Critical pressure and wetted area fraction as a function of contact angle for fibers with equal spacing on all layers. (c) Critical pressure and meniscus depth as a function of contact angle for fibers with equal spacing on all layers.

Finally, we tested the effect of alternating layers in the coating having different contact angles. We modeled an additional series of coatings with equal spacing for all layers. Fiber layers have a contact angle of either 100° or 130° (with 130° being more hydrophobic). Figures 5.20a and 5.20b show the critical pressure while varying SVF for the arrays, alternating which of

the two fiber types is in the even or odd numbered layers. The variation in critical pressure between cases is minimal, as is A_w.

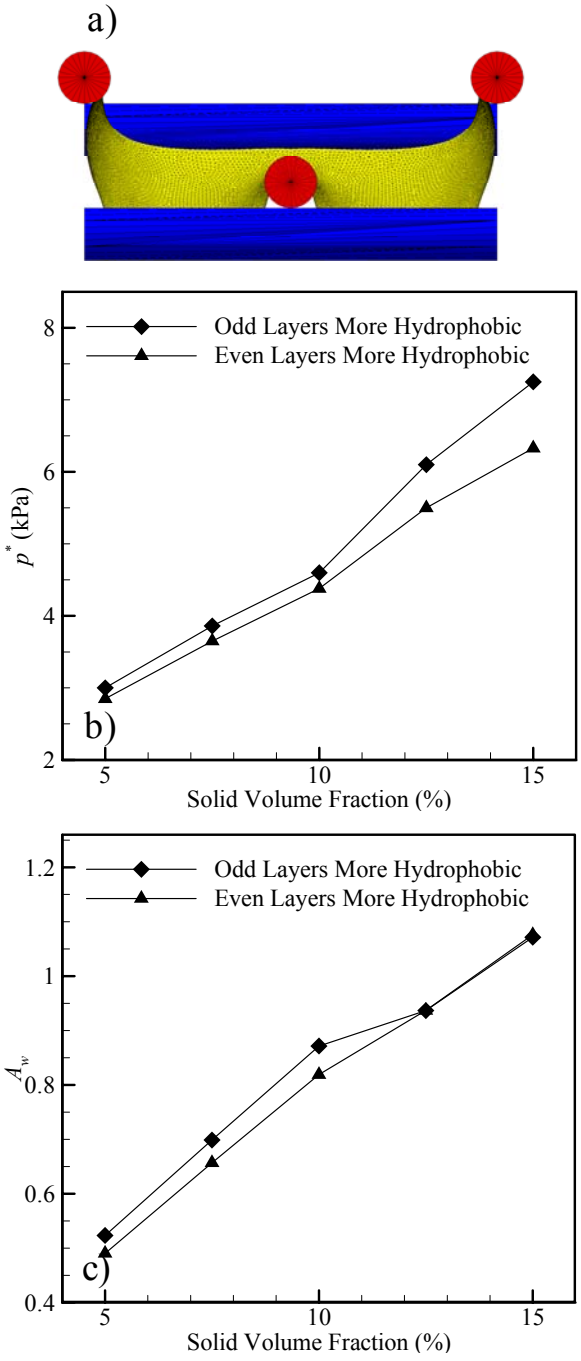

Figure 5.20: (a) Critical pressure and wetted area fraction as a function of SVF for coatings alternating contact angles. The alternating layers have contact angles of 130° and 100°. (b) Critical pressure and meniscus depth as a function of SVF for coatings alternating contact angles.

5.3 Orthogonally Layered Coatings for Improved Aerosol Filtration

This last section will quickly review the extension of orthogonally laid electrospun fiber coatings to filtering aerosol particles from the air. The most common method of removing particles from a fluid stream is via fibrous filters which are generally characterized by two basic parameters: collection efficiency and pressure drop (Brown, 1993; Spurny, 1998; Tien, 2012). Generally speaking, nanofiber media cannot be used as a stand-alone filter due to their lack of mechanical strength. However, they can be used as a thin coating deposited on the front and/or back surface (upstream and/or downstream side) of a filter medium comprised of larger fibers, to enhance its overall performance (see e.g., Podgorski *et al*., 2006; Zhang *et al*., 2010).

Flow Field and Particle Capture Equations

In the Stokes flow regime, pressure drop across a filter is caused by viscous forces as air flows past the fibers. The flow field through a given domain is determined using the conservation of mass and momentum equations, given here as

$$\frac{\partial u}{\partial x}+\frac{\partial v}{\partial y}+\frac{\partial w}{\partial z}=0 \tag{5.20}$$

$$\frac{\partial p}{\partial x}=\mu\left(\frac{\partial^2 u}{\partial x^2}+\frac{\partial^2 u}{\partial y^2}+\frac{\partial^2 u}{\partial z^2}\right) \tag{5.21a}$$

$$\frac{\partial p}{\partial y}=\mu\left(\frac{\partial^2 v}{\partial x^2}+\frac{\partial^2 v}{\partial y^2}+\frac{\partial^2 v}{\partial z^2}\right) \tag{5.21b}$$

$$\frac{\partial p}{\partial z}=\mu\left(\frac{\partial^2 w}{\partial x^2}+\frac{\partial^2 w}{\partial y^2}+\frac{\partial^2 w}{\partial z^2}\right) \tag{5.21c}$$

solved using ANSYS-Fluent CFD platform. Air flow enters through a velocity inlet in a uniform flow profile of 0.1 m/s, and leaves through a pressure outlet boundary set at atmospheric pressure. The inlet boundary is placed at a distance of $12d_f$ from the first layer of fibers, and the outlet is placed at a distance of $5d_f$ from the last layer, far from where strong pressure and velocity gradients can be expected.

Due to the scale of the coatings, the no-slip boundary condition on the surface of the fibers cannot be applied. The flow regime considered within the coating depends on fiber diameter and the thermodynamic state of the air, and include: the continuum regime ($Kn_f < 10^{-3}$), the slip-flow regime ($10^{-3} < Kn_f < 0.25$), the transition regime ($0.25 < Kn_f < 10$), and the free molecule regime ($Kn_f > 10$), where $Kn_f = 2\lambda_a/d_f$. The flow fields in our simulations are all in the slip-flow and/or transition regimes, and therefore, slip flow past the fibers must be taken into account. For simplicity, we have considered a no-slip boundary condition for the air flow on the surface of the fibers, but have corrected the computed pressure drop values using the correlation developed by Hosseini and Tafreshi (2010a), as explained in the next section. Note that the inclusion or absence of aerodynamic slip has negligible influence on collection efficiency, as the subtle changes in the streamlines around the fibers will have little impact on particles whose size is on the same order of magnitude as the fibers (Hosseini and Tafreshi, 2010a and 2010b).

The three main mechanisms by which particles are captured are inertial impaction, interception, and Brownian diffusion (Brown, 1993; Spurny, 1998; Tien, 2012). Due to the size of the particles and speed of the flow, inertial impaction is of no concern for this work. Interception is relevant when the particles and fibers are comparable in size, and Brownian

diffusion is important when the particles are small (less than about 500 nm). These latter two mechanisms are both prevalent in the study presented in this work. To determine collection efficiency for our structures, we use a Lagrangian approach to model particle capture. In the Lagrangian model, the balance of forces on each individual particle is integrated over time, revealing the particle's position and velocity in time as it moves through the domain. Note that particles do not interact with one another, and therefore do not have a collective influence on the flow field or collection efficiency results (a large number of particles can be—and are—injected) (Hosseini and Tafreshi, 2010a and 2010b). For a particle Reynolds number smaller than unity, the force-balance equations for a particle are given as (Li and Ahmadi, 1992)

$$\frac{\partial u_p}{\partial t} = \frac{18\mu}{d_p^2 \rho_p C_c}\left(u - u_p\right) + j_x(t) \tag{5.22a}$$

$$\frac{\partial v_p}{\partial t} = \frac{18\mu}{d_p^2 \rho_p C_c}\left(v - v_p\right) + j_y(t) \tag{5.22b}$$

$$\frac{\partial w_p}{\partial t} = \frac{18\mu}{d_p^2 \rho_p C_c}\left(w - w_p\right) + j_z(t) \tag{5.22c}$$

where the subscript p denotes particle properties. The term $C_c = 1 + Kn_p(1.257 + 0.4e^{-1.1/Kn_p})$ is the empirical Cunningham correction factor of for slip at the particle surface. As can be seen, the force balance equations are each the sum of two terms: the first being the drag force on the particle, and the second being the Brownian force. To add the effects of Brownian motion to the particles trajectory, we utilize a C++ subroutine that modifies Fluent's standard DPM model. This subroutine was developed and tested in the work of Hosseini and Tafreshi (2010b and 2011), and readers are referred to that work for more details. We utilize a second subroutine so that Fluent can model particle capture via interception**.** As the standard DPM model treats a particle as a point mass, this subroutine removes a particle from the domain if the particle's

center of mass comes within one radius of a fiber, rather than simply if the center of mass touches the fiber or any previously deposited particle in case particle deposition is also considered in the simulations (Hosseini and Tafreshi, 2012).

Figure 5.21 shows a conceptual illustration of the particle capture process, as 500-nm particles (red spheres) are injected in a line cutting through the xy-plane, and tracked as they move though the domain from right to left, being captured by 400-nm fibers. The injection of particles in a line is purely for visualization, i.e., particles are injected from random sites on the inlet plane for our actual simulations.

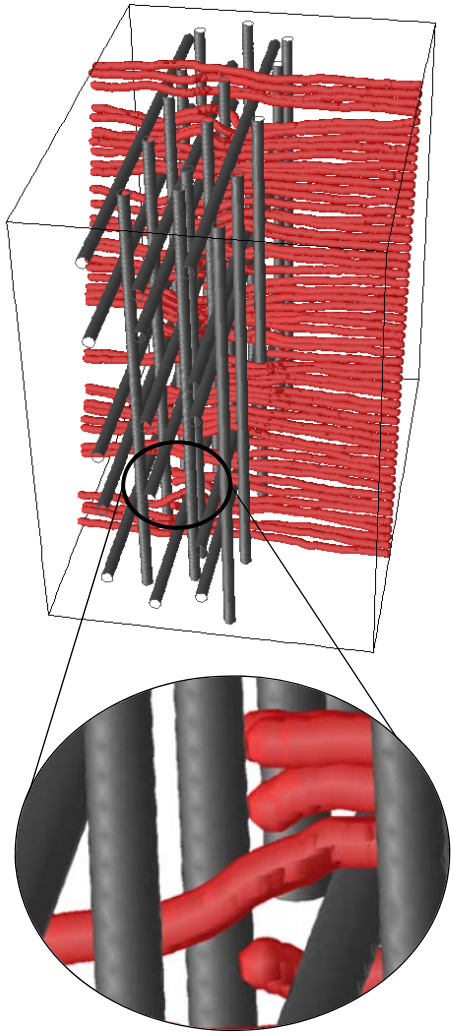

Figure 5.21: Visualization of the particle capture process in our model. 300-nm particles flow through the domain from right to left (red spheres), and are removed upon contact with a 400-nm fiber.

For the sake of brevity, validation with semi-empirical correlations in the literature for pressure drop and collection efficiency will be omitted in this thesis itself. Readers are referred to the original publication (Bucher *et al.*, Powder Technology, 2013) for details on that study. Suffice it to say for the results shown here that good agreement was observed.

The simulations conducted in this section are aimed at guiding the nanofabrication of the unimodal fibrous coatings in terms of the choice of fiber diameter, fiber spacing, and coating thickness. To eliminate the statistical noise associated with the randomness in fiber position from our simulation results, we used ordered fibrous structures for the analysis reported in the remainder of this section. Using ordered fibrous structures also allows us to reduce the size of our simulation domains to the smallest divisible unit within the filter that retains the input parameters, as is shown in Figure 5.22. Moreover, as nanofibrous coatings are extremely thin, consisting only of a very small number of layers, one can treat them as nano-sieves consisting only of one pair of layers (see e.g., Cena *et al*., 2012). In this approach, rather than categorizing our fibrous coatings with properties like SVF or thickness, we characterize them using their fiber count. The fiber count per distance f_c as an input can be more reliably measured under an SEM, with less approximation necessary than for SVF—which can still be obtained if needed. Moreover, knowing the desired fiber count per layer ahead of time can guide the fabrication process in terms of the mass of the polymer to deposit in each layer of a coating. As can be seen in Figure 5.22, fiber count in the x- and y-directions (presented in fibers per millimeter in this work) is simply the inverse of center-to-center distance s. Surface-to-surface inter-fiber distance

w and openness area A_o (measured in percent of total cross-sectional area) are both functions of fiber count and fiber diameter, and are ultimately the output parameters that more directly govern a coating's pressure drop and collection efficiency.

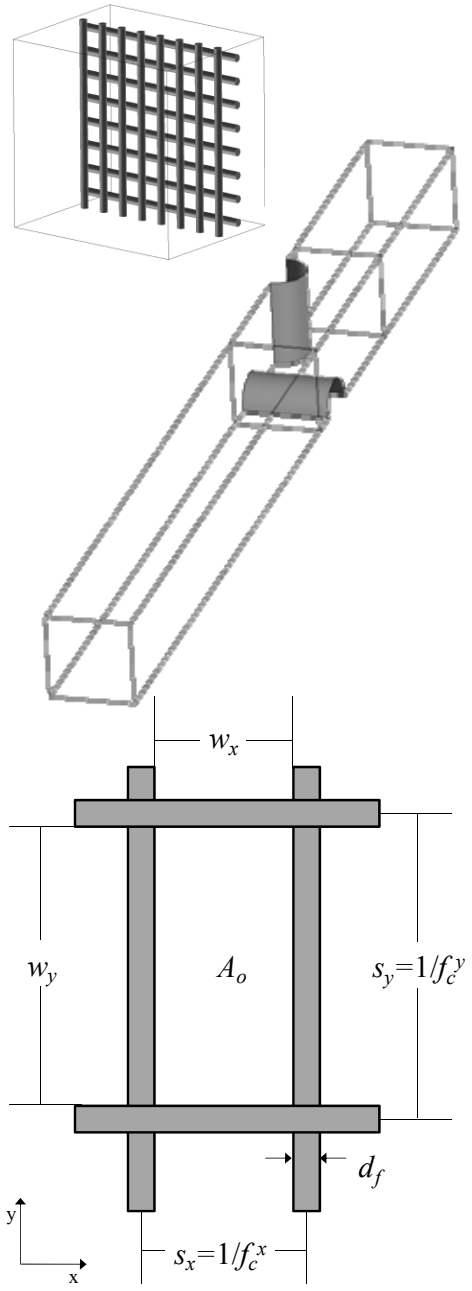

Figure 5.22: 3-D representation of an idealized thin "nano-sieve" with one pair of layers and even fiber spacing, typical simulation domain and boundary conditions for our mesh-screen unit cell model, and visual explanation of the input variables that arise in the unit cell modeling approach.

The pressure drop and collection efficiency of a fibrous coating with orthogonal fibers can be considered to vary depending on fiber diameter d_f, fiber count per layer f_c, coating's thickness l, and particle diameter d_p:

$$E = f(d_f, f_c, l, d_p) \tag{5.23}$$

$$\Delta p = f(d_f, f_c, l, d_p) \tag{5.24}$$

A commonly used parameter to characterize filter performance is the quality factor (or figure of merit) Q:

$$Q = -\ln(P_p)\Delta p_s^{-1} \tag{5.25}$$

where $P_p = 1 - E$. Quality factor is in fact a measure of attained collection efficiency for a given pressure drop.

(note in equation 5.25 that Δp_s is pressure drop value corrected for aerodynamic slip). The peculiar property of the quality factor is that it is independent of the coating's thickness, that means

$$Q = f(d_f, f_c, d_p) \tag{5.26}$$

Obviously, our objective here is to determine the fiber diameter–fiber spacing combinations that result in the highest quality factor for a given particle size.

Particle Size as the Constraint

A particle with a diameter of 150–300 nm is often considered to be the Most Penetrating Particle Size (MPPS) for most fibrous filters. This is because for such particles, both the

interception and Brownian diffusion capture mechanisms are at their minimum. Here we considered a particle diameter of 200 nm to simulate the collection efficiency of nano-sieves with different fiber diameters and fiber counts consisting of one pair of orthogonally oriented layers (see Figure 5.23). In generating this figure, fiber counts in the x- and y-directions were varied together, such that apertures between fibers are square. As expected, pressure drop and collection efficiency increase with increasing fiber count. However, the increase seems to be much faster for coatings with larger fibers. More interestingly, for a desired collection efficiency of 60%, for instance, the coating made of 1600 nm fibers causes a pressure drop almost seven times higher than that of the coating with 200-nm fibers, which clearly shows the advantage of using smaller fibers in a coating.

Figure 5.23c shows the quality factor for the above coatings. It can be seen that when challenged with particles of 200 nm diameter, coatings made of smaller fibers show much better performance in comparison to coatings made of larger fibers. One can expect that to design nano-sieves for filtering a given particle size where $Q^{(dp)} = f(d_f, f_c)$, coatings with smaller fibers have better quality factors. Increasing the fiber count f_c within the layers significantly increases both the pressure drop and collection efficiency of the coating, but the influence on the quality factor is more complicated, and seems to depend on the fiber diameter. Our results (Figure 5.23c) indicate that $Q^{(200)}$ increases with f_c for fibers comparable in diameter to the particles (200 nm here), but slightly decreases or stays unchanged for fibers much larger than the particles.

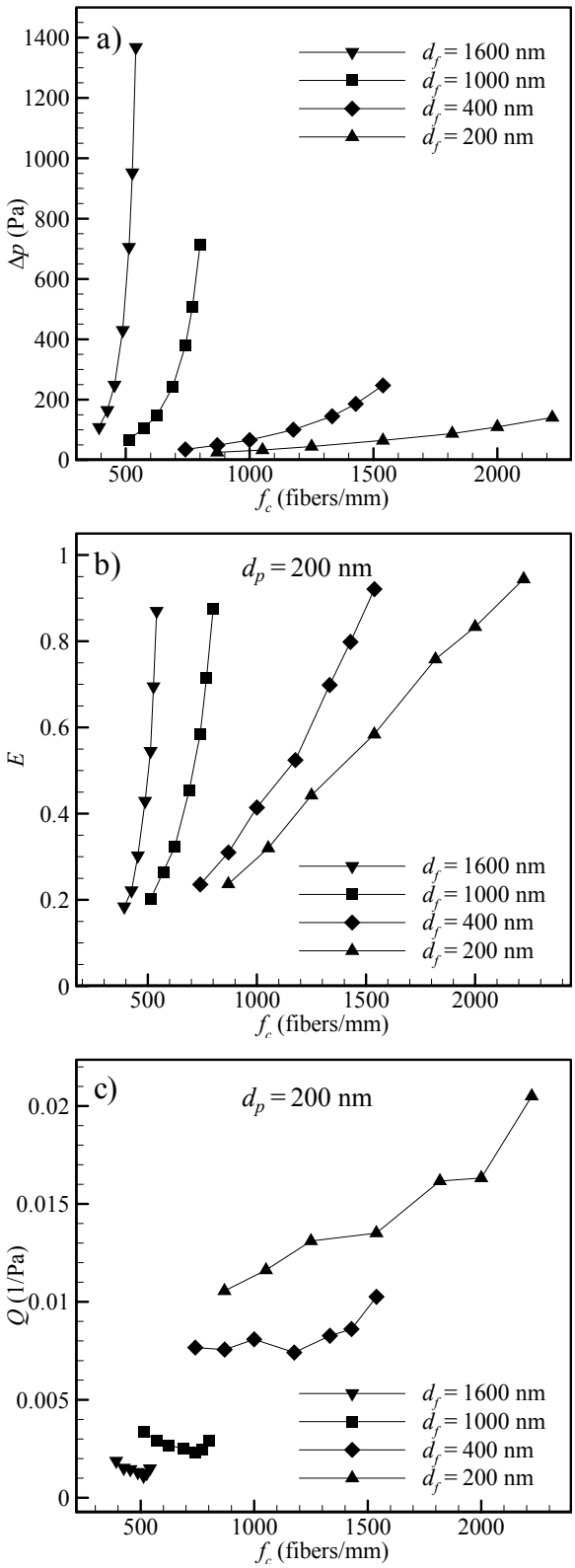

Figure 5.23: a) Pressure drop, b) collection efficiency, and c) quality factor as a function of fiber count for unit cells challenged with 200-nm particles. Results for d_f = 200, 400, 1000, and 1600 nm are shown. Fiber counts in the x- and y-directions are equal.

It is worth mentioning that, since collection efficiency of a filter is higher for particles outside the range associated to the MPPS, quality factor for particles greater or smaller than the MPPS is generally greater than that of the MPPS, i.e., $Q^{(dp)} > Q^{(MPPS)}$. Therefore, fibrous structures optimized for $Q^{(MPPS)}$ are expected to perform well for other particle sizes as well. From an application point of view for instance, such thin coatings can be applied on the downstream side of a traditional more rigid filter comprised of larger fibers to improve their performance against MPPSs (placing such a coating on the upstream face of the filter can cause undesired surface cake formation).

Fiber Size as the Constraint

There is often only a narrow range of possible fiber diameters that one can produce by electrospinning a given polymer. Therefore, to study the performance of coatings with a constant fiber diameter but varying fiber counts against particles of different sizes, where $Q^{[df]} = f(f_c, d_p)$,we challenged our coatings made of 400-nm fibers with aerosols having different particle sizes of 50, 150, and 300 nm (see Figure 5.24). Pressure drop and collection efficiency increase with fiber count, as expected. Less expected are the variations in $Q^{[df]}$. As can be seen in Figure 5.24c, Q rises with increasing fiber count for 300-nm particles (capture being mostly due to interception), but falls for 50-nm particles (capture mechanism being mostly due to Brownian diffusion). For the particles with a diameter of about 150 nm, on the other hand, the two effects are balanced, and the influence of fiber count on Q is almost negligible. To further explore this unique property, a series of additional simulations were conducted, and their results are

summarized in Figure 5.25. It can be seen in this figure that the behavior of a certain particle–fiber diameter combination being independent of fiber count in a layer is also true for other fiber sizes, with larger fiber diameters coinciding with larger particle diameters. This indicates that for each fiber diameter d_f^*, there exists a particle size d_p^* at which quality factor becomes independent of the fiber spacing, i.e., $Q^{[df^*]} = f(d_p^*)$. It can also be seen in Figure 5.25 that $Q^{[df^*]}$ is higher for larger particles, but the range of fiber count values in which collection efficiency transitions from 0 to 1 becomes narrower.

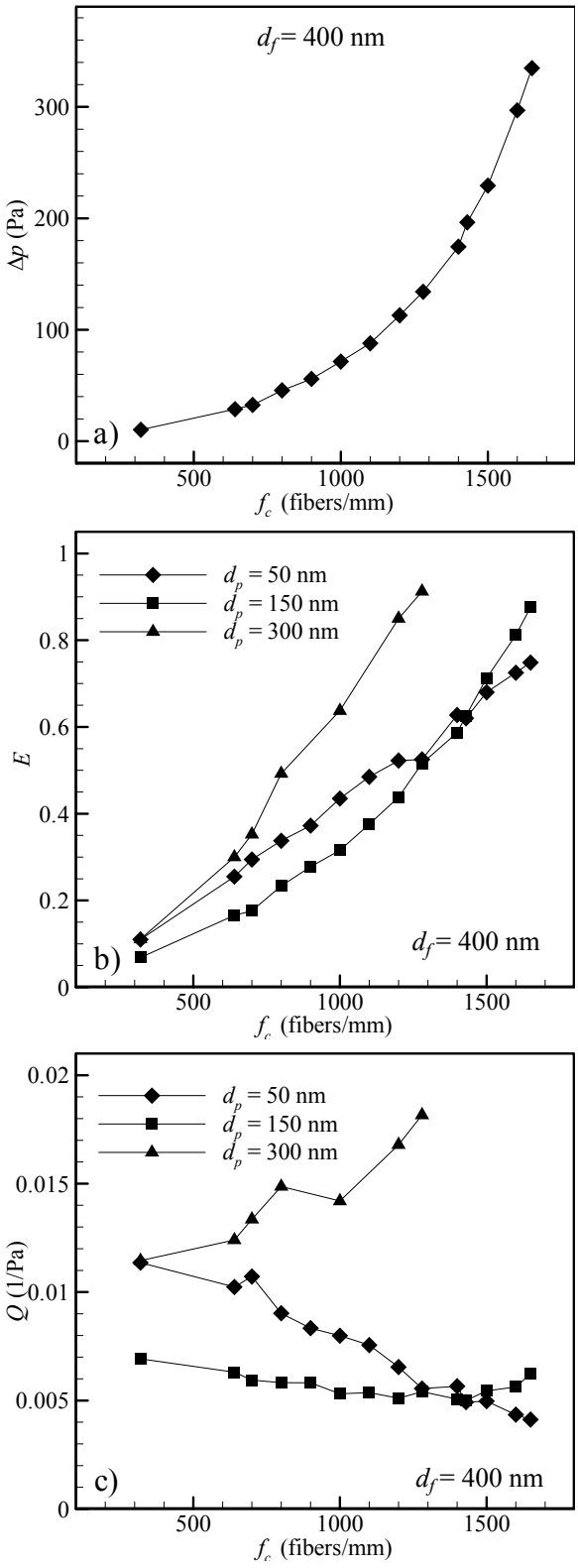

Figure 5.24: a) Pressure drop, b) collection efficiency, and c) quality factor as a function of fiber count using the unit cell model for a structure with d_f = 400 nm. Particles with d_p = 50, 150, and 300 nm were simulated. Fiber counts in the x- and y-directions are equal.

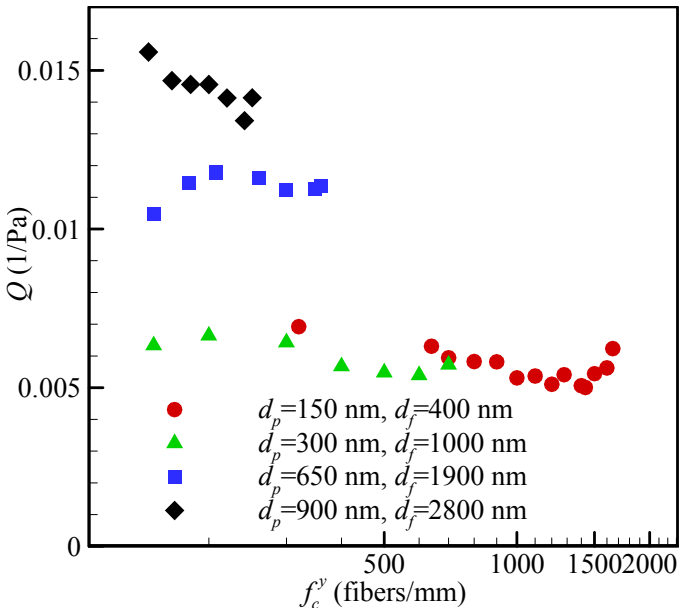

Figure 5.25: Quality factor as a function of fiber count for unit cell models with fiber diameters of: 400, 1000, 1900, and 2800 nm. The particle sizes tested for each fiber size (150, 300, 650, and 900 nm, respectively) corresponds to the particle diameter at which quality factor changes weakly with fiber count.

From the above analysis, one might infer that d_p^* corresponding to a given d_f^* is in general the MPPS for a filter made of fibers with a diameter equal to d_f^*, as is the case in Figure 5.24 where d_f^* = 400 nm. To further investigate such a possibility, we plot our collection efficiency values as a function of particle diameter for coatings with several different fiber counts, but all with a fiber diameter of 1900 nm in Figure 5.26. The corresponding d_p^* is 650 nm (shown also in Figure 5.26), well above the MPPS for that fiber diameter. The MPPS itself appears not to vary significantly from one fiber diameter to the next, while d_p^* rises as d_f^* rises.

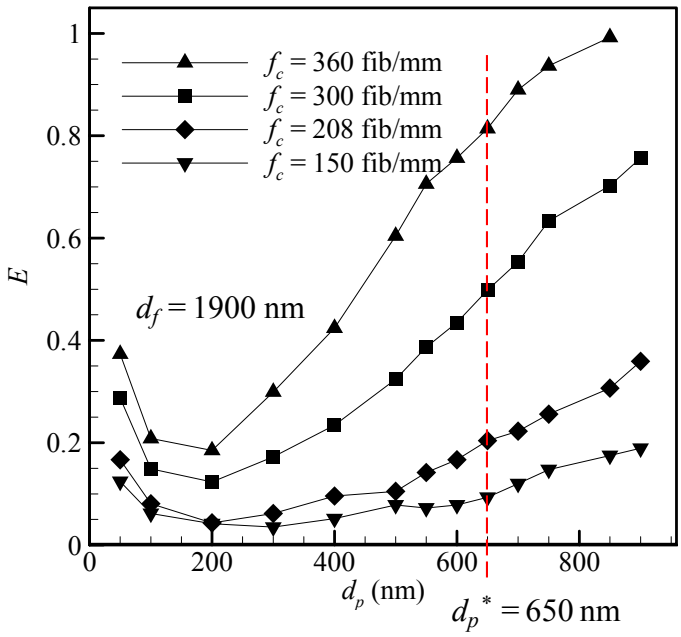

Figure 5.26: Collection efficiency as a function of particle diameter for four different fiber counts of a coating with d_f = 1900 nm. Red dashed line illustrates d_p^* for d_f^* = 1900 nm.

The quality factor of a coating being independent of its fiber count is an interesting property, because it shows that overall performance of the coating is neither lost nor gained due to non-uniformity in the coating's fiber count across the area (imperfection in fiber spacing), which is always a concern with manufacturing fibrous media. By conducting a series of similar simulations, we in fact establish a relationship between d_f^* and d_p^* for which the quality factor becomes a single-variable function, $Q^{[df^*]} = f(d_f^*) = Q^{(dp^*)} = g(d_p^*)$ as can be seen in Figure 5.27a. A linear regression performed on the data shown in Figure 5.27a, indicates that $d_f^* \cong 3d_p^*$. Figure 5.27b shows the actual value of $Q^{[df^*]} = f(d_f^*) = Q^{(dp^*)} = g(d_p^*)$ for coatings in which d_f^* and d_p^* are aligned with one another (note that each symbol represents a coating with a different fiber size). It can be seen that the general trend of $Q^{(dp^*)}$ itself is interestingly consistent with the general

statement of MPPS for most filters being between 150 and 300 nm, as the resulting quality factors across coatings following the relation between d_p^* and d_p^* behave in the same manner.

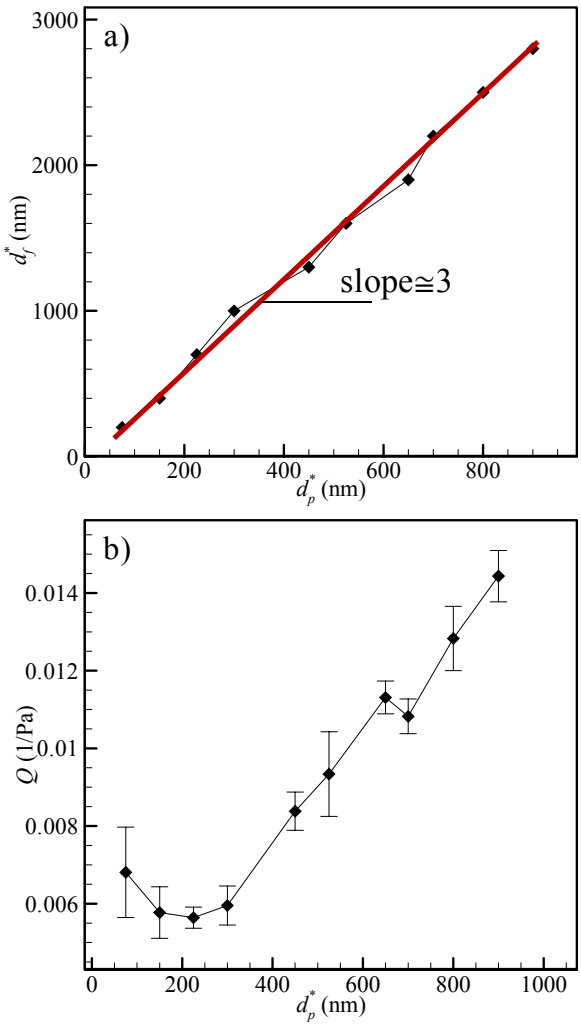

Figure 5.27: a) Target fiber diameter d_f^* shown as a function of intended capture particle diameter, where d_f^* represents the fiber diameter for which the effect of fiber count on quality factor becomes negligible for the corresponding particle diameter; b) quality factor for each corresponding coating with d_f^* as a function of particle diameter.

To study the effect of anisotropy in fiber spacing, Figures 5.28a through 5.28c show the performance as a function of fiber count for coatings with a fiber diameter of 1000 nm. The particle size for these simulations is 300 nm—the corresponding d_p^* for 1000-nm fibers. The

case of f_c^x being held constant at 200 fibers/mm is compared with the case of f_c^x and f_c^y varying together. As can be seen in Figures 5.28a and 5.28b, respectively, pressure drop and collection efficiency both reduce slightly when the apertures between fibers are not square. Quality factor in Figure 5.28c is seen to fluctuate slightly from the isotropic case, for the most part appearing slightly lower. However, the overall dependence of Q on fiber count remains negligible. We examined whether or not the fiber-count independence of Q holds for other combinations of d_p^* and d_f^*. Figure 5.28d presents the graphical information from Figure 5.25, but overlaid with hollow symbols with the same combinations of d_p^* and d_f^* as their solid-color counterparts, but with f_c^x being held at a constant value for each. As can be seen, for all cases, while quality factor fluctuates more widely for the cases in which $f_c^x \neq f_c^y$, it still does not change as a function of fiber count. From this, we confirm that the established relationship between d_p^* and d_f^* is not affected by anisotropy in the orthogonal fibers of a coating.

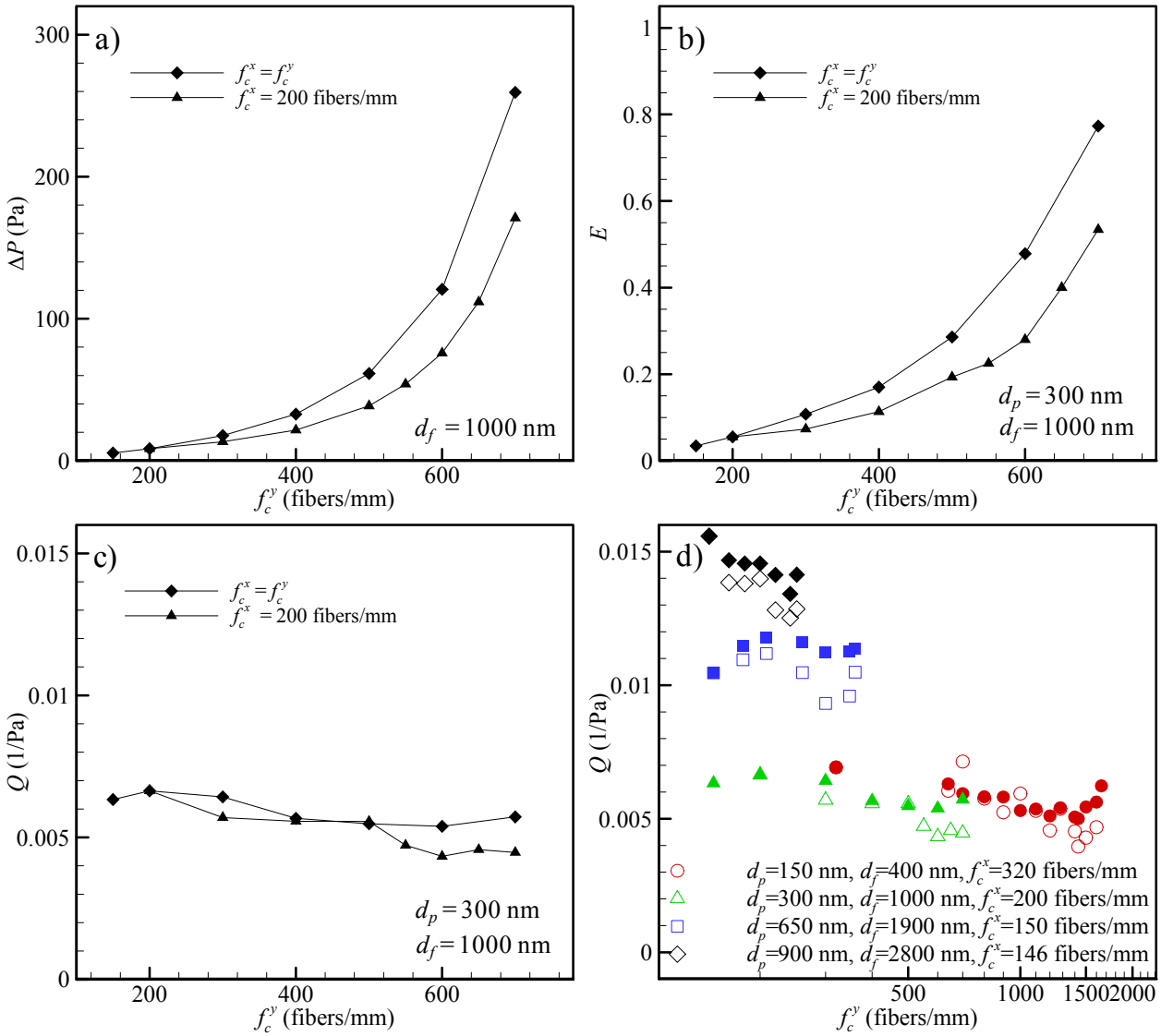

Figure 5.28: a) Pressure drop, b) collection efficiency, and c) quality factor as a function of fiber count for unit cell models with a fiber diameter of 1000 nm and the corresponding d_p^* of 300 nm. Two curves are shown for plots a–c: one for which fiber counts are equal in the x- and y-directions (square-shaped apertures between fibers); and one for which fiber count in the x-direction is held at a low value while varying y-direction fiber count (rectangular-shaped apertures). d) Quality factor as a function of fiber count for four different combinations of d_p^* and d_f^*. Legend shows information only for hollow symbols for brevity. Solid-colored symbols represent the same fiber diameter and particle diameter as the hollow point of the same color, but $f_c^x = f_c^y$ for the solid data points.

We also extended our analysis to coatings consisting of two pairs of fiber layers, with the fibers of the second pair situated on the opposite symmetry boundaries from those of the first, similar to the works of Kirsh (2006) and Dhaniyala (1999), as shown in Figure 5.29

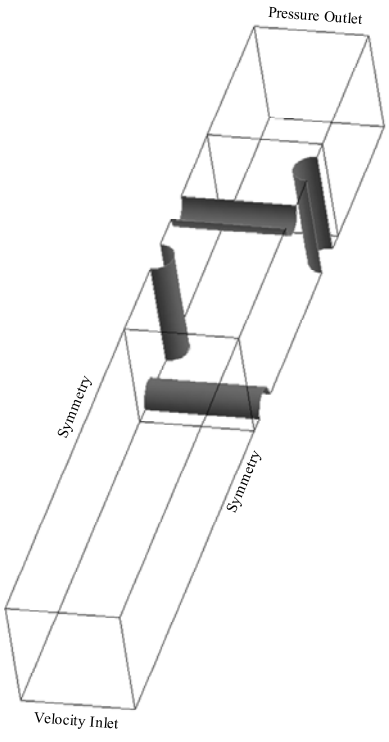

Figure 5.29: Visualization for the simulation domain and boundary conditions for a nano-sieve unit cell model consisting of two pairs of layers instead of one. Fibers of the second pair of layers are situated on the opposite symmetry boundary from those of the first.

For Figure 5.30a, we examine the effect of adding a layer on pressure drop for the case of d_f = 400 nm. As is expected, pressure drop rises for a given fiber count when a layer is added to the coating. However, rather than just examine the effect of simply adding a second pair of layers with the same fiber count as the first, one may also wish to examine the effect of simply distributing the fibers for one pair of layers across two pairs. The resulting coating would have a fiber count per layer that is half that of a coating in which the fibers are placed only in one pair of layers, but still have the same mass and number of fibers. Figure 5.30b presents the data of Figure 5.30a, but adjusted to represent both coatings having the same total mass. Pressure drop is significantly lower for the case of two pairs of layers, as is the rise in pressure drop with increasing fiber count.

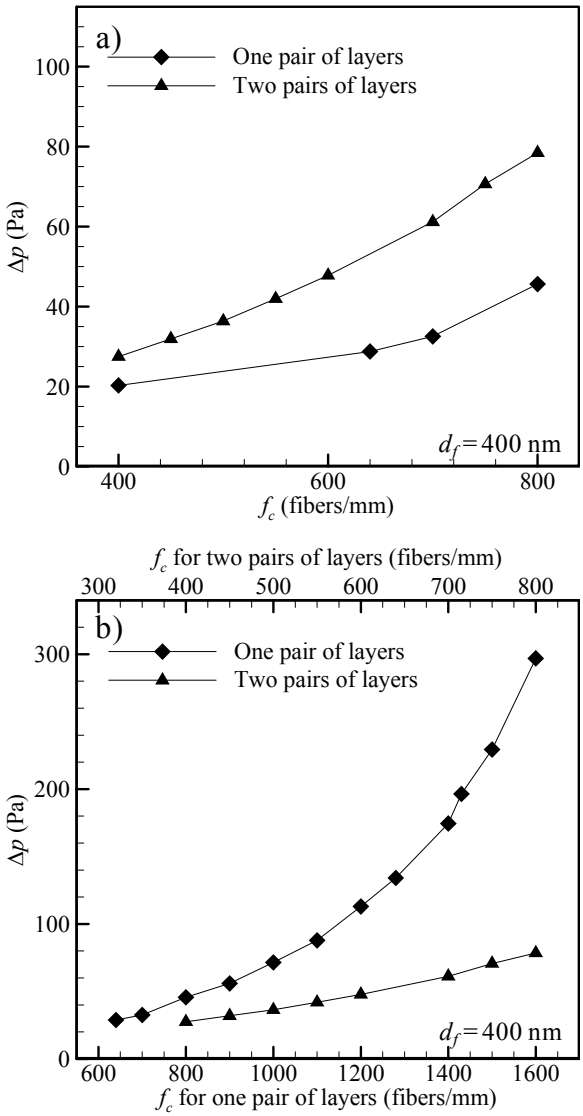

Figure 5.30: Pressure drop as a function of fiber count (x- and y-directions are equal) for unit cell models with a fiber diameter of 400 nm. The two curves in each plot represent fiber coatings comprised of one pair of layers and two pairs of layers. Figure (a) simply illustrates the difference between a coating of a given fiber count that consists of either one or two pairs of layers with that fiber count. Figure (b) shows the same data interpreted as each of the two cases having the same total mass, just distributed into either one pair of layers or two (top x-axis shows the single-layer fiber count for a coating in which the mass is spread into two pairs of layers).

Figures 5.31a and 5.31b respectively show the corresponding collection efficiency and overall quality factor for the case shown in Figure 5.30b. The particle size used is 150 nm, the corresponding d_p^* for 400-nm fibers. Notice in Figure 5.31a that collection efficiency for the two-

pair case is also reduced. This is because the first layer encounters a uniform flow field, which is disrupted for subsequent layers. This disruption reduces the collection efficiency of subsequent layers, as particles not caught in the first layer can deviate from their trajectory towards fibers of the second in the disrupted flow field. However, the reduction in pressure drop due to layering is so large that it nonetheless results in a slightly higher quality factor in Figure 5.31b. Figure 5.31 shows the improvement of Q when layering specifically for the case of the particle size corresponding to $d_f^* = 400$ nm. Q of fiber count also remains independent of fiber count per layer for two pairs of layers. From this, it is easy to see that for applications in which minimizing pressure drop is important, spreading the mass of a coating over several layers can improve overall filter performance.

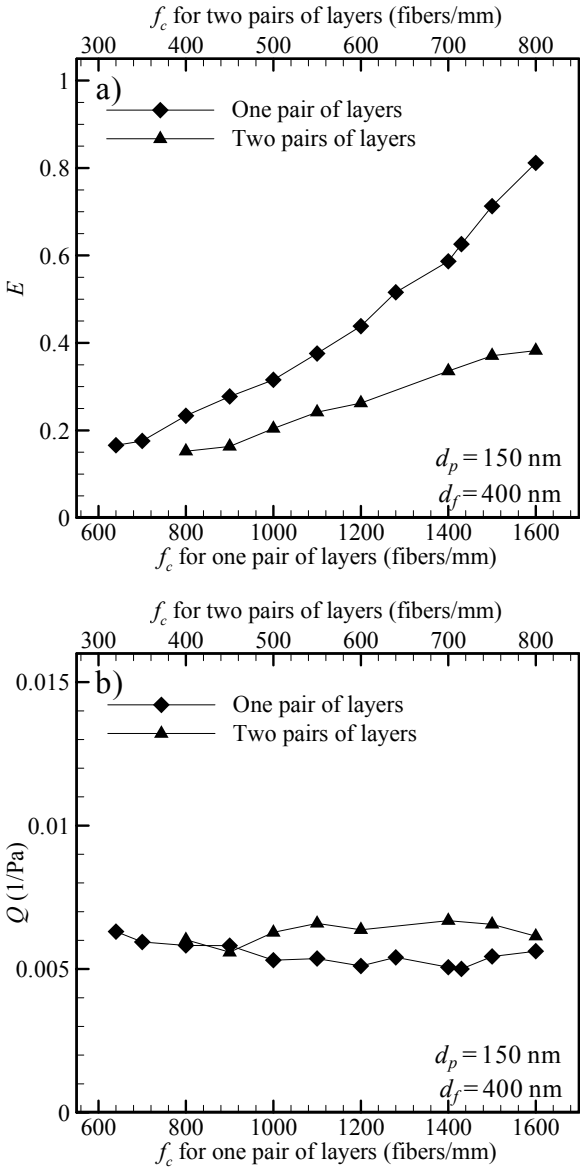

Figure 5.31: a) Collection efficiency and b) quality factor for the same case as Figure (b). Particle size of 150 nm corresponds to the quality factor independent particle size corresponding to a fiber diameter of 400 nm.

5.4 Chapter Conclusions

In this chapter, a numerical simulation strategy was discussed and used to predict the hydrostatic pressure tolerances of various bimodal, nanofibrous, superhydrophobic coatings produced via electrospinning. The Full Morphology approach was first employed in order to

examine the role of a coating's microstructural parameters in its performance, allowing for simulating randomly laid coatings as well as orthogonal. We also presented a comprehensive comparison between the predictions the FM method, our force balance formulations, and the equations of Tuteja *et al*. (2008) for fibrous coating comprised of equally spaced parallel fibers. It was found that predictions of the FM method deviates from that of the force balance method when contact angle is different from 120 degrees, but is reasonably accurate in accounting for the effects of SVF variation. The predictions of the robustness angle was found to be in close agreement with our force balance method when either SVF or contact angle were varied. The robustness height model, on the other hand, was found to be accurate only when the SVF is close to 18%.

Having established Full Morphology as a simulation method, we then developed a method for predicting coating performance by solving directly for the minimum-energy shape of the air–water interface that forms between several layers of fibers in an electrospun coating. This method has shown that critical pressure based on Full Morphology simulation is a pretty good approximation of critical pressure when comparing models. However, the method in Section 5.2 also reports wetted fiber surface area as well, and is capable of handling more than one contact angle among the constituent fibers. Our model shows that failure pressure is not actually due to mechanical failure per se, but rather due to the coalescence of the fluid meniscus with itself as it bulges around the first layer of fibers. Our results also show that the shape of the meniscus that penetrates into the spaces of a coating is scalable with fiber diameter, with critical pressure varying linearly with fiber diameter. This allows the trends illustrated in this paper to apply across the micro- and nano-scale. Our results also show the degree to which critical

pressure improves with increasing SVF, but shows a limitation to this benefit due to wetted area of the coating becoming greater than the surface are of the substrate for higher SVFs. This tradeoff between critical pressure and wetted area can be offset by allowing greater spacing between alternating fiber layers, while leaving the others with tight spacing.

Finally, on the subject of orthogonally laid electrospun nanofiber coatings, we have presented a theoretical analysis of the expected filtration performance of orthogonally layered thin nanofiber coatings (fibrous nano-sieves). Such coatings can be applied to an existing nonwoven filter to improve its collection efficiency without a significant additional pressure drop. The model produced here provides a means of predicting and therefore optimizing the performance of this class of filter coatings by isolating the contributions of their constituent microstructure properties. The flow and particle capture simulations have indicated that for each particle size, there exists a fiber diameter for which a coating's performance is not affected by the variations of the fiber-to-fiber spacing (i.e., coating's non-homogeneity). For the range of particle and fiber diameters considered in this study, the above fiber diameter is found to be about three times greater than the particle diameter. The simulations also indicate that a coating's performance improves when its mass is distributed across more than one pair of orthogonal layers.

Chapter 6

Overall Conclusions

This thesis has presented a series of approaches aimed at predicting capillarity in fibrous media. This behavior was examined in both the context of fluid absorption and fluid repulsion. Many of these models can be (and some have been) applied to existing correlations in the literature for capillary behavior. For example, the analytical force balance equation for vertical parallel fibers presented in Section 3.2 (Equation 3.8) can accommodate multiple fiber diameters and contact angles, but from it can be derived expressions for equivalent capillary diameter and capillary contact angle (Equations 3.10 and 3.11). This allows the method to be inserted into the Lucas–Washburn equation (Lucas, 1918; Washburn, 1921) or the related derivation for radial fluid spread given in Equation 2.5 (Marmur, 1988; Hyvaluoma *et al*., 2006), which would allow for absorption with respect to time. The work presented in Chapter 4 solved the Richards equation for two-phase flows (Equation 4.13) on the macroscale for fluid spread and drainage. That work used the Full Morphology method introduced in Section 3.2 to give expressions for capillary pressure as a function of saturation. Having since developed the model in Section 3.3 for horizontal parallel fibers, results of that model could also be applied to the Richards equation, facilitating multiple contact angles within the sheet along with the effect of other microstructure parameters.

Regarding superhydrophobic coatings, the Full Morphology method was again employed, this time to determine critical pressure in fibrous coatings produced via electrospinning. This method, while an educated approximation, established important relationships regarding the effect of microstructure on resistance to hydrostatic pressures. This was performed for coatings with randomly laid layers and orthogonally laid layers. Coating failure was based on the structures having saturation equal to the first layer of fibers in a uniform coating being submerged. This work was revisited in Section 5.2 in a manner similar to the work presented in Chapter 3. That is, domains representing cells in larger orthogonal coatings were constructed, and the minimum-energy shape of the air water interface was solved via the energy equation over the meniscus (Equation 5.10), establishing local failure trends that can be applied statistically over larger surfaces. The added context of the results from Section 5.2 show that the approximation of Full Morphology and our saturation estimate from Section 5.1 are considerably close to one another, validating the utility of the Full Morphology method beyond the simple case of force balance across a single pair of parallel fibers (Equation 5.5). However, solving for the minimum-energy interface curvature via Equation 5.10 still carries the additional information of wetted fiber area, which itself can be a hindrance to superhydrophobicity if A_w becomes greater than 1, as it does at higher solid volume fractions. Finally, orthogonal coatings have been shown to provide additional utility in aerosol filtration, having the unique property of a steady performance (i.e., quality factor) for a given fiber diameter–particle diameter pair.

Overall, this thesis has shown that capillarity for fibrous media can be quantified as a function of microstructural properties, fluid content, and fluid affinity of the fibers (even if more than one affinity exists in the same structure) using the true shape of the air–water meniscus over

parallel and orthogonally oriented fibers. While this thesis focused primarily on absorption and drainage in fibrous wipes and the performance of superhydrophobic coatings under pressure, the models presented here can be easily applied to many other applications in two-phase flows, such as coalescence filtration, water management in PEM fuel cells, fiber impregnation in composite materials, Laplace barriers in microfluidics, among countless others. Aside from having the true meniscus shape and location within a medium, the inclusion of multiple wettabilities and quantified contact surface area gives these models added value even if approximations for pressure in older models were fairly accurate.

List of Publications

T.M. Bucher and H.V. Tafreshi, "Effect of wetting heterogeneity on capillarity of orthogonally layered fibrous coatings," *to be submitted*

T.M. Bucher and H.V.Tafreshi, "Modeling air–water interface in disordered fibrous media with heterogeneous wettabilities," *Colloids and Surfaces A: Physiochemical and Engineering Aspects* 461, 323–335 (2014)

T.M. Bucher, H.V. Tafreshi, G.C. Tepper, "Modeling performance of thin fibrous coatings with orthogonally layered nanofibers for improved aerosol filtration," *Powder Technology* 249, 243–253 (2013)

T.M. Bucher and H.V. Tafreshi, "On applications and limitations of one-dimensional capillary formulations for media with heterogeneous wettability," *Applied Physics Letters* 102, 241606 (2013)

T.M. Bucher., B. Emami, H.V. Tafreshi, M. Gad-el-Hak, G.C. Tepper, "Modeling resistance of nanofibrous superhydrophobic coatings to hydrostatic pressures: the role of microstructure," *Physics of Fluids 24*, 022109 (2012)

A. Ashari, T.M. Bucher, H.V. Tafreshi, "Modeling motion-induced fluid release from partially-saturated fibrous media onto surfaces with different hydrophilicity," *International Journal of Heat and Fluid Flow* 382 (5), 1076–1081 (2011)

B. Emami, T.M. Bucher, H.V. Tafreshi, M. Gad-el-Hak, G.C. Tepper, "Simulation of meniscus stability in superhydrophobic granular surfaces under hydrostatic pressures," *Colloids and Surfaces A: Physiochemical and Engineering Aspects* 385, 95–103 (2011)

A. Ashari, T.M. Bucher, H.V. Tafreshi, "A semi-analytical model for simulating fluid transport in multi-layered fibrous sheets made up of solid and porous fibers," *Computational Materials Science* 50, 378 (2010)

A. Ashari, T.M. Bucher, H.V. Tafreshi, M.A. Tahir, M.S.A. Rahman, "Modeling fluid spread in thin fibrous sheets: effect of fiber orientation," *International Journal of Heat & Mass Transfer* 53, 1750 (2010)

Book Chapter

H.V. Tafreshi, T.M. Bucher, "Modeling Fluid absorption in anisotropic fibrous porous media" in Pillai, K.M., and Masoodi, R. (Eds.) *Wicking in Porous Materials:Traditional and Modern Modeling Approaches*, pp. 131–159, Publisher: Taylor and Francis/CRC (2012)

Nomenclature

A	Fluid interface cross-sectional area
A_o	Openness area
A_w	Wetted area fraction
a	Capillary length scale
a_i	One of four coefficients in Equation 3.19
B	Height of column added to boundary condition
b_{Gen}	Exponent in Equation 3.21
b_{Hav}	Exponent in Equation 3.20
b_{Lan}	Constant in Equation 4.12
C	Constant as applied to either Equation 3.20 or 3.21
C_c	Cunningham correction factor
C_{Gen}	Constant in Equation 3.21
C_{Hav}	Constant in Equation 3.20
C_{Lan}	Constant in Equation 4.12
D	Diffusive coefficient
d_{cap}	Capillary diameter
d_f	Fiber diameter

d_f^*	Spacing-independent fiber diameter
d_i	Fiber diameter for *i*-th fiber
d_p^*	Spacing-independent particle diameter
E_s	Interface nergy
E	Collection efficiency
F	Local fluid height
$\bar{F}$	Average fluid height
F_σ	Surface tension force
f_c	Fiber count
G	Level set function
g	Gravitational acceleration
j_i	Brownian force in direction *i*
K_0	Zero-order modified Bessel function of the second kind
K_1	First-order modified Bessel function of the second kind
Kn_f	Fiber Knudsen number
k	Permeability (second-order tensor)
k_d	Constant in Equation 4.18
k^r	Relative permeability
k^s	Saturated or single-phase permeability
L	Fiber length
l	Coating thickness

ℓ	Wipe length
N	Number of fibers in a layer
m_i	Mass fraction for *i*-th fiber
n	Number of layers
n_i	Fiber number fraction for *i*-th fiber
$\hat{n}$	Unit normal vector
P	Fluid interface contact perimeter
p	Fluid pressure
p_c	Capillary pressure
p_c^*	Maximum capillary pressure
p_{FB}	Force balance-based hydrostatic pressure
p_{FB}^*	Force balance-based critical pressure
p_{FM}^*	Full Morphology-based critical pressure
p_{Gen}	Capillary pressure for Equation 3.21
p_H^*	Robustness height-based critical pressure
p_{Hav}	Capillary pressure for Equation 3.20
p_{Lan}	Capillary pressure for Equation 4.12
p_{Lev}	Capillary pressure for Equation 3.19
p_θ^*	Robustness angle-based critical pressure
Q	Quality factor
R_{cf}	Coarse-to-fine fiber diameter ratio

R_{FM}^{*}	Ratio of Full Morphology to force balance critical pressure
R_{H}^{*}	Ratio of robustness height to force balance critical pressure
R_{θ}^{*}	Ratio of robustness angle to force balance critical pressure
r	Radius
r^{*}	Critical sphere radius for Full Morphology
r_m	Meniscus mean curvature
r_0	Reservoir radius
r_{cap}	Capillary radius
r_f	Fiber radius
r_{sph}	Sphere radius
S	Saturation
s	Center-to-center inter-fiber distance
s_f	Center-to-center inter-fiber distance
s_i	Distance between centers of meniscus curvature and fiber i
T	Thickness
t	Time
u	x-direction velocity
$\vec{u}$	Velocity vector
V_w	Wipe speed
v	y-direction velocity
W	Domain width

w	z-direction velocity
Z	Meniscus depth along fiber when fiber is n layers deep
z	Fluid height
z_{add}	Additional fluid height
z_{min}	Minimum fluid height
$\overline{z}$	Average fluid height

Greek Letters

α_i	Angle between fluid–fiber contact and top of i-th fiber type
α^*	Critical angle between fluid–fiber contact and top of fiber
β	Fabric inclination angle
δ	Random distance added to fiber spacing
ε	Solid volume fraction
η	Multiplier for Equation 5.1
θ	Contact angle
θ_i	Contact angle for i-th fiber type
θ_s	Solid surface contact angle
κ	Relative permeability exponent
λ	Pore size distribution index
λ_a	Mean free path of air

μ	Viscosity
ρ	Density
σ	Surface tension
σ_{lg}	Liquid–gas surface tension
σ_{sg}	Solid–gas surface tension
σ_{lg}	Solid–gas surface tension
Φ	Porosity
ϕ_i	Angle between s_f and s_i

Abbreviations

c	Coarse
f	Fine
FM	Full Morphology
fl	Fictitious layer
fm	Fibrous medium
iso	Isotropic
MPPS	Most penetrating particle size
nw	Non-wetting phase
p	Particle
ref	Reference
SVF	Solid volume fraction

References

References

A. Alizadeh, M. Yamada, R. Li, W. Sheng, S. Otta, S. Zhong, L. Ge, A. Dhinojwala, K.R. Conway, V. Bahadur, A.J. Vinciquerra, B. Stephens, and M.L. Blohm, "Dynamics of ice nucleation on water repellent surfaces," *Langmuir* 28, 3180–3186 (2012).

A. Ashari and H.V. Tafreshi, "A two-scale modeling of motion-induced fluid release from thin fibrous porous media", *Chemical Engineering Science* 64, 2067 (2009a).

A. Ashari and H.V. Tafreshi, "General Capillary Pressure and Relative Permeability Expressions for Through-Plane Fluid Transport in Thin Fibrous Sheets", *Colloids and Surfaces A: Physicochemical and Engineering Aspects* 346, 114 (2009b).

A. Ashari, T.M. Bucher, H.V. Tafreshi, "A semi-analytical model for simulating fluid transport in multi-layered fibrous sheets made up of solid and porous fibers", *Computational Materials Science* 50, 378–390 (2010).

W. Barthlott and C. Neinhuis, "Purity of the sacred lotus, or escape from contamination in biological surfaces," *Planta* 202, 1–8 (1997).

E. Bayramli and R.L. Powell, "The normal (transverse) impregnation of liquids into axially oriented fiber bundles," *Journal of Colloid and Interface Science* 138, 346–353 (1990).

J. Becker, V. Schulz, A. Wiegmann, "Numerical determination of two-phase material parameters of a gas diffusion layer using tomography images" *Journal of Fuel Cell Science and Technology*, vol. 5, no.2, art. 021006 (2008).

A. Borhan and K.K. Rungta, "An experimental-study of the radial penetration of liquids in thin porous substrates", *Journal of Colloid Interface Science* 158 (2), 403–411 (1993).

K.A. Brakke, "The Surface Evoler and the stability of liquid surfaces," *Philosophical Transactionas of the Royal Society A: Mathematical Physical and Engineering Sciences* 354 (1715), 2143–2157 (1996).

K.A. Brakke and F. Morgan, "Instabilities of cylindrical bubble clusters," European Physical Journal E 9 (5), 453–460 (2002).

R.H. Brooks and A.T. Corey, "Hydraulic properties of porous media", *Colorado State Univ., Hydrology Papers*, Fort Collins, Colorado (1964).

R.C. Brown, *Air Filtration: An Integrated Approach to the Theory and Application of Fibrous Filters*, Pergamon Press (1993).

A. B. D. Cassie, and S. Baxter, "Wettability of porous surfaces," *Transactions of the Faraday Society* 40, 546 (1944).

D.A. Caulk and D.R. Baker, "Modeling two-phase water transport in hydrophobic diffusion media for PEM fuel cells," *Journal of the Electrochemical Society* 158, B384–B393 (2011).

M. Conrath, N. Fries, M. Zhang, M.E. Dreyer, "Radial capillary transport from an infinite reservoir", *Transport in Porous Media* 84, 109–132 (2010).

C.N. Davies, *Air Filtration*, Academic Press, London (1973).

D. Danino and A. Marmur, "Radial capillary penetration into paper - limited and unlimited liquid reservoirs" *Journal of Colloid Interface Science* 166 (1), 245–250 (1994).

P.G. de Gennes, F. Brochard-Wyart, D. Quéré, *Capillaryity and Wetting Phenomena: Drops, Bubbles, Pearls, Waves*, Springer–Verlag, New York (2004).

S. Dhaniyala, B.Y.H. Liu, "An asymmetrical, three-dimensional model for fibrous filters", *Aerosol Science and Technology* 30 333–348 (1999).

F.A.L. Dullien, *Porous Media Fluid Transport and Pore Structure*, 2nd edition, Academic Press, San Diego (1992).

B. Emami, T.M. Bucher, H.V. Tafreshi, M. Gad-el-Hak, G.C. Tepper, "Simulation of Meniscus Stability in Superhydrophobic Granular Surfaces under Hydrostatic Pressures", *Colloids and Surfaces A: Physicochemical and Engineering Aspects* 305, 95–103 (2011a).

B. Emami, H.V. Tafreshi, M. Gad-el-Hak, and G.C. Tepper, "Predicting shape and stability of air-water interface on superhydrophobic surfaces with randomly distributed, dissimilar posts," *Applied Physics Letters* 98, 203106 (2011b).

B. Emami, H.V. Tafreshi, M. Gad-el-Hak, G.C. Tepper, "Predicting shape and stability of air–water interface on superhydrophobic surfaces comprised of pores with arbitrary shapes and depths," *Applied Physics Letters* 100, 013104 (2012a).

B. Emami, H.V. Tafreshi, M. Gad-el-Hak, G.C. Tepper, Effect of Fiber Orientation on shape and stability of air–water interface on submerged superhydrophobic electrospun thin coatings," *Journal of Applied Physics* 111, 064325 (2012b).

S. Fotovati, H.V. Tafreshi, B. Pourdeyhimi, "Influence of fiber orientation distribution on performance of aerosol filtration media", *Chemical Engineering Science* 65, 5285–5293 (2010).

http://fphoto.photoshelter.com/image/I000096KKIQwJAGc

J.T. Gostick, M.W. Fowler, M.A. Ioannidis, M.D. Pritzker, Y.M. Volfkovich, A. Sakars, "Capillary pressure and hydrophilic porosity in gas diffusion layers for polymer electrolyte fuel cells," *Journal of Power Sources* 156, 375–387 (2006).

L. Hao and P. Cheng, “Lattice Boltzmann simulations of water transport in gas diffusion layer of a polymer electrolyte membrane fuel cell,” *Journal of Power Sources* 195, 3870–3881 (2010).

R. Haverkamp, M. Vauclin, J. Touma, P.J. Wierenga, G.A. Vachaud, “Comparison of numerical simulation models for one-dimensional infiltration”, *Soil Science Society of America Journal* 124 (3), 285–294 (1977).

R.D. Hazlett, “Simulation of capillary-dominated displacements in microtomographic images of reservoir rocks”, *Transport in Porous Media* 20 (1–2), 21–35 (1995).

M. Hilpert and Miller CT 2001, ‘Pore-morphology-based simulation of drainage in totally wetting porous media’, *Advances in Water Resources*, vol. 24, no. 3 & 4, pp. 243–255.

K.T. Hodgson and J.C. Berg, “The effect of surfactants on wicking flow in fiber networks,” *Journal of Colloid Interface Science* 121, 22–31 (1987).

R. Hollies, M. Kaessinger, B. Watson, H. Bogaty, “Water transport mechanisms in textile materials part II: capillary-type penetration in yarns and fabrics,” *Textile Research Journal* 27, 8–13 (1957).

S.A. Hosseini and H.V. Tafreshi, “Modeling permeability of 3-D nanofiber media in slip flow regime,” *Chemical Engineering Science* 65, 2249–2254 (2010a).

S.A. Hosseini and H.V. Tafreshi, “3-D simulation of particle filtration in electrospun nanofibrous filters,” *Powder Technology* 201, 153–160 (2010b).

S.A. Hosseini and H.V. Tafreshi, “Modeling particle-loaded single fiber efficiency and fiber drag using ANSYS-Fluent code,” *Computers and Fluids* 66, 157–166 (2012).

J. Hyvaluoma, P. Raiskinmaki, A. Jasberg, A. Koponen, M. Kataja, J. Timonen, ”Simulation of liquid penetration in paper,” *Physical Review E* 73, 036705 (2006).

S. Jaganathan, H.V. Tafreshi, B. Pourdeyhimi, “A case study of realistic two-scale modeling of water permeability in fibrous media,” *Separation and Science Technology* 43 (8), 1901–1916 (2008a).

S. Jaganathan, H.V. Tafreshi, B. Pourdeyhimi, ”Modeling liquid porosimetry in modeled and imaged 3-D fibrous microstructures”, *Journal of Colloid and Interface Science* 326, 166–175 (2008b).

S. Jaganathan, H.V. Tafreshi, B. Pourdeyhimi, “A realistic modeling of fluid infiltration in thin fibrous sheets,” *Journal of Applied Physics* 105, 113522 (2009).

J. Jurin, “An account of some experiments shown before the Royal Society; with an enquiry into the cause of the ascent and suspension of water in capillary tubes,” *Philosophical Transactions of the Royal Society of London* 30 739–747 (1719).

G. Kaptay, “The threshold pressure of infiltration into fibrous preforms normal to the fibers’ axes”, *Composites Science and Technology*, 68 228–237 (2008).

R. Kessick and G. Tepper, “Microscale electrospinning of polymer nanofiber interconnections,” *Applied Physics Letters* 83, 557–559 (2003).

R. Kessick and G. Tepper, “Microscale polymeric helical structures produced by electrospinning,” *Applied Physics Letters* 84, 4807–4809 (2004).

R. Kessick and G. Tepper, “Electrospun polymer composite fiber arrays for the detection of volatile organic compounds,” *Sensors and Actuators B-Chemical* 117, 205–210 (2006).

V.A. Kirsh, “The viscous drag of three-dimensional model fibrous filters,” *Colloid Journal* 68 (3) 293–298 (2006).

K. Koch, B. Bhushan, Y.C. Jung, W. Barthlott, “Fabrication of artificial lotus leaves and significance of hierarchical structure for superhydrophobicity and low adhesion,” *Soft Matter* 5, 1386–1393 (2009).

E. Kreit, M. Dhindsa, S. Yang, M. Hagedon, K. Zhou, I. Papautsky, J. Heikenfeld, “Laplace Barriers for Electrowetting Thresholding and Virtual Fluid Confinement,” *Langmuir* 26, 18550–18556 (2010).

M. Landeryou, I. Eames, A. Cottenden, “Infiltration into inclined fibrous sheets,” *Journal of Fluid Mechanics* 529, 173–193 (2005).

C. Lee, C.H. Choi, and C. J. Kim, “Structured surfaces for giant liquid slip,” *Physical Review Letters* 101, 064501 (2008).

C. Lee and C.J. Kim, “Maximizing the giant liquid slip on superhydrophobic microstructures by nanostructuring their sidewalls,” *Langmuir* 25**,** 12812 (2009).

M.C. Leverett, “Capillary behavior in porous solids”, *Transactions of the American Institute of Mining and Metallurgical Engineers* 142, 152–169 (1941).

N. Levit and G. Tepper, “Supercritical CO_2–assisted electrospinning,” *Journal of Supercritical Fluids* 31, 329–333 (2004).

A. Li and G. Ahmadi, “Dispersion and deposition of spherical-particles from point source in a turbulent channel flow,” *Aerosol Science and Technology* 16, 209–226 (1992).

S. Litster, D. Sinton, N. Djilali, "Ex situ visualization of liquid water transport in PEM fuel cell gas diffusion layers," *Journal of Power Sources* 154, 95–105 (2005).

E.J. Lobaton, T.R. Salamon, Computation of constant mean curvature surfaces: application to the gas–liquid interface of a pressurized fluid on a superhydrophobic surface, *Journal of Colloid and Interface Science* 314, 184–198 (2007).

R. Lucas, "Rate of capillary ascension of liquids," *Kolloid Z.* 23, 15 (1918).

M.L. Ma, Y. Mao, M. Gupta, K.K. Gleason, and G.C. Rutledge, "Superhydrophobic fabrics produced by electrospinning and chemical vapor deposition," *Macromolecules* 38**,** 9742–9748 (2005).

M.L. Ma, R.M. Hill and G.C. Rutledge, "A review of recent results on superhydrophobic materials based on micro- and nanofibers," *Journal of Adhesive Science and Technology* 22, 1799–1817 (2008).

N. Mao and S.J. Russell, "Anisotropic liquid absorption in homogenous two dimensional nonwoven structure", *Journal of Applied Physics* 94, 4135 (2003).

N. Mao, "Unsteady-state liquid transport in engineered nonwoven fabrics having patterned structure", *Textile Research Journal* 79 (15), 1358–1363 (2009).

R. Masoodi, K.M. Pillai, *Wicking in Porous Materials Traditional and Modern Modeling Approaches*, CRC Press Taylor and Francis Group, Boca Raton (2013).
A. Marmur, "The radial capillary", *Journal of Colloid and Interface Science* 124 (1), 301–308 (1988).

D. Maynes, K. Jeffs, B. Woolford, and W. Webb, "Laminar flow in a microchannel with hydrophobic surface patterned microribs oriented parallel to the flow direction," *Physics of Fluids* 19, 093603.1 (2007).

B. Maze, H.V. Tafreshi, and B. Pourdeyhimi, "Geometrical modeling of fibrous materials under compression," *Journal of Applied Physics* 102, 073533 (2007a).

B. Maze, H.V. Tafreshi, Q. Wang, and B. Pourdeyhimi, "Unsteady–state simulation of nanoparticle aerosol filtration via nanofiber electrospun filters at reduced pressures," *Journal of Aerosol Science* 38, 550–571 (2007).

S. McKee, M.F. Tomé, V.G. Ferreira, J.A. Cuminato, A. Castelo, F.S. Sousa, N. Mangiavacchi, "Review: The MAC Method," *Computers and Fluids* 37, 907–930 (2008).

B. Miller and S.H. Jansen, "Wicking of liquids in nonwoven fibre assemblies", *Proc. 10th Technical Symposium on Advances in Nonwovens Technology*, 216–226 (1982).

http://www.nasa.gov/centers/langley/business/tg-img-fibermats.html

F.O. Ochanda, M.A. Samaha, H.V. Tafreshi, G.C. Tepper, and M. Gad-el-Hak, "Fabrication of superhydrophobic coatings by DC-biased AC-electrospinning," J. Appl. Polym. Sci. **123**, 1112–1119 (2012a).

A. Podgorski, A. Bałazy, L. Gradon, "Application of nanofibers to improve the filtration efficiency of the most penetrating aerosol particles in fibrous filters," *Chemical Engineering Science* 61 6804 – 6815 (2006).

A. Ponomarenko, D. Quére, and C. Clanet, "A universal law for capillary rise in corners," *Journal of Fluid Mechanics* 666, 146–154 (2011).

C. Pozrikidis, Computation of three-dimensional hydrostatic menisci, *IMA Journal of Applied Mathematics*. 75, 418–438 (2010).

H.M. Princen, "Capillary phenomena in assemblies of parallel cylinders 2: capillary rise in systems with more than two cylinders, *Journal of Colloid and Interface Science* 30 (3), 359–371 (1969).

D.H. Reneker and A.L. Yarin, "Electrospinning jets and polymer nanofibers," *Polymer* 49, 2387–2425 (2008).

L.A. Richards, "Capillary conduction of liquids through porous medium", *Physics* 1, 318–333 (1931).

J.P. Rothstein, "Slip on superhydrophobic surfaces", *Annual Review of Fluid Mechanics* 42, 89–109 (2010).

A.A. Saha, S.K. Mitra, M. Tweedie, S. Roy , J. McLaughlin, "Experimental and numerical investigation of capillary flow in SU8 and PDMS microchannels with integrated pillars," *Microfluid Nanofluid* 7, 451–465 (2009).

M.A. Samaha, F.O. Ochanda, H.V. Tafreshi, G.C. Tepper, and M. Gad-el-Hak, "In situ, non-invasive characterization of superhydrophobic coatings," *Review of Scientific Instruments* 82**,** 045109 (2011).

S. Sarkar, S.C. Deevi, G.C. Tepper, "Biased AC electrospinning of aligned polymer nanofibers", *Macromolecular Rapid Communications* 28, 1034–1039 (2007).

A. Schultz, I. Papautsky, J. Heikenfeld, "Investigation of Laplace Barriers for Arrayed Electrowetting Lab-on-a-Chip," *Langmuir* 30, 5349–5356 (2014).

R.S. Seymour and S.K. Hetz, "The diving bell and the spider: the physical gill of *argyroneta aquatic*," *Journal of Experimental Biology* 214, 2175–2181 (2011).

L. Spielman and S.L Goren, "Model for predicting pressure drop and filtration efficiency in fibrous media", *Environmental Science and Technology* 2 (4), 279–287 (1968).

Spurny, K.R., *Advances in Aerosol Filtration, Lewis Publisher*, CRC Press LLC (1998).

H.V. Tafreshi, M.S.A. Rahman, S. Jaganathan, Q. Wang, and B. Pourdeyhimi, "Analytical expressions for predicting permeability of bimodal fibrous porous media," *Chemical Engineering Science* 64, 1154 (2009).

M.A. Tahir, H.V. Tafreshi, "Influence of fiber orientation on the transverse permeability of fibrous media," *Physics of Fluids* 21 (8), 083604 (2009).

C. Tien, *Principles of Filtration*, Elsevier (2012).

K. Tuber, D. Pocza, C. Hebling, "Visualization of Water Buildup in the Cathode of a Transparent PEM Fuel Cell," *Journal of Power Sources* 124 (2), 403–414 (2003).

A. Tuteja, W. Choi, J.M. Mabry, G.H. McKinley, and R.E. Cohen, "Robust omniphobic surfaces," *Proceedings of the National Academy of Sciences of the United States of America* 105, 18200–18205 (2008).

M.T. Van Genuchten, "A closed-form equation for predicting the hydraulic conductivity of unsaturated soils," *Soil Science Society of America Journal* 44, 892–898 (1980).

E. Washburn, "The dynamics of capillary flow", *The Physical Review* 17 (3), 273–283 (1921).

Weislogel, "Compound capillary rise," *Journal of Fluid Mechanics* 709, 622–647 (2012)..
R. N. Wenzel, "Resistance of a solid surface to wetting by water," *Industrial and Engineering Chemistry* 28, 988 (1936).

A.L. Yarin, S. Koombhongse, and D.H. Reneker, "Taylor cone and jetting from liquid droplets in electrospinning of nanofibers," *Aournal of Applied Physics* 90, 4836–4846 (2001).

Q. Zhang, J. Welch, H. Park, C. Wu, W. Sigmund, J.C.M. Marijnissen, "Improvement in nanofiber filtration by multiple thin layers of nanofiber mats," *Journal of Aerosol Science* 41 230–236 (2010).

Q.S. Zheng, Y. Yu, and Z.H. Zhao, "Effects of hydraulic pressure on the stability and transition of wetting modes of superhydrophobic surfaces," *Langmuir* 21, 12207 (2005).

B.V. Zhmud, F. Tiberg, K. Hallstensson, "Dynamics of capillary rise", *Journal of Colloid and Interface Science* 228 (2), 263–269 (2000).

P. Zhou and C.W. Wu, "Liquid water transport mechanism in the gas diffusion layer," *Journal of Power Sources* 195, 1408–1415 (2010).

Vita

Thomas M. Bucher, Jr.

3435 Hanover Ave. Apt. 2
Richmond, VA 23221
Email: buchertm@mymail.vcu.edu

Education

- **Ph.D., Mechanical and Nuclear Engineering** (December 2014)
  Virginia Commonwealth University, Richmond, VA
  GPA 4.0
  Dissertation title: "Capillarity and Two-Phase Fluid Transport in Media with Fibers of Dissimilar Properties"

- **M.S., Mechanical and Nuclear Engineering** (August 2012)
  Virginia Commonwealth University, Richmond, VA
  GPA 4.0
  Thesis title: “Modeling the Resistance to Hydrostatic Pressures for Superhydrophobic Coatings Comprised of Random Roughness”

- **B.S., Mechanical Engineering** (May 2010)
  Virginia Commonwealth University, Richmond, VA
  GPA 3.859 Magna Cum Laude

Research Experience

VCU Porous Media and Multiphase Flows Laboratory (May 2009–Present)

- Developing numerical models for predicting absorption and drainage characteristics for 2-D and 3-D lump, composite, and layered fibrous materials. Influence of parameters of microstructure are determined on the scale of the fibers, and in turn applied on the macroscale to predict overall fabric performance. Simulation methodology is validated and refined using experimental data, some of which has been performed for or with several companies in the nonwoven fabrics industry, with deliverables including custom-made experimental methodologies and user-friendly graphical interfaces to perform simulations in a streamlined fashion

- Performing research in the field of aerosol filtration, modeling particle capture in nano-fibrous filter coatings using commercial software enhanced with in-house subroutines (user-defined functions). These coatings, when applied to the surface of micro-fiber filter media, can significantly improve the filter’s overall efficiency by capturing particles which escaped the larger filter, and with a fraction of the cost and material usage of larger and more complex filter media

- Developing numerical models for predicting the performance of granular and nano-fibrous superhydrophobic coatings under elevated hydrostatic pressure for submersible applications. Such coatings on the surface of a submerged object may significantly reduce the skin-friction drag along the object as it moves through water, therby reducing energy consumption and flow-induced noise (subject of M.S. thesis)

Publications

- **Bucher, T.M.**, Tafreshi, H.V., "Effect of Wetting Heterogeneity on Capillarity of Orthogonally Layered Fibrous Coatings," *to be submitted*
- **Bucher, T.M.**, Tafreshi, H.V., "Modeling Air–Water Interface in Disordered Fibrous Media with Heterogeneous Wettabilities," *Colloids and Surfaces A: Physiochemical and Engineering Aspects* 461, 323–335 (2014)
- **Bucher, T.M.**, Tafreshi, H.V., Tepper, G.C., "Modeling Performance of Thin Fibrous Coatings with Orthogonally Layered Nanofibers for Improved Aerosol Filtration," *Powder Technology* 249, 243–253 (2013)
- **Bucher, T.M.**, Tafreshi, H.V., "On Applications and Limitations of One-Dimensional Capillary Formulations for Media with Heterogeneous Wettability," *Applied Physics Letters* 102, 241606 (2013)
- **Bucher, T.M.**, Emami, B., Tafreshi, H.V., Gad-el-Hak, M., Tepper, G.C., "Modeling Resistance of Nanofibrous Superhydrophobic Coatings to Hydrostatic Pressures: the Role of Microstructure," *Physics of Fluids* 24, 022109 (2012)
- Ashari, A., **Bucher, T.M.**, Tafreshi, H.V., "Modeling Motion-Induced Fluid Release from Partially-Saturated Fibrous Media onto Surfaces with Different Hydrophilicity," *International Journal of Heat and Fluid Flow* 382 (5), 1076–1081 (2011)
- Emami, B., **Bucher, T.M.**, Tafreshi, H.V., Gad-el-Hak, M., Tepper, G.C., "Simulation of Meniscus Stability in Superhydrophobic Granular Surfaces under Hydrostatic Pressures," *Colloids and Surfaces A: Physiochemical and Engineering Aspects* 385, 95–103 (2011)
- Ashari, A., **Bucher, T.M.**, Tafreshi, H.V., "A Semi-Analytical Model for Simulating Fluid Transport in Multi-Layered Fibrous Sheets Made Up of Solid and Porous Fibers," *Computational Materials Science* 50, 378 (2010)
- Ashari, A., **Bucher, T.M.**, Tafreshi, H.V., Tahir, M.A., Rahman, M.S.A., "Modeling Fluid Spread in Thin Fibrous Sheets: Effect of Fiber Orientation," *International Journal of Heat & Mass Transfer* 53, 1750 (2010)

Book Chapter

- Tafreshi, H.V., **Bucher, T.M.**, "Modeling Fluid Absorption in Anisotropic Fibrous Porous Media" in Pillai, K.M., and Masoodi, R. (Eds.) *Wicking in Porous Materials:Traditional and Modern Modeling Approaches*, pp. 131–159, Publisher: Taylor and Francis/CRC (2012)

Conference Presentations with Peer-Reviewed Abstracts

- **Bucher, T.M.**, B. Emami, Tafreshi, H.V., "Modeling superhydrophobic Surfaces Comprised of Randomly Deposited Fibers or Particles," *4th International Conference on Porous Media and Annual Meeting of the International Society for Porous Media*, May 14–16 (2012)
- Tafreshi, H.V., **Bucher, T.M.**, "Modeling Transport Phenomena in Anisotropic Fibrous Media," *4th International Conference on Porous Media and Annual Meeting of the International Society for Porous Media*, May 14–16 (2012)

- **Bucher, T.M.**, Emami, B., Tafreshi, H.V., Gad-el-Hak, M., Tepper, G.C., "On the Resistance of Nanofibrous Superhydrophobic Coatings to Hydrostatic Pressures," *Bulletin of the American Physical Society* 56, no. 18, p. 175 (2011)
- **Bucher, T.M.**, Tafreshi, H.V., "An Overview on Modeling Fluid Absroption in Fibrous Media," *NETinc, Innovative Nonwovens Conference*, Sep 13–15 (2011), Atlanta Georgia (2011)

Professional Activities

- **Professional Society**
  - Interpore (International Society for Porous Media)
- **Assisted in reviewing articles for the following journals**
  - Chemical Engineering Research and Design
  - Chemical Engineering Science
  - Drying Technology
  - International Journal of Heat and Mass Transfer
  - Journal of Nanoparticle Research
  - Lab on a Chip
  - Separation and Purification Technology
  - Textile Research Journal
- **Graduate Research activities funded by**
  - Virginia Commonwealth University (August 2012–Present)
  - National Science Foundation (January 2012–Present)
  - Johnson & Johnson (January 2011–December 2011)
  - Defense Advanced Research Projects Agency (DARPA) (September 2010–January 2011)
  - Ahlstrom (August 2010–January 2011)

Awards

- VCU Engineering Outstanding Graduate Research Assistant (Spring 2014)
- Federal Science and Math Retain Talent Grant (Fall 2007–Spring 2009)

Other Relevant Accomplishments

- **Mircoscale–Macroscale Fluid Absorption Model** (January 2011–December 2011)
  Developed user-friendly software model for predicting the fluid-absorption and transfer performance of multiple fabric layers in absorbent products based solely on the properties of the fluid and microstructure of the fabrics. Several accompanying experimental procedures were also developed in order to complement and validate the software model. Program and experimental apparatus were developed for use as a design tool for Johnson & Johnson, Inc.

- **Ph.D. Qualifying Exam** (Fall 2010)
  Successfully passed the Ph.D. Qualifying Exam for the VCU Department of Mechanical and Nuclear Engineering in my first semester as a graduate student, less than six months after my baccalaureate

- **VCU Nuclear Reactor Simulator** (Fall 2009–Spring 2010)
  Combined cumulative engineering knowledge with prior Navy experience, and was instrumental in the initial construction and programming of a nuclear power plant simulator that has gone on to become a training and education tool for the VCU Nuclear Engineering Program

- **Tobacco Company Restaurant** (2004–2008)
  Spent the first two thirds of my undergraduate education also supporting myself and my education by working full time as a cook at the famous Tobacco Company Restaurant in Downtown Richmond

Mentorship Experience

- **Undergraduate Fluid Mechanics Independent Study** (Fall 2011–Spring 2012)
  Conducted the undergraduate Fluid Mechanics course as an independent study for one undergraduate student. Duties included tutoring; writing, assigning, and grading homework assignments; and writing and conducting midterm and final exams

- **VCU Porous Media and Multiphase Flows Laboratory** (Summer–Fall 2010)
  Supervised five undergraduate student workers in various design and experimental work involving several lab projects

- **Engineering Thermal Sciences Lab Teaching Assistant** (Spring 2010)
  Set up weekly experiments, supervised thirty students as they conducted the experiments in small groups, and graded their subsequent lab reports, also made myself available to answer students' questions throughout the week as they wrote their reports

Graduate Coursework

- Advanced Engineering Mathematics (EGRM 512)
- Vibrations (EGRM 515)
- Advanced Fluid Mechanics (EGRM 561)
- Flow Control (EGRM 580)
- Continuum Mechanics (ENGR 591)

- Porous Media Independent Study (EGRM 692)
- Mechanical and Nuclear Engineering Materials (EGMN 604)
- Topics in Nuclear Engineering (EGRN 610)
- Nuclear Reactor Safety (EGRN 640)
- Energy Conversion Systems (EGRM 691)
- Nuclear Power Plants (EGRN 630)
- Convective Heat Transfer (EGRM 602)
- Numerical Solutions to Partial Differential Equations (MATH 715)

Industry Experience

- **United States Naval Nuclear Propulsion Program** (1997–2001)
  Orlando, FL; Ballston Spa, NY
  Nuclear plant mechanical operator and instructor

Software Proficiencies

- **Engineering**
  ANSYS-FLUENT, Gambit, Surface Evolver, FlexPDE, Geodict, Solidworks, Particle Image Velocimetry (PIV) software
- **Programming Languages**
  Matlab, C
- **General**
  LaTeX, Tecplot, SigmaPlot, Adobe Photoshop, MS Office, Linux Open Office